Ultrasonic Inverse Scattering Problem in Layered Media

(層状媒質における超音波逆散乱問題)

by

Dong-Lai Liu

Supervised by *Prof. Masao Saito*

Department of Electronic Engineering, Faculty of Engineering,
Graduate School, University of Tokyo

December 21, 1990

Abstract

This is a summary of our research which is related to the measuring and imaging of a non-uniform, refractive medium by ultrasound. This non-uniformity may be of interest by itself. It may also become a disturbing factor if our purpose is to know about the details beneath it. Anyway we must know about its properties, for example the spatial distribution of the sound velocity inside it, before we can take its influence into consideration.

Inferring medium properties from the incident and the scattered waves has been studied under the general name of *the inverse scattering problem*, which includes one-, two- and three-dimensional problems. To solve three-dimensional problems, signals need to be recorded on a surface enclosing the object, and the calculation requirement is in most cases too big for the computing power available today. From technological restrictions as well as analytical difficulties, most research works are confined to one- or two-dimensional problems. The solution of two-dimensional problems is usually via the Born or the Rytov approximation, which is valid only for weak inhomogeneities.

Turning to one-dimensional problems, since the parameters of the medium change only in one direction, the measurement and processing is usually much easier. However to solve this problem exactly would require the impulse response of the medium to be known. Viewing in the frequency domain, this means knowledge of the reflection coefficient to harmonic waves of frequencies from DC to infinity. In practice we can only measure with a transducer of limited bandwidth. Another realistic problem is that transducers usually have directivities that are difficult to control. In inverse scattering measurement, waves from different directions are received by the same transducer. Without knowing from which direction the wave comes and the directivity of the transducer, it is practically impossible to use the amplitude information contained in the received signal.

With these practical considerations in mind, we considered the possibility of calculating the sound velocity profile of a one-dimensional medium from reflected signals which are band-limited and noise-corrupted. Then, layered media with plane interfaces, either parallel or non-parallel, are dealt with. In doing this we have avoided using the amplitude information which is system-dependent and unreliable, as noted above. Instead we use the time information contained in the signals. However, if the amplitude information is available, then the density of each layer can be calculated at the same time.

Roughly speaking, the measurement required by our methods can be performed in the following way, for calculating the sound velocity of each layer and the geometrical configuration of the medium. A spherical wave is generated by a point-like transducer, and the reflected wave is received by several receivers (at least 2 for horizontally-layered media, and 3 for non-parallel layered media) at different locations. The important thing is that these receivers must not be too close together, because we are using the differences in the arrival time of the echoes to infer about the sound velocity of each layer.

The main results of our research can be summarized as the following:

1. Demonstrated that it is possible to calculate the sound velocity profile of a one-dimensional medium using only a relationship between the travel times corresponding to two different incident angles;

2. Developed algorithms for calculating the sound velocities and thicknesses of layered media with either horizontal or non-parallel plane interfaces;

3. Proposed a spectral fitting approach to recover an δ-impulse series from its filtered and noise-corrupted version. Evaluated the error of the positions of these δ-impulses caused by measurement noise.

All of these results have been verified by computer simulation and by experimental measurements of some simple geometries.

Our treatment of the one-dimensional problem is unprecedented so far as we know. On comparing two signals measured at different incident anglse, it

is noticed that waves coming from the same depth resemble each other, even though they arrive at the surface at different time instants. This fact indicates that it is possible to make the two waveforms nealy the same (according to certain criteria) by stretching or contracting the time-axis of one of them. In this way a functional relationship is established between the two travel times. A simple derivation is then given which shows that the one-dimensional sound velocity profile can be recovered as a function of depth from this travel time relationship, under the assumption that the probing wave is a plane wave.

Next we turned our attention to layered media. Apparently a layered medium with horizontal plane interfaces is a special case of the general one-dimensional media. The new problem here is that the probing wave is not planar, but spherical. Using the ray approximation we investigated the dependency of increments of travel time on the propagation angle, and found the relationship $dt \sim \cos^{\alpha}\theta$ to be a very good approximation. Based upon this observation we modified the analysis which is derived under the plane wave assumption, and developed an algorithm for the processing of data obtained with spherical waves.

Layered media with non-parallel interfaces are treated quite differently. Although some relationships have been established between increments of travle time and propagation angles, the final solution is based upon a minimization formulation, *i.e.*, the medium parameters are varied so that the travel times calculated from the reconstructed model agree with those of observation. The adjustment of the sound velocity c_k of the kth layer is made through the secant method, whereas the thickness d_k and the inclination angle γ_k are obtained by solving a minimization problem, using the Marquardt-Levenberg algorithm, which is a combination of the Gauss-Newton method and the gradient method.

The problem of estimating pulse positions from signals which contain measurement noise has been considered. The reflection from a layered medium is modeled by the convolution of an incident pulse with the impulse response

of the medium, which consists of a series of δ-impulses. The problem is to estimate the accurate positions of these δ-impulses from the received signal. We propose to solve this problem by a spectral fitting approach, in which we fit terms like $\rho_i e^{-i\omega\tau_i}$ to the estimated spectrum of the impulse response. This fitting problem can be solved efficiently using the FFT. Furthermore we analysed the fluctuation of the estimated pulse positions caused by additive noise, using the peak position of the cross-correlation function. This not only leads to an analytical evalution of the fluctuation, but also provides an alternative way for estimating the delay between two pulses. In fact this latter approach is less time consuming when the rough positions of the two pulses are known, and the best combination would be to use the spectral fitting technique to scan the whole signal, which provides rough positions of the pulses, and then to use the correlation technique, together with spline interpolation, to get accurate estimation of the positions.

This dissertation consists of 7 chapters. The above analyses and discussions are contained in chapters 1 through 4. Chapter 5 is on computer simulation, in which we demonstrated deconvolution by spectral fitting, compared the fluctuation of pulse positions to the result of analysis, and performed inversion to parallel layered media probed by either plane or spherical waves, and to non-parallel layered media probed by spherical waves. In chapter 6, results of experimental measurements are reported, including the deterioration of image qualities caused by a distortion plate, compensation for the distortion effect using travel time residuals, and results of processing the data measured with both parallel and non-parallel interfaced layered media.

Although we have not been able to go so far as to apply the methods proposed here to actual human data, simply because that the geometries we have treated are still not general enough, we think that we are heading towards the solution of the problem.

CONTENTS

1

Introduction

1.1 A Brief Review of Ultrasonic Imaging

The practice of generating a wave from the outside of an object, and investigating the interior of the object by detecting and analysing the scattered waves, is becoming commonplace. The application of ultrasound in medical diagnosis is a typical example. Others include the exploration seismics, non-destructive evaluation of materials, radar and sona, *etc.*

From the principle of operation, the application of ultrasound in medical diagnosis can be divided into two categories, *i.e.*, Doppler methods and pulse-echo methods [1]. The former make use of the Doppler frequency shift to measure the movement of blood or the heart wall or other parts, while the latter, although have many different forms, measure the echoes due to a generated pulse to infer about the acoustical non-uniformity of the object.

In this dissertation we deal exclusively with the latter. The basic principle of the pulse-echo system is illustrated in Fig. 1.1. An acoustic pulse is generated at the surface of the body. It propagates into the deeper part, while at the same time, is reflected back to the surface by the non-uniformity of the body. The reflected waves (echoes) are received by a transducer, amplified and processed to provide information useful for medical diagnosis.

There are several forms in which this information can be displayed, *i.e.*, the A-scope, the B-scope, and the M-scope. With the A-scope, the received signal is demodulated (rectified) and low-pass filtered. The resultant signal

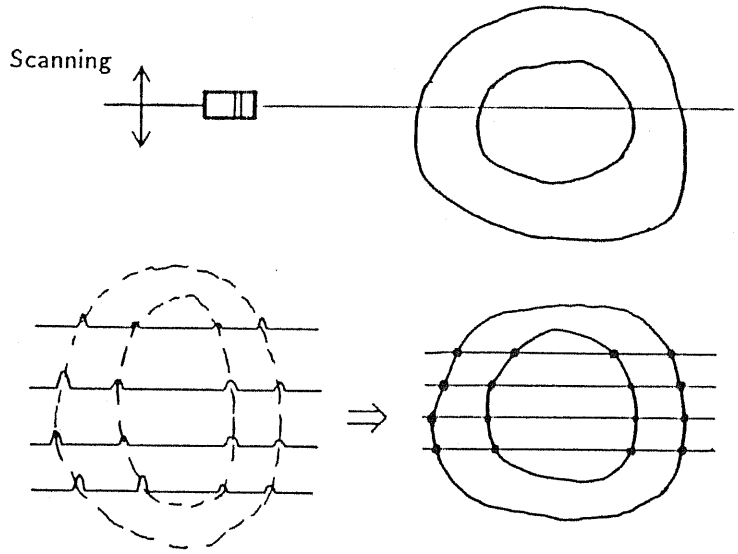

Fig. 1.2 B-scope pictures are formed by modulating the brightness of a scanning spot according to the amplitude of the video signal.

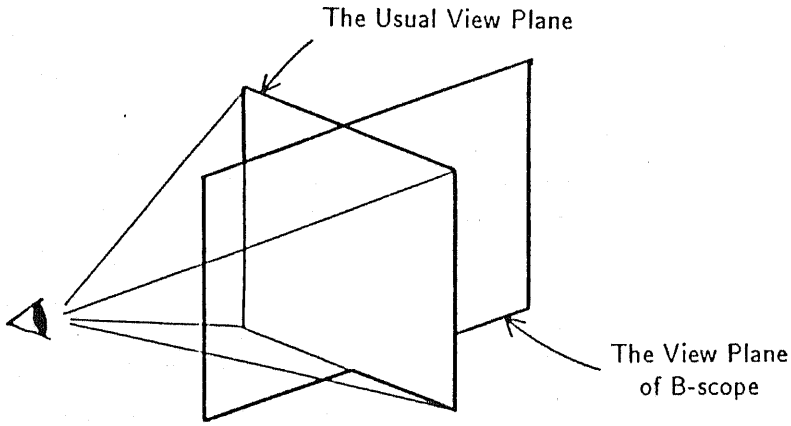

Fig. 1.3 B-scope pictures are different cuts of the object compared with what we usually see.

Up to now we have neglected an important fact. We notice that the propagation, reflection, and scattering, of the acoustic wave in the object is basically a three-dimensional phenomenon. It is not one-dimensional as

depicted in Figs. 1 and 2. However, when displaying the received signal it is treated as though it is one-dimensional, as though the echo has come from directly below the transducer and not from any other directions. Apparently there is a gap between the way the signal is generated and the way it is displayed. To make up for this gap, the commonly adopted method is to focus the acoustic beam, so as to stay as close as possible to the one-dimensional assumption.

The idea of focusing is very simple in principle (Fig. 1.4). For example, to generate a wave field which focuses at a certain point, one only has to initiate appropriately the vibration of each part of a generating system, so that the waves from each part arrive at that point at the same time. This makes the wave field at that point to have the greatest intensity, so that it is focused there. Focusing can also be applied in receiving signals. Here the process is the reverse of transmitting. The signals received by each part of a receiving system is delayed appropriately and added up, so that the waves coming from the focal point are in-phase to each other and when added, sum up to a big signal.

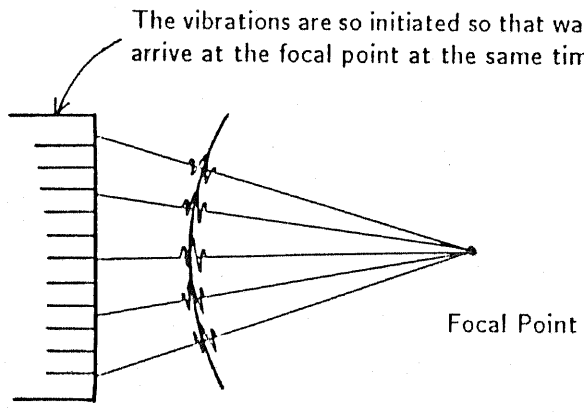

Fig. 1.4 Focusing the acoustic field.

The above description of focusing applies equally well to both optical and acoustical systems. But here comes a concept which is peculiar to acoustical systems. It is called dynamic focusing. As the propagation of acoustical waves is relatively slow (in water or typical biological tissues, about 1500 m/s), it is possible to adjust the receiving focus as fast as the echoes are being received. That is, the early echoes come from the shallow regions, and the focus is adjusted to the shallow regions. As times goes on, echoes are arriving from deeper and deeper regions, and the focal point is also moved to track the origin of the echoes. In this way the entire image can be made to be in focus. There is no counterpart in optics to this technology because the speed of light is so fast that it is impossible to do much during the arriving of the light. However the need of dynamic focusing in optics is neigher that great, because the view volume has usually a relatively small depth, unlike that of acoustics (see Fig. 1.3).

In the foregoing paragraphs we have briefly described the picture-forming process in the B-scope, with emphasis on the need to focus, the idea of dynamic focusing. The last two decades have seen great improvements in the quality of ultrasonic images. These have mainly resulted from new materials for the transducer, which can generate a pulse of broader spectrum, better electronics for amplification and improved focusing techniques (for example, dynamic focusing). But the basic aspect of the situation has not changed much. Ultrasound as a diagnostic tool is still qualitative instead of quantitative. To read the pictures and make correct diagnosis is still to some extent an art, and needs a lot of training and experience.

In the late 1970's interests in tissue characterization began to grow [2,3], which aims at characterizing the tissue with numbers or parameters. The main parameters that have been investigated include the sound velocity [4], the attenuation coefficient [5,6], and the backscattering coefficient [7]. These parameters have been found to be indicators of various kinds of pathological variations of the tissue. For example, it has been shown [6] that the attenuation coefficient is closely related to liver diseases such as alcoholic

and cardiac cirrhosis, at which the values are significantly higher than nomal values. The temperature dependence of sound velocity and attenuation coefficient has been proposed to be utilized for non-invasive measurement of temperature deep inside the body.

But as the research on tissue characterization is carried on, it quickly becomes clear that a better understanding of wave propagation in non-uniform media is necessary. We must have a better knowledge of the situation before we can say something definite. Just generating a pulse and listening to the echo, which is certainly necessary, is not enough. Even if we go back to the basic problem of imaging, we find that a knowledge of sound velocity distribution is needed to focus (either fixed or dynamic) in a non-uniform medium. Without a detailed analysis we would be at a loss as to what it is that we have measured.

On the other hand there have been active research activities on diffraction tomography and the inverse scattering problem. Direct application of the X-ray CT algorithm to ultrasound has not been successful [8,9], owing to the diffraction phenomenon which invalidates the line-integral assumption. In diffraction tomography most authors work with two-dimensional non-uniformity. The object is usually assumed to be embedded in a know uniform medium and probed by plane or spherical waves. The Born or the Rytov approximation is in most cases applied to derive the relationship between the scattered waves and the medium non-uniformity. Most of the studies are restricted to theoretical analysis or numerical simulation. The reason that only a few experimental measurements have been conducted may lie in that there are still very few systems with which the scattered waves can be easily measured at many accurately known positions. The same is true with inverse scattering studies, which also deal with the problem of inferring medium properties from scattered waves, but encompass a broader spectrum of problems, ranging from one to three dimensional problems.

In summary of this brief review, we note that technological progresses have greatly improved the qualities of ultrasonic images. However it is believed that more information useful to medical diagnosis can be derived from

the scattered waves, in more quantitative forms. Endeavor in this direction includes tissue characterization, diffraction tomography and inverse scattering. The final group is the most fundamental, yet the most difficult approach.

1.2 An Overview of the Present Research

In the previous section much of the background of this research has been laid down. To focus acoustic waves in a non-uniform medium, it is necessary to know sound velocity as a function of spatial coordinates. Sound velocity is also an important parameter for tissue characterization. In the limit of high frequency, sound velocity alone can be used to determine the ray equation (the eikonal approximation), manifesting the importance of sound velocity profile on wave propagation.

In this research we consider layered media. The simplest example of such media can be imagined as a stack of plates of different materials. Layered structures are encountered in the earth's crust, in the sea and the sea bottom. In the case of human body they can be found in the eye, the skin and the bodywall. The problem of calculating the sound velocity profile of such media from the reflected waves is certainly a special case of the more general inverse scattering problem. So in the following we will first take a bird's-eye view of this field.

There have been many research works [10,11] concerning the inverse scattering problem, with applications to exploration seismics, underwater acoustics, plasma, quantum mechanics and medical ultrasonics. According to the author's classification, the researchers can be roughly divided into 3 groups, *i.e.*, the exact solution group that pursues mathematically exact solutions [12–17], represented by mathematical physicians such as Gel'fand, Newton, Balanis, *etc.*; the approximation group that assumes weak non-uniformity and employs the Born (for example, [18,19]) or the Rytov approximation (for example, [20]), or their improved version such as the distorted Born or the distorted Rytov approximation [21–23], to find solutions; and the geometrical group

that assumes the frequency to be high enough for the wave phenomenon to be dealt with geometrically, and discusses travel path and travel time.

From the dimension of non-uniformity there can be one-, two-, and three-dimensional problems. To solve three-dimensional problems, signals need to be recorded on a surface enclosing the object [28], and the calculation requirement is in most cases too big for the computing power available today. So, although the solution to three-dimensional problems has been claimed for some years [14,26], not much seems to have been done to put it into practice. From technological restrictions as well as analytical difficulties, most research works are confined to one- or two-dimensional problems.

Concerning one-dimensional problems, since the parameters of the medium changes only in one direction, the measurement and processing is usually relatively easy. However to solve this problem exactly would require the impulse response of the medium to be known. Viewing in the frequency domain, this means knowledge of the reflection coefficient to harmonic waves of frequencies from DC to infinity. In practice we can only measure with a transducer of limited bandwidth. Another realistic problem is that transducers usually have directivities that are difficult to control. In inverse scattering measurement, waves from different directions are received by the same transducer. Without knowing from which direction the wave comes and the directivity of the transducer, it is practically impossible to use the amplitude information contained in the received signal.

With these practical considerations in mind, we considered the possibility of calculating the sound velocity profile of a one-dimensional medium from reflected signals which are band-limited and noise-corrupted. Then, layered media with plane interfaces, either parallel or non-parallel, are dealt with. In doing this we have avoided using the amplitude information which is system-dependent and unreliable, as noted above. Instead we use the time information contained in the signals. However, if the amplitude information is available, then the density of each layer can be calculated at the same time.

Roughly speaking, the measurement required by our methods can be performed in the following way, for calculating the sound velocity of each layer and the geometrical configuration of the medium. A spherical wave is generated by a poing-like transducer, and the reflected wave is received by several receivers (at least 2 for horizontally-layered media, and 3 for non-parallel layered media) at different locations. The important thing is that these receivers must not be too close together, because we are using the differences in the arrival time of the echoes to infer about the sound velocity of each layer.

When imaging organs inside the body, the non-uniform bodywall comes in between the transducer and the organ inevitably, whose influence must be accounted for. By modelling the bodywall as a layered medium and estimating the sound velocity and thickness of each layer, we can compensate for this influence, thus improving the focusing of the acoustic field in the organ. In this way it is expected that the quality of ultrasonic images can be much improved. Another field of application of this research is in tissue characterization. Sound velocity and thickness (size) of each part of the eye ball, of the skin and the organizations beneath it, may be of diagnostic values, although much of this is yet to be discovered. This research can also have applications besides in medical ultrasonics. The problem encountered in exploration seismics [24] is almost the same as the one here, except that the scale and frequency range are different. Knowledge of velocity distribution is critical to the post-stack migration of the geophysical signals [25].

With this we conclude the introduction to our research.

1.3 Organization of This Dissertation

This dissertation is composed of 7 chapters, describing in detail our research on the inverse scattering problem (ISP) on layered media.

Chapter 2 is a brief review of some of the important results concerning the ISP, including the Born and the Rytov approximation, the Goupillaud's

method of one-dimensional media, the transision matrix method, the impediography and the forward scattering approximation. This chapter not only provides some idea about how the ISP might be solved, but also reveals the difficulties of measurement: scattered waves at all frequencies need to be measured at known positions, and the amplitude information is required.

Chapter 3 describes our approach to the one-dimensional ISP. We have considered practical signals which are band-limited and noise-corrupted. Because waves are arriving from different directions and the directivity of the receiver is usually unknown, we have avoided using the amplitude information quantitatively. For this reason only the sound velocity profile is recovered. The density and the impedance profiles are left untouched. We considered layered media of either horizontal or non-parallel plane interfaces, and provided algorithms for calculating the medium parameters from observed pulse positions.

Chapter 4 deals with the problem of estimating pulse positions from the signals. A spectral fitting approach is proposed for the deconvolution of these signals, so that the original impulse responses can be obtained, from which the pulse positions can be easily read off. The error in the estimated pulse positions caused by measurement noise has been evaluated using the fluctuation of the peak position of the cross-correlation function between two pulses. Based upon this the error of the sound velocities calculated from these errorneous pulse positions has also been discussed, revealing the well-known ill-conditionedness of the ISP.

Computer simulation has been an important part of this research since the very beginning. In chapter 5 various simulations have been devised to verify the validity of the analyses and processings, or to investigate the influence of various factors.

Chapter 6 describes our experimental work. We demonstrated the deterioration of image qualities by inserting a distortion plate between the transducer and wire targets, and also showed that this can be compensated if the travel

time aberration introduced by the distortion plate is known. Next the results of measuring layered media with horizontal or non-parallel interfaces are shown, and compared to the real values.

Finally in chapter 7 we conclude this dissertation by listing up the main results, as well as some problems. Directions for further research work have been suggested.

In appendix A, the propagation of non-perpendicular plane waves in a one-dimensional medium, and in appendix B, the reflection of a spherical wave from a plane interface, have been treated. These results, though can be found in the literature, have been included for convenience and self-containedness.

2

Inverse Scattering —Various Formulations and Approaches

In this chapter we will make a survey on the inverse scattering problem, *i.e.*, the problem of estimating medium properties from the observed waves. For multi-dimensional problems the most popular formulation is still via the Born or the Rytov approximation, although there have been some important progresses in exact solution, made by for example Newton, Yagle [13,14,26,27]. For one-dimensional problems many variations exist, including continuous and discrete media, time-domain and frequency-domain analyses, exact and approximate solutions. Here we will only pick up the topics that are either relevant to our research, or helpful in developing a general idea of how the inverse problem might be solved. Our emphasis will be on the physical insight provided by these analyses to the inverse scattering problem.

2.1 The Wave Equation in Inhomogeneous Media

We begin by deriving the wave equation in inhomogeneous media. Consider a rectangular parallelpiped at $\vec{r} = (x, y, z)$, whose three sides have lengths Δx, Δy, Δz respectively (Fig. 2.1). It has density $\rho(\vec{r})$, compressibility $\kappa(\vec{r})$. The pressure and particle velocity caused by the wave motion are denoted by $p(\vec{r}, t)$ and $\vec{v}(\vec{r}, t)$.

First we will consider its motion in the x direction. From Newton's law,

$$[p(x, y, z) - p(x + \Delta x, y, z)]\, \Delta y \Delta z = \rho \Delta x \Delta y \Delta z \frac{\partial v_z}{\partial t}$$

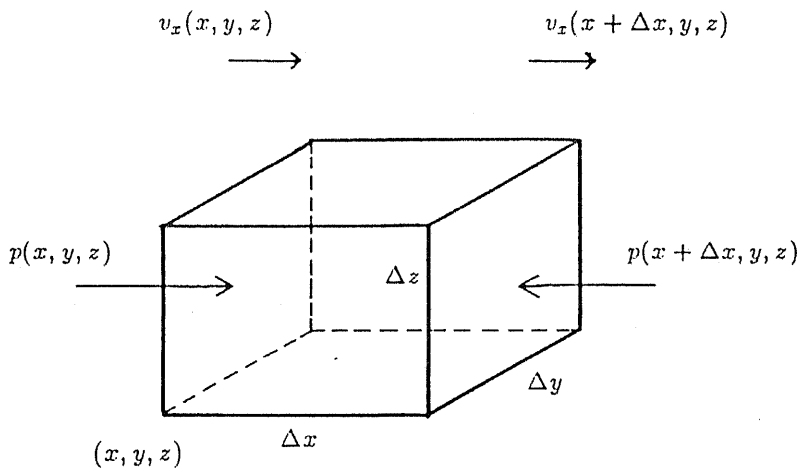

Fig. 2.1 A cell in the medium.

or

$$\frac{\partial p}{\partial x} = -\rho \frac{\partial v_x}{\partial t}$$

Simillarly we can obtain $\frac{\partial p}{\partial y} = -\rho \frac{\partial v_y}{\partial t}$, $\frac{\partial p}{\partial z} = -\rho \frac{\partial v_z}{\partial t}$, and combining these into one vector equation, we obtain

$$\nabla p = -\rho \frac{\partial \vec{v}}{\partial t} \tag{2.1}$$

Next we notice that pressure originates from the gradient of partical velocity. For example, after time Δt the parallelpiped is "compressed" in the x direction by $[v_x(x,y,z) - v_z(x+\Delta x,y,z)]\Delta t$. From the definition of compressibility, the increase of pressure can be obtained from the proportion of compression:

$$(\Delta p)_x = \frac{1}{\kappa} \frac{[v_x(x,y,z) - v_x(x+\Delta x,y,z)]\Delta t}{\Delta x}$$

where $(\Delta p)_x$ means increase of pressure due to compression in the x direction. Similar relation exists for compression in the y and z direction, and adding the effects up because

$$\Delta p = (\Delta p)_x + (\Delta p)_y + (\Delta p)_z$$

we get in the limit

$$\frac{\partial p}{\partial t} = -\frac{1}{\kappa}\nabla \cdot \vec{v} \tag{2.2}$$

The equations (2.1) and (2.2) are the basic equations that describe wave motion in a isotropic, linear, lossless medium. Combining these two equations we get

$$\nabla \cdot \left(\frac{1}{\rho}\nabla p\right) - \frac{\partial}{\partial t}\left(\kappa \frac{\partial p}{\partial t}\right) = 0 \tag{2.3}$$

Assuming that the inhomogeneous part is embedded in a homogeneous medium with parameters ρ_0 and κ_0 (Fig. 2.2), equation (2.3) can be rewritten as

$$\nabla^2 p - \frac{1}{c_0^2}\frac{\partial^2 p}{\partial t^2} = \frac{\gamma_\kappa}{c_0^2}\frac{\partial^2 p}{\partial t^2} + \nabla(\gamma_\rho \nabla p) \tag{2.4}$$

where

$$c_0^2 = \frac{1}{\kappa_0 \rho_0}, \quad \gamma_\kappa = \frac{\kappa(\vec{r}) - \kappa_0}{\kappa_0}, \quad \gamma_\rho = \frac{\rho(\vec{r}) - \rho_0}{\rho(\vec{r})} \tag{2.5}$$

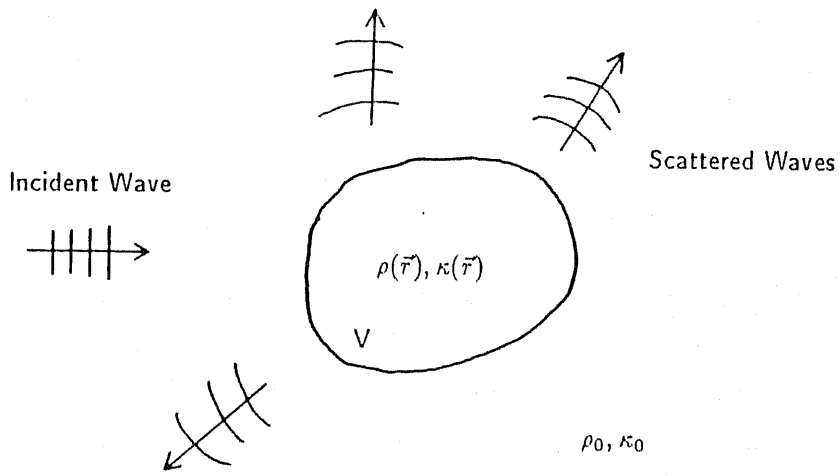

Fig. 2.2 A non-uniform medium embedded in a uniform medium.

Taking the Fourier transform with respect to time, we have

$$p_k(\vec{r}, t) = \int_{-\infty}^{+\infty} p(\vec{r}, t) e^{-i\omega t} dt, \qquad p(\vec{r}, t) = \frac{1}{2\pi}\int_{-\infty}^{+\infty} p_k(\vec{r}, \omega) e^{i\omega t} d\omega \tag{2.6}$$

Here the subscript k is p_k is used to distinguish it from its time-domain counterpart p. The equation for p_k is

$$\nabla^2 p_k + k^2 p_k = -k^2 \gamma_\kappa p_k + \nabla(\gamma_\rho \nabla p_k) \tag{2.7}$$

where $k = \omega/c_0$ is known as the wavenumber.

2.2 Solutions Based on the Born or the Rytov Approximation

First we will consider the (first-order) Born approximation. Using the Green's function, equation (2.7) can be transformed into

$$p_k(\vec{r},\omega) = \int_V \left(k^2 \gamma_\kappa p_k - \nabla(\gamma_\rho \nabla p_k)\right)_{\vec{r}_0} g(\vec{r}|\vec{r}_0) d\vec{r}_0 + p_{ik}(\vec{r},\omega) \tag{2.8}$$

where $p_{ik}(\vec{r},\omega)$ is the incident field, and $g(\vec{r}|\vec{r}_0)$ is the Green's function which is the solution to

$$\nabla^2 g + k^2 g = -\delta(\vec{r} - \vec{r}_0) \tag{2.9}$$

under the condition that it represents outgoing waves (because that the scattered waves are outgoing in the infinity). It can be shown that (forexample, [18])

$$g(\vec{r}|\vec{r}_0) = \frac{e^{ik|\vec{r}-\vec{r}_0|}}{4\pi|\vec{r}-\vec{r}_0|} \tag{2.10}$$

is the required solution.

From equation (2.8) we see that to calculate the total wave pressure, we need to know the field inside V, which is a sum of the incident and the scattered field. If we assume that the incident field is much stronger than the scattered field, then an approximate expression for the scattered field $p_{sk}(\vec{r},\omega)$ is obtained:

$$p_{sk}(\vec{r},\omega) = \int_V \left(k^2 \gamma_\kappa p_{ik} - \nabla(\gamma_\rho \nabla p_{ik})\right)_{\vec{r}_0} g(\vec{r}|\vec{r}_0) d\vec{r}_0 \tag{2.11}$$

The approximation introduced in obtaining (2.11) is the first-order Born approximation. Next we go further to solve the inverse problem. Suppose that the incident field is a plane wave, *i.e.*,

$$p_{ik} = A_k e^{ik\vec{i}\cdot\vec{r}_0}$$

where $\vec{i}$ is the unit vector along the direction of propagation (Fig. 2.3), and assume that the observation of the scattered field is made at $|\vec{r}| \gg |\vec{r}_0|$, $|\vec{r} - \vec{r}_0| \gg \frac{1}{k}$, then after some manipulations we obtain

$$p_{sk} = \frac{k^2 A_k e^{ikr}}{4\pi r} \int_V [\gamma_\kappa + \gamma_\rho(\vec{i} \cdot \vec{o})] e^{ik(\vec{i}-\vec{o})\cdot\vec{r}_0} d\vec{r}_0 \qquad (2.12)$$

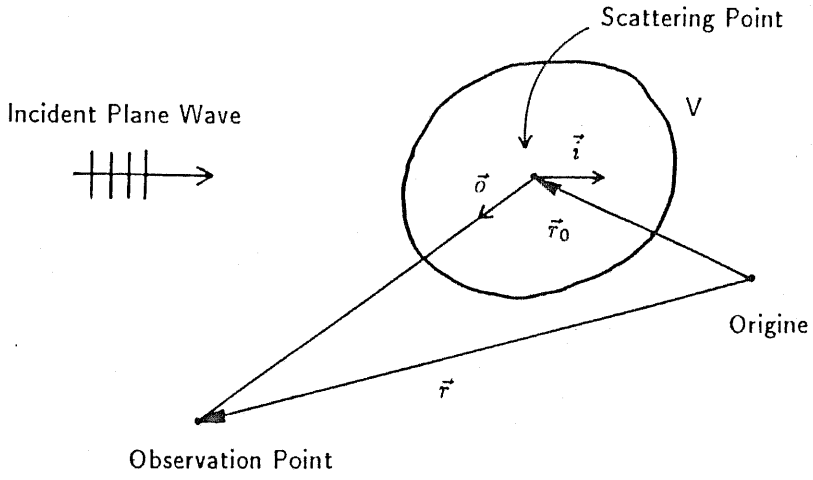

Fig. 2.3 Coordinate system for solving the inverse scattering problem

Equation (2.12) shows that measuring the scattered field gives the three-dimensional Fourier transform of $[\gamma_\kappa + \gamma_\rho(\vec{i} \cdot \vec{o})]$. Here γ_ρ and γ_κ are related to $\rho(\vec{r})$ and $\kappa(\vec{r})$ through (2.5), $\vec{i}$ and $\vec{o}$ are unit vectors along the incident and the observation direction (Fig. 2.3). This is really a remarkable result, which has appeared with slight differences in several papers [28–32], and provided the theoretical basis for some experimental measurements [33,34]. However it is hard to say that enough research has been done to evaluate its applicability to the non-uniform structures found in human body.

The validity of the first Born approximation clearly requires that the strength of the scattered field component remains small throughout the volume

of the object (scatterer). This in turn requires that both the magnitude of the material parameters γ_κ and γ_ρ be small, *and* that the total volume of the object be small. The first condition maybe violated when dealing with the inhomogeneities found in the bodywall because the sound velocity variation is rather big so that the incident wave field cannot be assumed to be *uninfluenced* by the existence of the inhomogeneity (at least the phase front is distorted). The second condition is more likely to be violated by the large volume (a linear scale of 100mm, which contains about 200 wavelengths, is typical) we wish to image.

There are some trials to improve upon the first Born approximation. One is known as the distorted Born approximation, which has several forms. For example one can calculate the scattered field using (2.12) first. The sum of this result and the incident field is a better approximation to the total field, and can be substituted into the right side of (2.9) to make a second evaluation of the scattered field [21,35]. In solving the inverse problem one can first calculate the medium parameters using the simple Born approximation. Then the total field inside the inhomogeneous object can be calculated more accurately, which in turn improves the evaluation of the medium parameters. One may also want to use the obtained medium parameters as a new background medium (instead of sticking to a uniform medium all the time). In this case not only the wave field, but also the Green's function in (2.9) needs to be updated. Some computer simulation results are available on this topic [23].

Another substitution to the Born approximation is the Rytov approximation [36–38]. Instead of dealing with p_k directly, we put $p_k \equiv e^{u_k}$ in (2.8) and obtain an equation for u_k, which is

$$\nabla^2 u_k + \nabla u_k \cdot \nabla u_k + k^2 = \\ -\gamma_\kappa k^2 + \gamma_\rho[\nabla^2 u_k + \nabla u_k \cdot \nabla u_k] + \nabla\gamma_\rho \cdot \nabla u_k \qquad (2.13)$$

The incident wave field (when the inhomogeneity is absent) u_{ik} satisfies the equation

$$\nabla^2 u_{ik} + \nabla u_{ik} \cdot \nabla u_{ik} + k^2 = 0 \qquad (2.14)$$

Putting $u_k = u_{ik} + u_1$ and omitting the higher order terms of u_1, we get

$$\nabla^2 u_1 + 2\nabla u_{ik} \cdot \nabla u_1 = -k^2(\gamma_\rho + \gamma_\kappa) + \nabla\gamma_\rho \cdot \nabla u_{ik} \tag{2.15}$$

The Green's function of (2.15) depends upon the incident field u_{ik}. In the case of plane waves $u_{ik} = ik\vec{i}\cdot\vec{r}$, the Green's function is

$$g_k(\vec{r}|\vec{r}_0, \vec{i}) = \left.\frac{e^{ik(r_1 - \vec{i}\cdot\vec{r})}}{4\pi r_1}\right|_{\vec{r}_1 = \vec{r} - \vec{r}_0} \tag{2.16}$$

which satisfies

$$\nabla^2 g_k + 2ik\vec{i}\cdot\nabla g_k = -\delta(\vec{r} - \vec{r}_0) \tag{2.17}$$

Using (2.16), the solution to (2.15) can be obtained which, under the condition of far field observation, becomes

$$u_1 = \frac{k^2 e^{ik(r - \vec{i}\cdot\vec{r})}}{4\pi r}\int[\gamma_\kappa + (\vec{i}\cdot\vec{o})\gamma_\rho]e^{ik(\vec{i}-\vec{o})\cdot\vec{r}}d\vec{r}_0 \tag{2.18}$$

We notice that the solutions (2.12) and (2.18) are almost identical. This is not a mere coincidence. In fact it can be shown that, if one puts $p_k = p_{ik}(1+u_1)$ and uses the Born approximation to solve for u_1, one will obtain an equation which is exactly the same as (2.15). The difference is that in the Rytov approximation one has put $p_k = e^{u_{ik}}e^{u_1}$ which is

$$p_k = e^{u_{ik}}\left(1 + u_1 + \frac{1}{2!}u_1^2 + \frac{1}{3!}u_1^3 + \cdots\right).$$

So, although the same u_1 needs to be solved in the first Born and the first Rytov approximation, it appears in different forms in the final solution. It should be noted that this coincidence no longer exists when it comes to higher order approximations.

There has been much controversy concerning the relative accuracy of the Born and the Rytov approximation [38]. Now the general opinion is that the latter can be applied to stronger non-uniformity or greater volume of the object. But the former has its appeal of linearity, simplicity in its idea

and easiness of extension to higher order approximations. So both are in use according to the situation.

However, the purpose of this section is in obtaining some idea about how the inverse scattering problem might be solved, even though approximately. We can also learn from these analyses what kind of data need to be collected to solve a three-dimensional problem. It is known that to invert a three-dimensional Fourier transform, which is just what should be done in solving (2.12) or (2.18) for $[\gamma_\kappa + (\vec{i}\cdot\vec{o})\gamma_\rho]$, we must know the transform at any point in the three-dimensional frequency domain. Now the frequency domain vector in these equations is $k(\vec{i}-\vec{o})$. To meet the above requirement, the vector $\vec{i}-\vec{o}$ must have chances of pointing to any direction and the wavenumber k must be varied from zero to infinity. If the incident vector $\vec{i}$ is fixed, then the observation vector $\vec{o}$ must vary over the entire solid angle, *i.e.*, the scattered field must be observed on a surface enclosing the object. Varying k from zero to infinity means to vary the frequency of the probing wave from zero to infinity, since $k = \omega/c_0$; or alternatively, to measure the scattered waves caused by an impulse input.

2.3 One-dimensional Forward Scattering Problem

When it comes to the one-dimensional problem, there are many more varieties in its solution. The forward problem, *i.e.*, to calculate the reflected waves caused by a given input, typically an impulse input, can be solved in several ways by numerical methods. One approach is to calculate the frequency response of the medium and use the inverse Fourier transform to obtain the impulse response. Another approach is to use the Goupillaud's model, which is well-known to the seismic circle. By analysing this model much can be learnt about the reflected and the transmitted waves. Still another approach to solving the forward problem of either one- or multi-dimensional medium is the so-called k-space method [39,40] which, although very interesting, will not be discussed here.

In this section we will discuss briefly the two former approaches only, because of the physical insight they can provide. The Goupillaud's method will also be useful in our computer simulation studies.

Now we begin by considering the one-dimensional wave equation. From equations (2.1) and (2.2) we have

$$\begin{cases} \dfrac{\partial p}{\partial x} = -\rho(x)\dfrac{\partial v}{\partial t} \\ \dfrac{\partial v}{\partial x} = -\kappa(x)\dfrac{\partial p}{\partial t} \end{cases} \tag{2.19}$$

Here we have assumed wave motion in the x-direction only (thus, perpendicular plane waves), for the sake of simplicity. In Appendix A we have shown that non-perpendicular plane waves can be treated by introducing an equivalent sound velocity, whereas non-plane waves can be dealt with by decomposing them into sums of plane waves using the Fourier transformation (see Appendix B, [18,41]).

Since we are going to calculate the impulse resopnse of the medium from its reflection coefficient for harmonic waves, we will suppose the time depencence of any quantity to be $e^{i\omega t}$, so that $\frac{\partial}{\partial t}$ can be replaced by multiplications with $i\omega$, and (2.19) becomes

$$\begin{cases} \dfrac{\partial p}{\partial x} = -i\omega\rho v \\ \dfrac{\partial v}{\partial x} = -i\omega\kappa p \end{cases} \tag{2.20}$$

The first step is to decompose the wave motion into down-going and up-going components [42]. Examining the case of uniform medium will give us hint as for how to do it. In a uniform medium the down-going pressure and velocity components will look like $p^+(t - x/c)$ and $v^+(t - x/c)$. Using (2.19) we obtain immediately $v^+ = p^+/\rho c$. Similarly, for up-going waves we have $v^- = -p^-/\rho c$. The total pressure and partical velocity are sums of the individual components:

$$p = p^+ + p^-, \quad v = v^+ + v^- = \frac{1}{\rho c}(p^+ - p^-) \tag{2.21}$$

The relationship (2.21) suggests a transformation from (p, v) to (p^+, p^-), which guarantee that, in a uniform medium, if there are down-going waves only, the p^- component will diminish, whereas if there are up-going waves only, the p^+ component will diminish. These can be made clearer if we solve for p^+ and p^-,

$$p^+ = \frac{1}{2}(p + \rho c v), \quad p^- = \frac{1}{2}(p - \rho c v).$$

Using the transformation (2.21), the wave equation (2.20) becomes

$$\frac{d}{dx}\begin{pmatrix} p^+ \\ p^- \end{pmatrix} = \left[jk \begin{pmatrix} -1 & 0 \\ 0 & 1 \end{pmatrix} + \alpha \begin{pmatrix} 1 & -1 \\ -1 & 1 \end{pmatrix} \right] \begin{pmatrix} p^+ \\ p^- \end{pmatrix} \tag{2.22}$$

where

$$\begin{aligned} k(x) &= \frac{\omega}{c(x)}, \quad \alpha = \frac{1}{2}\frac{d \ln z(x)}{dx} \\ c(x) &= \frac{1}{\sqrt{\rho(x)\kappa(x)}}, \quad z(x) = \rho(x)c(x) = \sqrt{\frac{\rho(x)}{\kappa(x)}} \end{aligned} \tag{2.23}$$

Equation (2.22) can be solved numerically by dividing the x-axis into short enough intervals and assuming that $k(x)$ and $\alpha(x)$ are constants in each interval. For instance, for the interval $[j\Delta x, (j+1)\Delta x]$, equation (2.22) takes the form

$$\frac{d}{dx}\begin{pmatrix} p^+ \\ p^- \end{pmatrix} = A(j\Delta x)\begin{pmatrix} p^+ \\ p^- \end{pmatrix} \equiv A_j \begin{pmatrix} p^+ \\ p^- \end{pmatrix} \tag{2.24}$$

which can be solved since A_j is assumed to be constant,

$$\begin{pmatrix} p^+ \\ p^- \end{pmatrix}_{(j+1)\Delta x} = e^{A_j \Delta x} \begin{pmatrix} p^+ \\ p^- \end{pmatrix}_{j\Delta x} \tag{2.25}$$

Applying the above calculations repeatedly, we arrive at

$$\begin{pmatrix} p^+ \\ p^- \end{pmatrix}_{J\Delta x} = e^{A_{J-1}\Delta x} \cdot e^{A_{J-2}\Delta x} \cdots e^{A_0 \Delta x} \begin{pmatrix} p^+ \\ p^- \end{pmatrix}_0 \tag{2.26}$$

where J is the last interval beyond which the mediume is assumed to be homogeneous. Since no waves are reflected from beneath the Jth interval, $(p^-)_{J\Delta x} = 0$, and

$$\begin{aligned} \begin{pmatrix} p^+ \\ p^- \end{pmatrix}_0 &= e^{-A_0 \Delta x} \cdot e^{-A_1 \Delta x} \cdots e^{-A_{J-1}\Delta x} \begin{pmatrix} p^+(J\Delta x) \\ 0 \end{pmatrix} \\ &\equiv \begin{pmatrix} M_{00} & M_{01} \\ M_{10} & M_{11} \end{pmatrix} \begin{pmatrix} p^+(J\Delta x) \\ 0 \end{pmatrix} \end{aligned} \tag{2.27}$$

From this result,

$$\begin{cases} p^+(0) = M_{00}p^+(J\Delta x) \\ p^-(0) = M_{10}p^+(J\Delta x) \end{cases} \qquad \frac{p^-(0)}{p^+(0)} = \frac{M_{10}}{M_{00}} \tag{2.28}$$

i.e., the reflection coefficient can be calculated at the first interval. To obtain the impulse resopnse, one only has to calculate the reflection coefficient for all the necessary frequencies and perform inverse Fourier transform to the results.

This approach, though very straight-forward in its idea, needs relatively much calculation. It neither reveals much about the properties of the reflected and the transmitted waves. Next we will turn to the Goupillaud's method [42–45], which also calculates the impulse response of a one-dimensional medium.

In the Goupillaud's model the medium is also divided into thin layers along the x direction, but the thickness of each layer varies to keep the propagation time in each layer a constant. These thicknesses are assumed to be small enough so that the density and the sound velocity of each layer are also approximately constant, and the reflection occurs only at the interfaces among the layers. If the incident wave is an impulse, the reflected signal will also be a series of impulse, whose strength may be denoted by $R_0, R_1, R_2, \cdots$. The time interval between two successive impulses is just the round-trip time of one layer. If z is used to represent this delay, then the received signal can be written as

$$R(z) = R_0 + R_1 z + R_2 z^2 + \cdots \tag{2.29}$$

In this system of notation, the impulse input becomes $I(z) = 1$.

Now we will consider the problem of calculating $R(z)$ from medium parameters $\rho_0, c_0, \rho_1, c_1, \cdots$ (Fig. 2.4). Denote the down-going pressure component by D_k and the up-going component by U_k *at the begining of the kth layer*(Fig. 2.4). At the bottom of the same layer these components are dashed. They are related by

$$D'_{k-1} = \sqrt{z}D_{k-1}, \quad U'_{k-1} = \frac{1}{\sqrt{z}}U_k \tag{2.30}$$

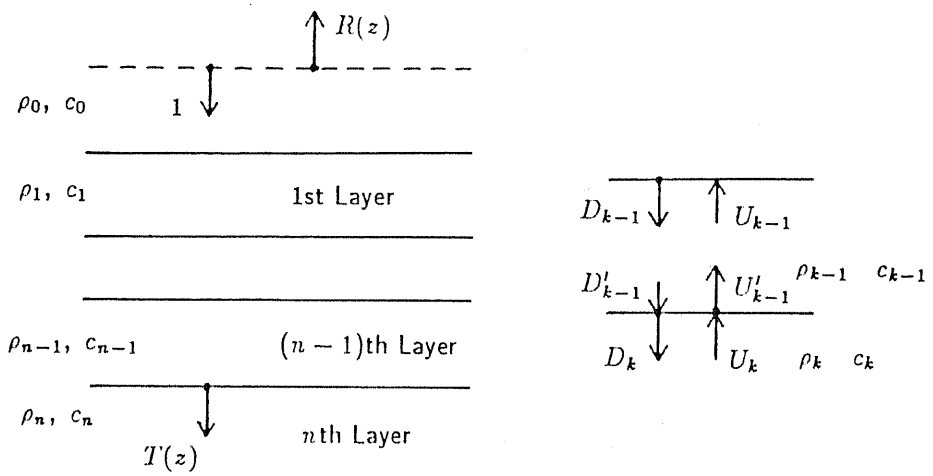

Fig. 2.4 The Goupillaud's model of a one-dimensional medium.

where $\sqrt{z}$ represents the one-way travel time of one layer. The relationship between D'_{k-1}, U'_{k-1}, D_k, U_k can be established from the requirement that the pressure and the particle velocity should be continueous across the interface. From (2.21)

$$\begin{cases} D'_{k-1} + U'_{k-1} = D_k + U_k \\ \dfrac{1}{\rho_{k-1}c_{k-1}}(D'_{k-1} - U'_{k-1}) = \dfrac{1}{\rho_k c_k}(D_k - U_k) \end{cases} \tag{2.31}$$

which can be rewritten as

$$\begin{pmatrix} U_k \\ D_k \end{pmatrix} = \frac{1}{t_k}\begin{pmatrix} 1 & -r_k \\ -r_k & 1 \end{pmatrix}\begin{pmatrix} U'_{k-1} \\ D'_{k-1} \end{pmatrix} \tag{2.32}$$

where

$$t_k = \frac{2\rho_{k-1}c_{k-1}}{\rho_k c_k + \rho_{k-1}c_{k-1}}, \quad r_k = \frac{\rho_k c_k - \rho_{k-1}c_{k-1}}{\rho_k c_k + \rho_{k-1}c_{k-1}} = 1 - t_k \tag{2.33}$$

Combining (2.30) and (2.32),

$$\begin{pmatrix} U_k \\ D_k \end{pmatrix} = \frac{1}{t_k\sqrt{z}}\begin{pmatrix} 1 & -r_k z \\ -r_k & z \end{pmatrix}\begin{pmatrix} U_{k-1} \\ D_{k-1} \end{pmatrix} \tag{2.34}$$

Applying (2.34) repeatedly we obtain

$$\begin{pmatrix} U_k \\ D_k \end{pmatrix} = \frac{1}{\prod_{i=1}^{k} t_i \sqrt{z^k}} \times$$

$$\begin{pmatrix} 1 & -r_k z \\ -r_k & z \end{pmatrix} \begin{pmatrix} 1 & -r_{k-1} z \\ -r_{k-1} & z \end{pmatrix} \cdots \begin{pmatrix} 1 & -r_1 z \\ -r_1 & z \end{pmatrix} \begin{pmatrix} U_0 \\ D_0 \end{pmatrix} \tag{2.35}$$

The multiplication of the k matrixes in (2.35) can be performed in an efficient way. By inspecting

$$\begin{pmatrix} 1 & -r_2 z \\ -r_2 & z \end{pmatrix} \begin{pmatrix} 1 & -r_1 z \\ -r_1 & z \end{pmatrix} = \begin{pmatrix} 1 + r_1 r_2 z & -r_1 z - r_2 z^2 \\ -r_2 - r_1 z & z^2 + r_1 r_2 z \end{pmatrix}$$
$$= \begin{pmatrix} 1 + r_1 r_2 z & z^2 \left(-r_2 - r_1 \frac{1}{z}\right) \\ -r_2 - r_1 z & z^2 \left(1 + r_1 r_2 \frac{1}{z}\right) \end{pmatrix}$$

we get the hint of trying a result of the following form:

$$\begin{pmatrix} 1 & -r_{k-1} z \\ -r_{k-1} & z \end{pmatrix} \begin{pmatrix} 1 & -r_{k-2} z \\ -r_{k-2} & z \end{pmatrix} \cdots \begin{pmatrix} 1 & -r_1 z \\ -r_1 & z \end{pmatrix} =$$
$$\begin{pmatrix} F_{k-1}(z) & z^{k-1} G_{k-1}\left(\frac{1}{z}\right) \\ G_{k-1}(z) & z^{k-1} F_{k-1}\left(\frac{1}{z}\right) \end{pmatrix} \tag{2.36}$$

whose correctness can be verified by showing that the multiplication of another matrix to the right of (2.36) does not destroy this form:

$$\begin{pmatrix} 1 & -r_k z \\ -r_k & z \end{pmatrix} \begin{pmatrix} F_{k-1}(z) & z^{k-1} G_{k-1}\left(\frac{1}{z}\right) \\ G_{k-1}(z) & z^{k-1} F_{k-1}\left(\frac{1}{z}\right) \end{pmatrix} =$$
$$\begin{pmatrix} F_{k-1}(z) - r_k z G_{k-1}(z) & z^k \left[-r_k F_{k-1}\left(\frac{1}{z}\right) + \frac{1}{z} G_{k-1}\left(\frac{1}{z}\right)\right] \\ -r_k F_{k-1}(z) + z G_{k-1}(z) & z^k \left[F_{k-1}\left(\frac{1}{z}\right) - r_k \frac{1}{z} G_{k-1}\left(\frac{1}{z}\right)\right] \end{pmatrix} \tag{2.37}$$

So, if we put

$$\begin{cases} F_k(z) = F_{k-1}(z) - r_k z G_{k-1}(z) \\ G_k(z) = -r_k F_{k-1}(z) + z G_{k-1}(z) \end{cases} \tag{2.38}$$

we see that the form is preserved.

By this result we can write down

$$\begin{pmatrix} U_n \\ D_n \end{pmatrix} = \frac{1}{\prod_{k-1}^{n} t_k \sqrt{z^n}} \begin{pmatrix} F_n(z) & z^n G_n\left(\frac{1}{z}\right) \\ G_n(z) & z^n F_n\left(\frac{1}{z}\right) \end{pmatrix} \begin{pmatrix} U_0 \\ D_0 \end{pmatrix} \tag{2.39}$$

From boundary conditions (Fig. 2.4)

$$U_0 = R(z), \quad D_0 = 1, \quad U_n = 0, \quad D_n = T(z) \tag{2.40}$$

it is required that $F_n(z)$ does not have zero points inside the unit circle (for example,

$$\frac{1}{2-z} = \frac{1}{2} + \frac{z}{4} + \frac{z^2}{8} + \cdots$$

converges, while

$$\frac{1}{1-2z} = 1 + 2z + 4z^2 + \cdots$$

diverges). This is known as the minimum-phase condition. As is well-known, a minimum-phase signal can be uniquely determined from its spectrum [46]. That is to say that, if $A(z)$ is known to be minimum-phased and $B(z) = A(z)\ A(z^{-1})$ is given, then $A(z)$ can be uniquely determined from $B(z)$. We can apply this theorem here, to show that the transmitted signal $T(z)$ can be determined from the reflected signal $R(z)$. From (2.46) and (2.44) it follows that

$$R(z)R\left(\frac{1}{z}\right) = \frac{G_n\left(\frac{1}{z}\right)G_n(z)}{F_n(z)F_n\left(\frac{1}{z}\right)} = 1 - \frac{\prod t_k t_k'}{F_n(z)F_n\left(\frac{1}{z}\right)}$$

$$T(z)T\left(\frac{1}{z}\right) = \frac{\prod t_k'^2}{F_n(z)F_n\left(\frac{1}{z}\right)} = \frac{\prod t_k t_k' \prod t_k'/t_k}{F_n(z)F_n\left(\frac{1}{z}\right)} = \frac{\rho_n c_n}{\rho_0 c_0}\frac{\prod t_k t_k'}{F_n(z)F_n\left(\frac{1}{z}\right)}$$

Thus

$$1 - R(z)R\left(\frac{1}{z}\right) = \frac{\rho_0 c_0}{\rho_n c_n}T(z)T\left(\frac{1}{z}\right) \tag{2.47}$$

Since $F_n(z)$ can be determined uniquely from $F_n(z)F_n(1/z)$, so can $T(z)$ from $T(z)T(1/z)$. Except for the constant $\rho_0 c_0/\rho_n c_n$ (actually this constant can also be deduced from $R(z)$), equation (2.47) says that $T(z)T(1/z)$ can be obtained from $R(z)R(1/z)$. So we may conclude that the transmitted signal $T(z)$ can be uniquely determined from the reflected signal $R(z)$. The reverse is not true. That is, $R(z)$ is not uniquely determined by $T(z)$, because there is no guarantee that $G_n(z)$ will be minimum-phased. In fact it can well be non-minimum-phased.

2.4 One-dimensional Inverse Scattering Problem

In the previous section we have described two approaches to solving the one-dimensional forward scattering problem. One is a frequency-domain method while another is the Goupillaud's method. In this section we will consider the inverse problem. First the possibility of calculating medium parameters from the observed scattered (reflected) signals will be examined. Next we will consider several proposed approximate solutions to the inverse problem, including the impediography, the forward scattering approximation.

On considering the one-dimensional inverse scattering problem, the first natural question is, what can be recovered from the impulse response of the medium when probed from one direction only? Since non-perpendicular incident waves can be equivalently treated by defining a new compressibility or sound velocity (see Appendix A), we only have to consider the perpendicular incidence case. In this case the reflection is determined solely by the acoustic impedance $z(x) = \rho(x)c(x)$. For instance, so long as $z(x)$ remains constant, no reflection can be observed even if $\rho(x)$ and $c(x)$ vary with x. This observation indicates that, from one impulse response measured at a particular direction one cannot reconstruct the two profiles $\rho(x)$ and $c(x)$ as functions of depth simultaneously. The more accurate answer to this question is, impulse response of one direction can be used to reconstruct the (equivalent) acoustic impedance as a function of travel time, while two impulse responses of different directions can be used to reconstructboth the density and the sound velocity as functions of depth. This fact will become clear as our analysis goes on.

First we will introduce an inversion procedure provided by the Goupillaud's model [45,47]. Equation (2.34) is rewritten here:

$$\begin{pmatrix} U_k(z) \\ D_k(z) \end{pmatrix} = \frac{1}{(1-r_k)\sqrt{z}} \begin{pmatrix} 1 & -r_k z \\ -r_k & z \end{pmatrix} \begin{pmatrix} U_{k-1}(z) \\ D_{k-1}(z) \end{pmatrix} \tag{2.34}$$

Referring to Fig. 2.4, U_{k-1} and D_{k-1} are the up-going the down-going impulse trains observed at the beginning of the $(k-1)$th layer. Intuition tells us that the first impulse in U_{k-1} originates from the reflection of the first impulse in

D_{k-1}, by the interface between the $(k-1)$th and kth layers. So the reflection coefficient r_k is given by the ratio of the amplitudes of these two impulses. Once r_k is obtained the equation (2.34) can be applied to find (U_k, D_k), from which r_{k+1} can be calculated, using the first two pulses of (U_k, D_k) again. Thus we may proceed until all the r_k are determined. The initialization of this process is certainly made by $U_0(z) = R(z)$, $D_0(z) = 1$, where $R(z)$ is the measured impulse response.

If all the r_k have been determined and if ρ_0, c_0 (see Fig. 2.4), or rather their product $z_0 = \rho_0 c_0$ is given, then z_1, z_2, $\cdots$, z_n can be easily calculated using (2.33). But, as we have no knowledge about c_k, the thickness of each layer in the Goupillaud's model is unknown. However the round-trip travel time of each layer is known — it is just the time interval between the impulses in $R(z)$. So, by this procedure the impedance profile can be reconstructed from the impulse response, but only as a function of the travel-time. Although very simple, this procedure is exact in principle, which is a remarkable fact. Its essential feature is a downward continuation of the wave phenomenon observed at the surface.

Next we will discuss three approximate solutions to the one-dimensional inverse scattering problem. The interesting thing is that, although these three solutions have been derived from different considerations, they lead to the same answer. This same approximation has also been arrived at from other start points [48], and it has also been shown that if the relative variations of the medium parameters have the order ϵ, then the term that has been omitted in deriving this solution is of the order of ϵ^3 [49].

The first derivation can be obtained by intuition. Consider the one-dimensional medium of Fig. 2.5. the reflection coefficient at depth x is approximately

$$\frac{z(x+\Delta x) - z(x)}{z(x+\Delta x) + z(x)} \approx \frac{1}{2z(x)} \frac{dz(x)}{dx} \Delta x \tag{2.48}$$

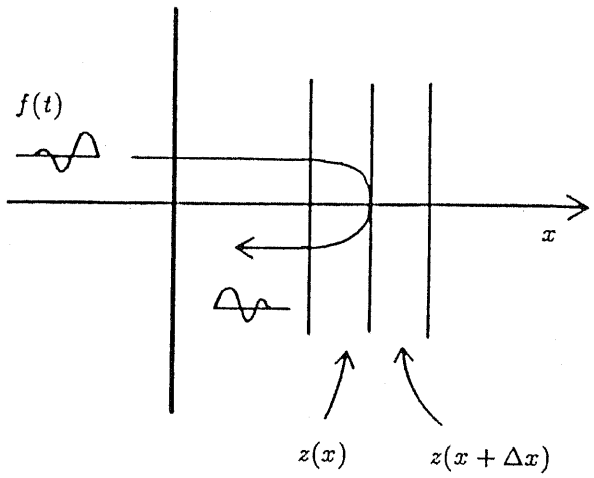

Fig. 2.5 A one-dimensional medium.

Suppose that there is a pressure variation $f(t)$ at the surface, which propagates into the medium. If we ignore the loss and dispersion it suffers in this process, at depth x the pressure variation will be $f(t-\tau(x))$, where

$$\tau(x) = \int_0^x \frac{1}{c(\xi)} d\xi \tag{2.49}$$

is the one-way travel time from the surface to depth x. The reflected signal travels back to the surface again, suffering the same amount of loss and dispersion, which is agina ignored. Thus the reflected signal can be approximated by

$$r(t) \approx \int_0^\infty f(t-2\tau(x)) \frac{1}{2z(x)} \frac{dz(x)}{dx} dx \tag{2.50}$$

This is known as the impediography approximation [50]. If the integration variable is changed from x to τ, then

$$r(t) \approx \int_0^\infty f(t-2\tau) \frac{1}{2z(\tau)} \frac{dz(\tau)}{d\tau} d\tau \tag{2.51}$$

where $z(\tau) \equiv z[\tau(x)]$ means the impedance at a depth whose one-way travel time from the surface is τ.

The inversion of (2.51) under the condition $f(t) = \delta(t)$ (*i.e.*, the input is an impulse) is straightforward, and gives

$$z(t) = z(0) \exp\left[4 \int_0^t r(2\tau) d\tau\right] \tag{2.52}$$

Note that the $r(t)$ in (2.52) is the impulse response as $f(t)$ equals $\delta(t)$.

Another derivation starts with the wave equation (2.22). By changing the variable from x to τ using (2.49), the wave equation becomes

$$\begin{cases} \dfrac{dp^+(\tau)}{d\tau} = (-i\omega + \beta(\tau))p^+(\tau) - \beta(\tau)p^-(\tau) \\ \dfrac{dp^-(\tau)}{d\tau} = -\beta(\tau)p^+(\tau) + (i\omega + \beta(\tau))p^-(\tau) \end{cases} \tag{2.53}$$

where

$$\beta(\tau) = \frac{1}{2} \frac{d \ln z(\tau)}{d\tau} \tag{2.54}$$

If we assume that the down-going wave p^+ is much stronger than the up-going wave p^-, then in the equation of $\dfrac{dp^+(\tau)}{d\tau}$ the term $-\beta p^-$ can be omitted,

$$\frac{dp^+(\tau)}{d\tau} \approx (-i\omega + \beta(\tau))p^+(\tau) \tag{2.55}$$

This approximation has been given the name forward scattering approximation [51,52]. Equation (2.55) can be solved under the boundary condition $p^+(0) = 1$, giving

$$p^+(\tau) = \exp\left[-i\omega\tau + \int_0^\tau \beta(u) du\right] \tag{2.56}$$

On substituting this result back to the second equation of (2.53), $p^-(\tau)$ can also be solved under the condition $p^-(+\infty) = 0$, which means that no echo comes from the infinity. The solution is

$$p^-(\tau) = e^{i\omega\tau + \int_0^\tau \beta(u) du} \int_\tau^{+\infty} \beta(u) e^{-i2\omega u} du \tag{2.57}$$

Our interest is in the up-going wave at $\tau = 0$,

$$p^-(0) = \int_0^{+\infty} \beta(u) e^{-i2\omega u} du \tag{2.58}$$

Since $p^+(0) = 1$, the reflection coefficient for frequency ω is clearly

$$R(\omega) = \frac{p^-(0)}{p^+(0)} = \int_0^{+\infty} \frac{1}{2} \frac{d \ln z(\tau)}{d\tau} e^{-i2\omega\tau} d\tau \tag{2.59}$$

For arbitrary incident waveform $f(t)$, the reflected signal can be obtained using the Fourier transform:

$$\begin{aligned} r(t) &= \frac{1}{2\pi} \int_{-\infty}^{+\infty} F(\omega) R(\omega) e^{i\omega t} d\omega \\ &= \frac{1}{2\pi} \int_{-\infty}^{+\infty} \left(\int_{-\infty}^{+\infty} f(u) e^{-i\omega u} du \right) \left(\int_{-\infty}^{+\infty} \frac{1}{2} \frac{d \ln z(\tau)}{d\tau} e^{-i2\omega\tau} d\tau \right) e^{i\omega t} d\omega \\ &= \int_0^{+\infty} \frac{1}{2} \frac{d \ln z(\tau)}{d\tau} \cdot \int_0^{+\infty} \left(\frac{1}{2\pi} \int_{-\infty}^{+\infty} e^{i\omega(t-u-2\tau)} d\omega \right) f(u) du \cdot d\tau \\ &= \int_0^{+\infty} \frac{1}{2} \frac{d \ln z(\tau)}{d\tau} \int_0^{+\infty} \delta(t-u-2\tau) f(u) du \cdot d\tau \\ &= \int_0^{+\infty} f(t-2\tau) \frac{1}{2} \frac{d \ln z(\tau)}{d\tau} d\tau \end{aligned} \tag{2.60}$$

which is exactly the same as the intuitive result (2.51).

Another investigation from the Riccati's equation is also possible. Defining a new variable $R(\tau) \equiv p^-(\tau)/p^+(\tau)$, its equation can be obtained from (2.53):

$$\frac{dR}{d\tau} = \frac{1}{p^+} \frac{dp^-}{d\tau} - \frac{p^-}{p^{+2}} \frac{dp^+}{d\tau} = 2i\omega R - \beta(1 - R^2) \tag{2.61}$$

This is known as the Riccati's equation, whose general form is

$$\frac{dy}{dx} + p(x) y^2 + q(x) y + r(x) = 0.$$

As the general solution for arbitrary $\beta(\tau)$ cannot be obtained, we solve it under the condition $R^2 \ll 1$ by the following approximation:

$$\frac{dR}{d\tau} \approx 2i\omega R - \beta \tag{2.62}$$

The solution is clearly the same as that given by (2.59).

An improvement upon this solution has been proposed [53]. Dividing (2.61) by $(1 - R^2)$, we get

$$\frac{1}{1 - R^2} \frac{dR}{d\tau} = 2i\omega \frac{R}{1 - R^2} - \beta$$

If R' is defined as $\tanh R$, since $\frac{dR'}{dR} = \frac{1}{1-R^2}$, in the neighborhood of $R = 0$, the approximation $R' \approx R/(1-R^2)$ is adopted and

$$\frac{dR'}{d\tau} \approx 2i\omega R' - \beta \tag{2.63}$$

is obtained. Although equations (2.62) and (2.63) have exactly the same form, their contents are apparently different, because of the usage of the non-linear hyperbolic tangent. There are reports on improved accuracy by virture of this nonlinear transformation [53,54]. The modified procedure can be outlined as the following. Given the impulse response $r(t)$, the first thing is to Fourier transform it to get $R(\omega)$, from which $R'(\omega) = \tanh R(\omega)$ is calculated. Then by the inverse Fourier transformation, $r'(t)$ can be obtained from $R'(\omega)$, which is then used in place of $r(t)$ in (2.52) to calculate the impedance profile.

2.5 A Summary of the Inverse Scattering Theory

On surveying the literature it is noticed that the research on the inverse scattering problem can be roughly divided into 3 groups, *i.e.*, the exact solution group that pursues theoretically exact solutions, represented by mathematical physicians such as Gel'fand, Newton, Balanis; the approximation group that assumes weak non-uniformity and employs the Born or the Rytov approximation (or their improved version such as the distorted Born or Rytov approximation) to find solutions; and the geometrical group that assumes the frequency to be high enough for the wave phenomenon to be dealt with geometrically, and discusses travel time and travel path in detail.

These approaches have their merits and demerits. The exact solutions are fundamental and important, but are usually difficult to obtain, to understand and to implement. The weakly inhomogeneous approximations are much easier to handle with, and have lead to the proposal of diffraction tomography. The problem is that very few experimental measurements have been performed, and we do not know how well these approximations apply to the reality, for example, to the bodywall in the abdomen. The possible reason for this

is that measuring and processing the three-dimensionally scattered waves is still not an easy job with present-day technology. However, researches in this direction seems most likely to lead to imaging non-uniform media by inverse scattering. The geometrical approaches usually deal with much simpler, usually structural non-uniformities. For this reason the data that need to be collected and processed are not that many. The results of inversion may not be directly of interest by themselves, but they can be used to facilitate the interpretation of signals which come from beneath the structural non-uniformity. In medical ultrasonics, the necissity of this kind of interpretation manifests itself through the need of focusing the sonic beam in the organs.

The analysis and approaches introduced in this chapter form the basis, as well as part of the motivation of our research. Although they can be found in the literature, we have tried to present them in a brief, unified and easy-to-understand form.

3

Inverse Scattering in Layered Media

As discussed in the previous chapter, multi-dimensional inverse scattering problems encountered in medical ultrasonics are still too difficult for present-day technology. The one-dimensional problem, though can be solved relatively easily, has very limited applications. There are also problems associated with the data that is required by the general solutions. From the results obtained in §2.2 and §2.4 (see in particular the discussions at the end of §2.2, and the formula (2.52)), it is clear that the impulse response of the medium system is necessary for either the exact or the approximate solutions, while knowing the impulse response is equivalent to knowing the scattering or the reflecting coefficient for harmonic waves of all frequencies, ranging from zero to infinity. In practice transducers are efficient only within a certain limited frequency band, so that the impulse response is usually unavailable. Another thing that we should not forget about is the directivity of the transducer, which is very angular-dependent and often uncontrollable. Even in the simple case of plane wave incidence upon a layered medium with non-parallel plane interfaces (Fig. 3.1), the waves reflected from different depths will arrive at the receiving transducer from different directions. The directivity of the transducer gives them different gains when transforming the mechanical vibrations into electrical signals. To compensate for this difference in gain is impossible unless the directivity and the wave directions are known simultaneously. (Using two transducers as receivers may enable us to determine the direction of plane waves (Fig. 3.2)). However, this is rarely the case and generally we cannot expect the amplitude information contained in the received signal to be quantitatively correct.

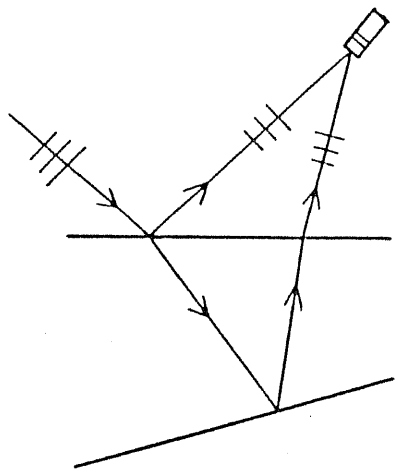

Fig. 3.1 Waves are arriving from different directions.

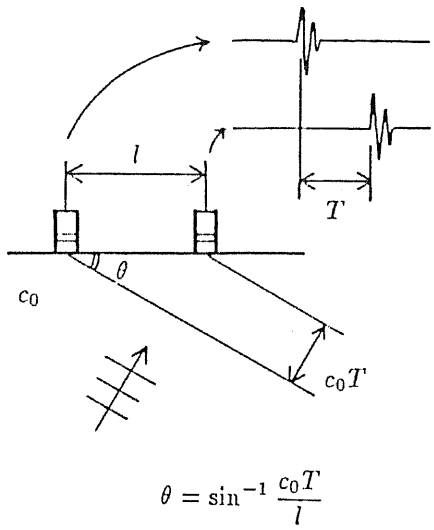

Fig. 3.2 Wave direction can be determined using 2 transducers.

In summary of the above discussion, practical measurement of the scattered waves is limited to a certain frequency band, and the measured signals have amplitudes that are difficult to be related to the real amplitudes of sound waves. Based upon these considerations we investigated the possibility of calculating the sound velocity profile without using the amplitude information, and concluded that it is possible.

3.1 Sound Velocity Inversion Using Travel Time Relationships

Consider probing a one-dimensional medium with plane waves at different incident angles. The time it takes for the wave to reach a certain depth x is different since the incident angles θ_{a0} and θ_{b0}, and thus the propagation paths, are different. However, by comparing the reflection data it is noticed that waves coming from the same part of the medium resemble each other, except that they arrive at different time instants. This suggests that these waveforms can be made nearly the same (according to certain criteria) by stretching or

contracting the time axis of one of them. In this way, a correspondence can be built up between the two travel times. That is, it is possible to relate one travel time $t_a(x)$ to another, $t_b(x)$, even though both are unkown functions of x. In this section we will show that it is possible to calculate the sound velocity as a function of depth from the travel time relationship $t_a(t_b)$.

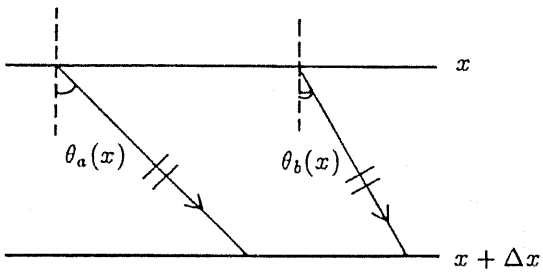

Fig. 3.3 A thin layer of a one-dimensional medium.

Consider a thin layer from x to $x+dx$ (Fig. 3.3). For non-perpendicular plane waves the equivalent sound velocity is $c(x)/\cos\theta(x)$ (see Appendix A), so that

$$dt_a(x) = \frac{dx}{c(x)/\cos\theta_a(x)}, \quad dt_b(x) = \frac{dx}{c(x)/\cos\theta_b(x)}. \tag{3.1}$$

and

$$\frac{dt_a(x)}{dt_b(x)} = \frac{\cos\theta_a(x)}{\cos\theta_b(x)} \tag{3.2}$$

On the other hand, from the Snell's law for the refraction of plane waves we have

$$\begin{aligned} \frac{\sin\theta_a(x)}{c(x)} &= \frac{\sin\theta_{a0}}{c(0)} \equiv p_a \\ \frac{\sin\theta_b(x)}{c(x)} &= \frac{\sin\theta_{b0}}{c(0)} \equiv p_b \end{aligned} \tag{3.3}$$

Combining (3.2) with (3.3) we get

$$\left(\frac{dt_a}{dt_b}\right)^2 = \frac{1-\sin^2\theta_a(x)}{1-\sin^2\theta_b(x)} = \frac{1-p_a^2c^2(x)}{1-p_a^2c^2(x)} \tag{3.4}$$

from which the sound velocity $c(x)$ can be solved:

$$c(x) = \sqrt{\frac{1-(dt_a/dt_b)^2}{p_a^2 - p_b^2(dt_a/dt_b)^2}} \tag{3.5}$$

This equation indicates that, if t_a is obtained as a function of t_b, then c can also be obtained as a function of t_b. The calculation of the density ρ as a function of t_b is possible if the equivalent impedance is available (see (2.52)):

$$\rho(t_b) = \frac{z_b(t_b)\cos\theta_b(t_b)}{c(t_b)} = \frac{z_b(t_b)\sqrt{1-p_b^2c^2(t_b)}}{c(t_b)} \tag{3.6}$$

The final problem is to connect t_b with x, which can be accomplished via

$$x(t_b) = \int_0^{t_b} \frac{c(t_b)}{\cos\theta(t_b)}dt_b = \int_0^{t_b} \frac{c(t_b)}{\sqrt{1-p_b^2c^2(t_b)}}dt_b \tag{3.7}$$

(Here we have used the same notation t_b for the variable and the bound of integration, to help understanding. Of course the integration variable can have any other names. They are not the same thing: one is varying while the other is fixed during the integration.)

The problem how $t_a(t_b)$ may be obtained from the measured signals $r_a(t_a)$ and $r_b(t_b)$ is unsolved yet. A possible answer is to employ an approach similar to the DP-matching (dynamic programing) [55] technique used in speech recognition. Suppose that $r_a(t_a)$ is worked on so that it approaches $r_b(t_b)$ (Fig. 3.4). We can employ the correlation coefficient as a measure of similarity of the two waveforms, so that the influence of amplitude variations can be suppressed. First $r_a(t_a)$ is stretched or contracted in the whole, and the correlation coefficient is calculated for the whole signal, and is maximized. Next we hold onto the middle point and the end point of $r_a(t_a)$ (one at a time), and again shift them about their present positions in both directions, and maximize the correlation coefficient of the influenced parts. Next we hold onto the 1/4 point, 2/4 point, 3/4 point and 4/4 point (the end point), one at a time, and repeat the same process. The amount of shifting for the parts between a fixed point and a shifted point can be calculated using linear interpolation, but it is perhaps better to use other interpolation schemes, such as the spline interpolation, if we are dealing with a continuous instead of a stepwise variation of the sound velocity. At least this approach is feasible in principle, though the calculation of the correlation coefficient between two waveforms can be conceived to be time-consuming. We will not pursue this matter further.

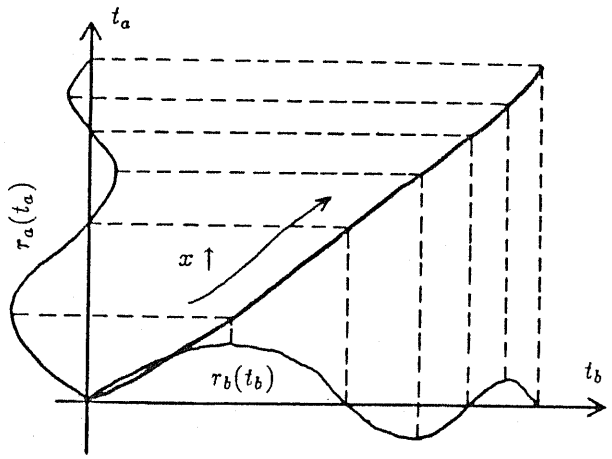

Fig. 3.4 Matching two signals.

Another possibility of obtaining $t_a(t_b)$, if the equivalent acoustic impedances (see Appendix A) $z_a(t_a)$ and $z_b(t_b)$ are known, is to use the ratio $z_a[t_a(x)]/z_b[t_b(x)]$. As a matter of fact,

$$z_a[t_a(x)] = \rho(x)\frac{c(x)}{\cos\theta_a(x)}, \quad z_b[t_b(x)] = \rho(x)\frac{c(x)}{\cos\theta_b(x)} \tag{3.8}$$

so that

$$\frac{z_a[t_a(x)]}{z_b[t_b(x)]} = \frac{\cos\theta_b(x)}{\cos\theta_a(x)} \tag{3.9}$$

By comparing this with (3.2) we obtain that

$$\frac{dt_a(x)}{dt_b(x)} = \frac{z_b[t_b(x)]}{z_a[t_a(x)]} \tag{3.10}$$

If t_a is viewed as a function of t_b, the above equation is indeed an ordinary first-order differential equation:

$$\frac{dt_a}{dt_b} = \frac{z_b(t_b)}{z_a(t_a)} \tag{3.11}$$

having the form $dy/dx = f(x,y)$ where $f(x,y)$ is a computable function of x and y. This equation can be solved numerically using for example the Runge-Kutta's method. The initial condition is clearly $t_a(t_b)|_{t_b=0} = 0$.

3.2 Why Layered Media, and What Kind of Layered Media?

Now let us turn to layered media. There are three reasons that suggest the consideration of layered media:

1. Layered structures are encountered in the inhomogeneous bodywall, which is the bigges factor that deteriorates the image quality. The skin, the eye ball are also examples of layered media.

2. The necessary information for solving the inverse problem can be greatly reduced by exploiting the structural simplicity of the non-uniformity of a layered medium. Consequently the measurement and processing requirement is far less than for general media.

3. The reflection from a layered medium consists of a series of isolated pulses, and the travel time relationship required in the previous section can be easily obtained from the positions of these pulses.

Having answered the question of "Why layered media", next we will discuss about "What kind of layered media?" There can be 3 categories of complexity, as illustrated in Fig. 3.5.

The first category has parallel, horizontal interfaces, as shown in the figure. The second category has non-parallel plane interfaces, while the third has curved interfaces. Here we will only treat problems of the first and the second category.

Consider the description of one interface. In the first category only one parameter, *i.e.*, the distance d_k between two interfaces is needed. In the second category two parameters are needed: the distance d_k and the angle of inclination γ_k. For the third category there are many more variations. If each interface is a parabolic curve, 3 parameters are needed. More generally one can assign N points on the interface and use the spline function to interpolate the curve. In the case N is just the number of parameters for the description

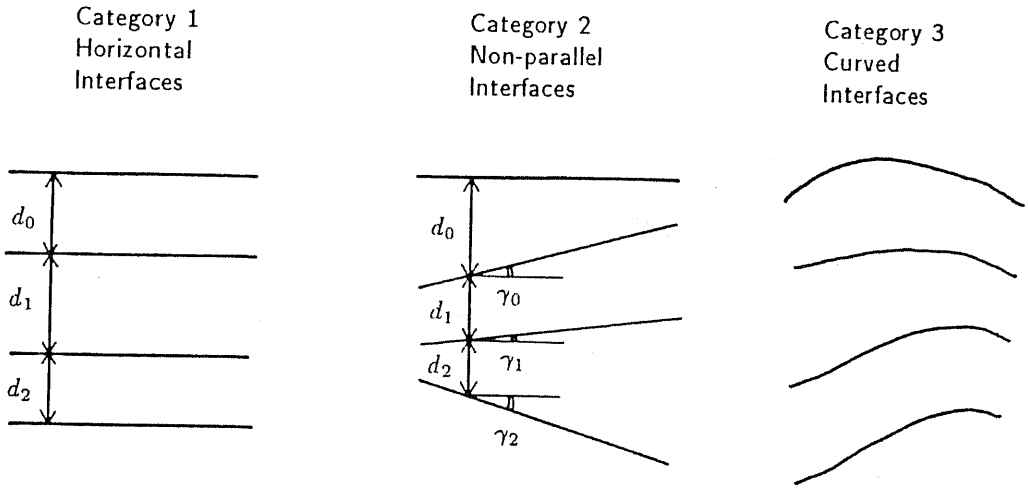

Fig. 3.5 Three categories of complexity of layered media.

of one curve. A special case of curved interfaces is worth noting, that is, the case of concentric circle interfaces (Fig. 3.6). Such interfaces can be described using the radius (one parameter) only. A particularly simple relationship [56] for the ray path can be derived, making it possible to transfer such media into media of the first category.

Referring to Fig. 3.6, from the Snell's law of refraction, we obtain

$$\frac{c_i}{\sin\theta_i} = \frac{c_{i+1}}{\sin\theta'_{i+1}} \tag{3.12}$$

On the other hand, from the triangle OAB it is clear that

$$\frac{r_{i+1}}{\sin\theta'_{i+1}} = \frac{r_i}{\sin\theta_{i+1}} \tag{3.13}$$

Thus

$$\frac{c_i}{\sin\theta_i} = \frac{c_{i+1}}{\frac{r_{i+1}}{r_i}\sin\theta_{i+1}} \quad \Rightarrow \quad \frac{c_i}{r_i\sin\theta_i} = \frac{c_{i+1}}{r_{i+1}\sin\theta_{i+1}} \tag{3.14}$$

This result indicates that the quantity $c(r)/r\sin\theta(r)$ is a constant along a ray path, as compared with the $c(x)/\sin\theta(x)$ of media with horizontal plane interfaces.

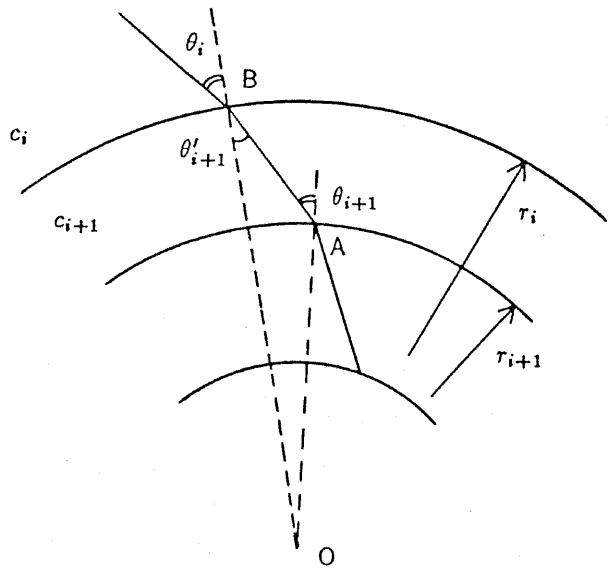

Fig. 3.6 A layered medium with concentric circular interfaces.

3.3 Calculating Travel Times Using Geometrical Paths

Consider a pulse incident upon a layered medium. The acoustic parameters c_k(sound velocity) and ρ_k(density) within each layer are assumed to be constants, so that reflections only occur at the interfaces, and the echo consists of a series of isolated pulses. As discussed at the beginning of this chapter, the amplitude of each observed pulse is not very quantitative. The shape of thses pulses is in principle the same as the incident pulse, and so contains no information about the medium. (However, if there is frequency-dependent attenuation inside each layer, it can be estimated by comparing the frequency component of two adjacent pulses.) Thus the only information about the layered medium is contained in the positions of the pulses. These positions indicate how long it takes for the acoustic wave to reach a certain interface and to reflect back to the receiver.

The reason that we assume spherical wave incidence is because that the transducers are usually much smaller in size than the medium, so that spherical waves are reasonable approximations to the reality. The exact analysis

of a spherical wave interacting with a plane boundary is rather complicated: first it is decomposed into plane waves of different directions and amplitudes, using the Fourier integral, then the reflection of each plane wave is calculated and finally the result is summed to give the total field of reflection (see Appendix B, [18,41]). This procedure is necessary because the reflection coefficient for plane waves depends upon the incident angle (see Appendix A). However, if the frequency of the spherical wave is high enough and the transducers are not too close to the plane boundary [41], then using the stationary phase approximation [57,58], the reflected wave can be calculated in a much simpler way. The result indicates that the reflected wave is also spherical, and the reflection coefficient is the same as that for a plane wave which propagates along the main path, *i.e.*, the path of geometrical acoustics (Fig. 3.7). This fact implies that the delay for the received spherical wave equals to the propagation time along the geometrical path.

So our problem is transferred into the problem of finding the geometrical path for reflection at a specific interface, which passes through the transmitter and the receiver, and obeys the laws of refraction and reflection. We will treat media with non-parallel plane interfaces (Fig. 3.7). First we calculate the distance between the transmitter and the receiver for an arbitrary incident angle, and then we adjust the incident angle so that the ray passes through a specified receiver position.

Referring to Fig. 3.8(a), the downward propagation through the $(i+1)$th layer results in an increment Δl_i in the horizontal direction:

$$\Delta l_i = \frac{d_{i+1} + l_i(\tan\gamma_i - \tan\gamma_{i+1})}{\cot\theta_{i+1} + \tan\gamma_{i+1}} \tag{3.15}$$

so

$$l_{i+1} = l_i + \Delta l_i = \frac{d_{i+1} + l_i(\tan\gamma_i + \cot\theta_{i+1})}{\cot\theta_{i+1} + \tan\gamma_{i+1}} \tag{3.16}$$

The calculation of l_0 is somewhat special (Fig. 3.9(a))

$$l_0 = \frac{d_0}{\cot\theta_0 + \tan\gamma_0} \tag{3.17}$$

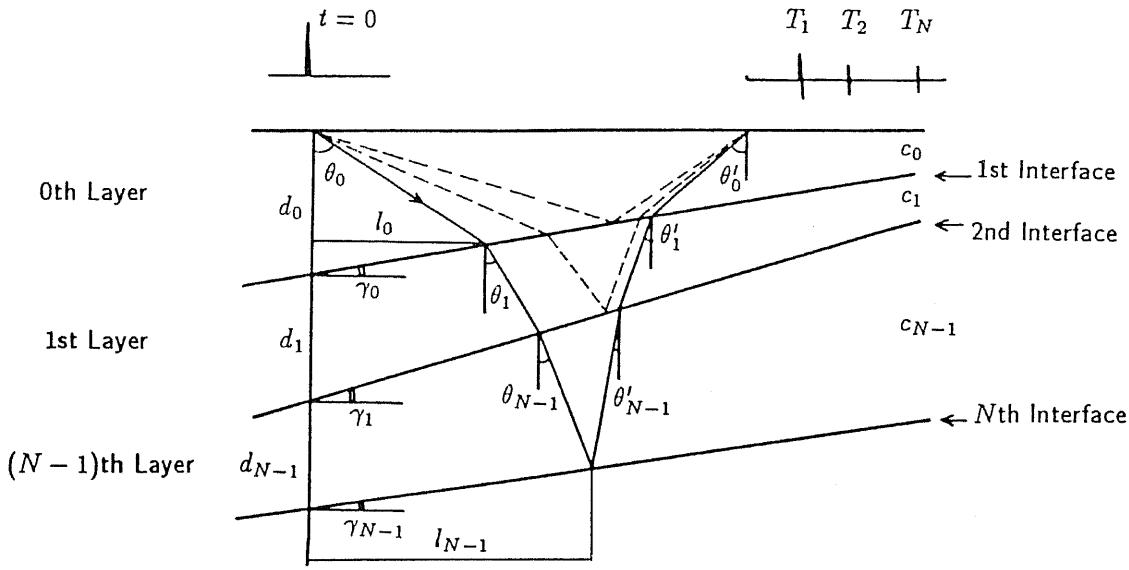

Fig. 3.7 A ray-path in a layered medium.

The refraction of the ray path at the $(i+1)$th interface is governed by

$$\frac{\sin(\theta_{i+1}-\gamma_i)}{c_{i+1}} = \frac{\sin(\theta_i-\gamma_i)}{c_i} \Rightarrow$$

$$\theta_{i+1} = \gamma_i + \sin^{-1}\left(\frac{c_{i+1}}{c_i}\sin(\theta_i-\gamma_i)\right) \tag{3.18}$$

The downward propagation continues down to the Nth interface, at which it is reflected. The law of reflection requires that (Fig. 3.8(b))

$$\theta'_{N-1}+\gamma_{N-1} = \theta_{N-1}-\gamma_{N-1} \;\Rightarrow\; \theta'_{N-1} = \theta_{N-1}-2\gamma_{N-1} \tag{3.19}$$

It should be noted that the positive direction of θ'_{N-1} is opposite to that of θ_{N-1}. During the process of upward propagation we have (Fig. 3.8(c))

$$\Delta l_{i+1} = \frac{d_{i+1}+l_{i+1}(\tan\gamma_i-\tan\gamma_{i+1})}{\cot\theta'_{i+1}-\tan\gamma_i} \tag{3.20}$$

$$l_i = l_{i+1}+\Delta l_{i+1} = \frac{d_{i+1}+l_{i+1}(\cot\theta'_{i+1}-\tan\gamma_{i+1})}{\cot\theta'_{i+1}-\tan\gamma_i} \tag{3.21}$$

$$\theta'_i = -\gamma_i + \sin^{-1}\left(\frac{c_i}{c_{i+1}}\sin(\theta'_{i+1}+\gamma_i)\right) \tag{3.22}$$

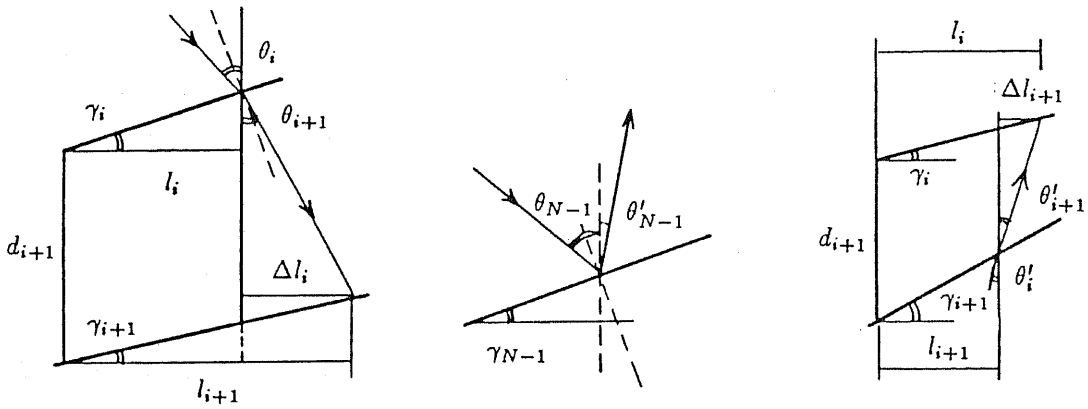

(a) Downward (b) Reflection (c) Upward

Fig. 3.8 Downward propagation, reflection, and upward propagation.

These formulae are applied until l_0 is obtained, to which the following Δl_0 should be added

$$\Delta l_0 = (d_0 - l_0 \tan\gamma_0) * \tan\theta'_0 \tag{3.23}$$

to get the final answer (Fig. 3.9(b)).

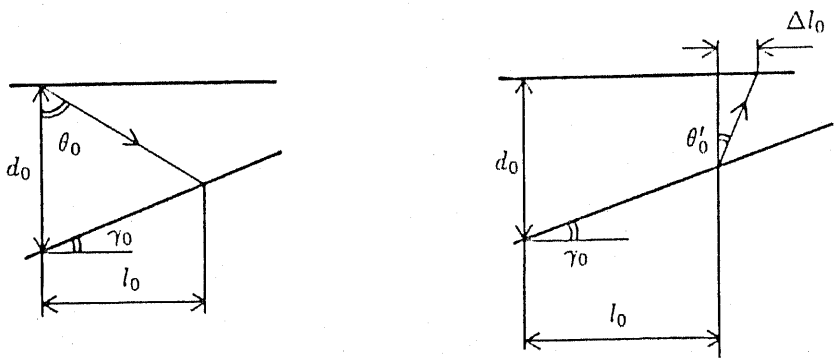

(a) (b)

Fig. 3.9 The initial and the final part of the calculation.

In this way we can calculate the amount of horizontal offset l for an

arbitrary incident angle θ_0. In practice we often need to adjust the incident angle so that the horizontal offset equals to a given value. By investigating the relationship between l and θ_0 for typical settings, it is found that l varies monotonically with θ_0 and the function is close to a straight line (Fig. 3.10). This property makes it an easy job to find the appropriate θ_0 for a prescribed l. Here we adopted the secant method ([59], Fig. 3.11). Specifically, if for some $\theta_{0,k-1}$ and $\theta_{0,k}$, the corresponding l_{k-1} and l_k are obtained, a straight line is drawn through these two points:

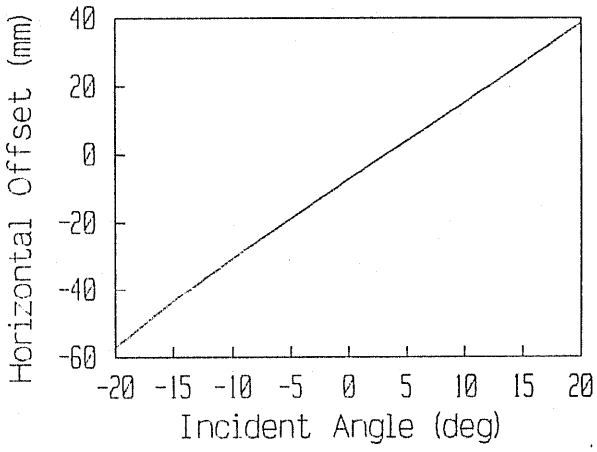

Fig. 3.10 An example of the variation of the horizontal offset l as a function of the incident angle θ_0.

$$\frac{l - l_k}{l_{k-1} - l_k} = \frac{\theta_0 - \theta_{0k}}{\theta_{0,k-1} - \theta_{0k}} \tag{3.24}$$

and the new angle $\theta_{0,k+1}$ is given by

$$\theta_{0,k+1} = \theta_{0k} + \frac{l - l_k}{l_{k-1} - l_k}(\theta_{0,k-1} - \theta_{0k}) \tag{3.25}$$

The corresponding l_{k+1} is calculated again, and the process is iterated until l_k is close enough to the prescribed l. In this way we can make the reflection from a specific interface to emerge at a specific position, and we repeat this calculation for each interface to get the paths for all the reflections.

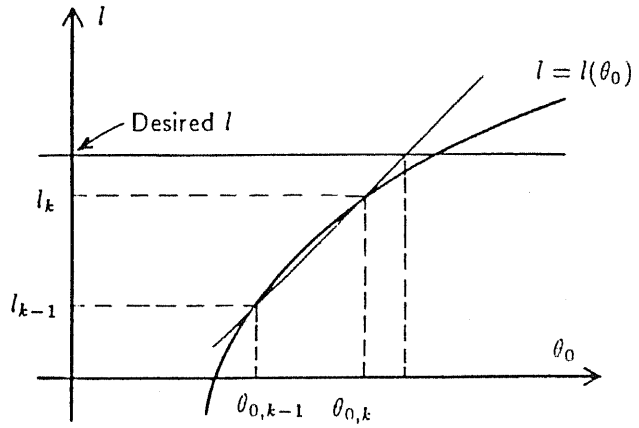

Fig. 3.11 The secant method.

The calculation of travel time is straightforward once the ray path is totally known, so will not be discussed here.

3.4 Layered Media with Horizontal Interfaces

Suppose that under two measurement conditions, the observed signals consist of pulses whose positions are $T_{a1}, T_{a2}, \cdots$, and $T_{b1}, T_{b2}, \cdots$, respectively (Fig. 3.12).

For such media, since the plot of $t_a(x)$ versus $t_b(x)$ is piecewise-linear (Fig. 3.13), dt_a/dt_b can be easily obtained from pulse positions:

$$\left.\frac{dt_a}{dt_b}\right|_{\text{ith layer}} = \frac{\Delta T_{ai}}{\Delta T_{bi}} = \frac{T_{a,i+1} - T_{ai}}{T_{b,i+1} - T_{bi}}, \quad (i = 0, 1, 2, \cdots) \tag{3.26}$$

When the probing wave is planar, the calculation of $c(x)$ is straightforward using (3.5), (3.7). This calculation was made possible through (3.2), which states that

$$\frac{dt_a(x)}{dt_b(x)} = \frac{\cos\theta_a(x)}{\cos\theta_b(x)} \tag{3.2}$$

Now, when the transducers are point-like, and the probing wave is not planar but spherical, this relationship needs to be modified. Under a specific setting

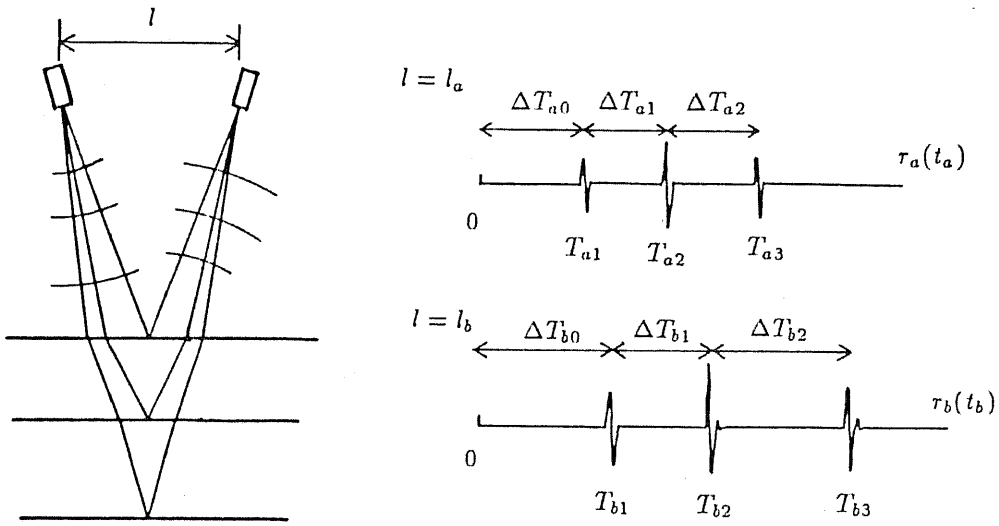

Fig. 3.12 A layered medium with horizontal interfaces, probed by spherical waves.

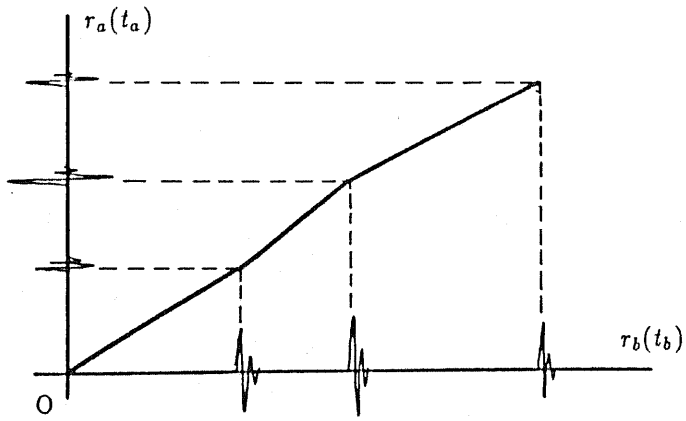

Fig. 3.13 The plot of $t_a(x)$ versus $t_b(x)$ is piecewise-linear for a layered medium which is uniform inside each layer.

(Fig. 3.14) we may investigate $\ln \Delta T$ and $\ln \cos\theta$ for any layer as functions of l, and we always find that the following approximations hold good for a wide range of l:

$$\begin{cases} \ln \Delta T_i \approx a_i l^2 + b_i \\ \ln \cos\theta_i \approx c_i l^2 + d_i \end{cases} \tag{3.27}$$

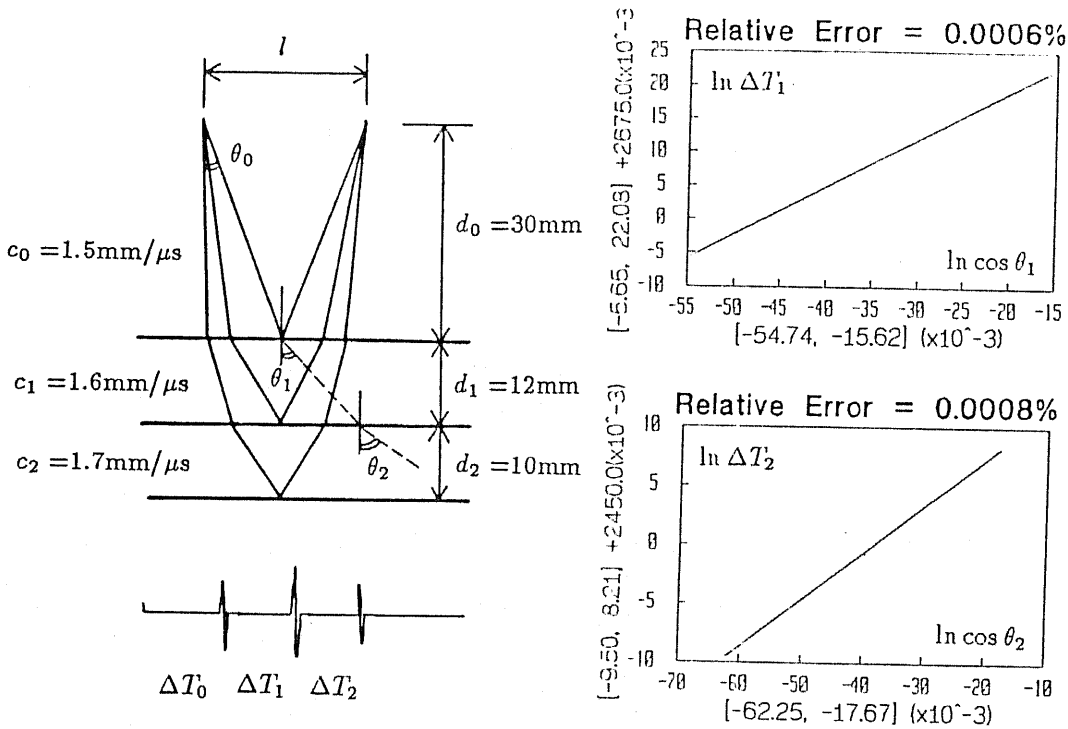

Fig. 3.14 A typicall setting and the approximately linear relationship between $\ln \Delta T$ and $\ln \cos\theta$

Upon eliminating l^2 from these two equations we get

$$\ln \Delta T_i \approx \alpha_i \ln \cos\theta_i + \beta_i \tag{3.28}$$

which means that, when l varies, the relation between $\ln \Delta T$ and $\ln \cos\theta$ is approximately linear (Fig. 3.14). This linearity is found to be a very good approximation. For example, by fitting a straight line to $\ln T_2 \sim \ln \cos\theta_2$, the relative error $(\ln T_2 - \ln T_2')/\ln T_2$ has a mean square value less than 0.001%

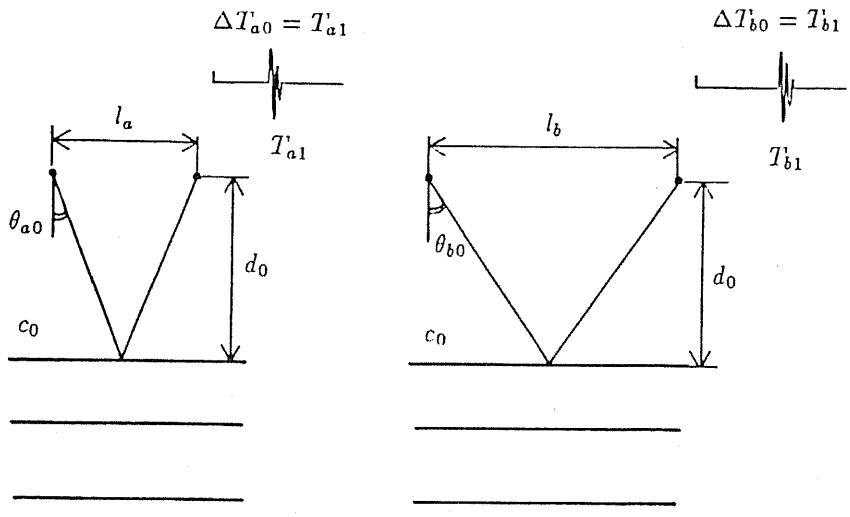

Fig. 3.15 Two settings of measurement using point-like transmitter and receiver.

(l =10~19mm). Note that the θ's in Fig. 3.14 does not correspond to any angles in the real ray-paths. They are choosen merely because that θ_i can be easily determined from c_0, θ_0 and c_i, or rather, c_i can be easily determined from θ_i, as done below. From (3.17) we obtain

$$\frac{\Delta T_{ai}}{\Delta T_{bi}} = \left(\frac{\cos\theta_{ai}}{\cos\theta_{bi}}\right)^{\alpha_i} \tag{3.29}$$

which is a modification to (3.2). Thus

$$\left(\frac{\Delta T_{ai}}{\Delta T_{bi}}\right)^{2/\alpha_i} = \frac{1-\sin^2\theta_{ai}}{1-\sin^2\theta_{bi}} = \frac{1-p_a^2c_i^2}{1-p_a^2c_i^2} \tag{3.30}$$

where $p_a = \sin\theta_{a0}/c_0$, $p_b = \sin\theta_{b0}/c_0$, the same as defined in (3.3), although the meanings of θ_{a0} and θ_{b0} are somewhat different. The parameters c_0, θ_{a0}, θ_{b0} can be obtained from l_a, l_b, ΔT_{a0} and ΔT_{b0} since (Fig. 3.15)

$$\begin{cases} \Delta T_{a0} = l_a/(c_0\sin\theta_{a0}) \\ \Delta T_{b0} = l_b/(c_0\sin\theta_{b0}) \\ l_a\cot\theta_{a0} = l_b\cot\theta_{b0} \end{cases} \tag{3.31}$$

To use (3.20) to calculate c_i one still has to know about α_i. It is found that α_i varies from layer to layer, and depends on the overall configuration in a complicated way. In practice we may solve this problem by iteration. At first we put α_i to 1 (plane wave value) and calculate for c_i by (3.30). With c_i and, say $T_{a,i+1}$ (or $T_{b,i+1}$), we can find the thickness d_i from the simultaneous equations (Fig. 3.16)

$$\begin{cases} \sum_{k=0}^{i} d_k \tan\delta_k = \dfrac{l_a}{2} \\ \dfrac{\sin\delta_{k+1}}{\sin\delta_k} = \dfrac{c_{k+1}}{c_k}, \quad (k = 0, 1, \cdots, i-1) \\ \sum_{k=0}^{i} \dfrac{d_k}{c_k \cos\delta_k} = \dfrac{T_{a,i+1}}{2} \end{cases} \tag{3.32}$$

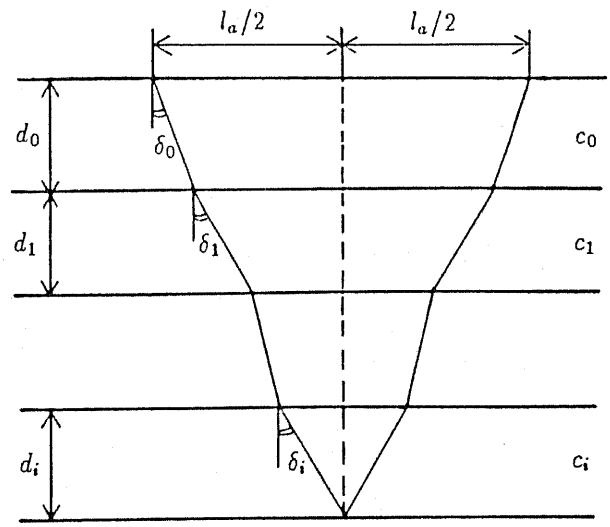

Fig. 3.16 A ray path in a horizontally layered medium.

There are $i+2$ equations in (3.32) and there are $i+2$ unknowns: d_i, δ_0, δ_1, $\cdots$, δ_i. These equations can be solved numerically, so that d_i is obtained. Then the medium is totally known (though temporarily) down to

the ith layer, and the propagation times $\Delta T'_{ai}$ and $\Delta T'_{bi}$ can be calculated for the temporarily reconstructed medium, as well as the angles θ_{ai} and θ_{bi}, corresponding to θ_{a0} and θ_{b0}. Now from (3.29) we can recalculate α_i using

$$\alpha_i = \frac{\ln(\Delta T'_{ai}/\Delta T'_{bi})}{\ln(\cos\theta_{ai}/\cos\theta_{bi})} \tag{3.33}$$

and c_i is again calculated by (3.30). This process is repeated until convergence is reached, which can be examined by comparing either the values of α_i or c_i before and after each interation. The procedure of calculating c_0, d_0, c_1, d_1, $\cdots$, c_i, d_i from T_{a1}, T_{a2}, $\cdots$, $T_{a,i+1}$ and T_{b1}, T_{b2}, $\cdots$, $T_{b,i+1}$ is summarized in the flow-chart in Fig. 3.17.

The basic idea behind this procedure is that, the sound velocity of a new layer is first calculated roughly, then its thickness is calculated from the real propagation times, and these results are applied to improve the calculation of the sound velocity.

3.5 Layered Media with Non-Parallel Interfaces

When it comes to non-parallel interfaces, the calculation is much complicated by the fact that no simple connection between ΔT (the time elapsed between two observed pulses) and $\cos\theta$ (θ is an angle which can be easily determined from the sound velocity) has been found. Although one still observes that $\ln\Delta T$ and $\ln\cos\theta$ are approximately parabolic functions of l (Fig. 3.18), *i.e.*,

$$\begin{cases} \ln\Delta T \approx a(l-b)^2 + c \\ \ln\cos\theta \approx p(l-q)^2 + r \end{cases} \tag{3.34}$$

the problem is that the centers of these curves b and q are unequal, so that at most one can obtain a relationship like the following

$$(A\ln\cos\theta + B\ln\Delta T)^2 + C\ln\cos\theta + D\ln\Delta T = 1 \tag{3.35}$$

which has 4 parameters in it, whereas in (3.28) only 2 parameters are needed.

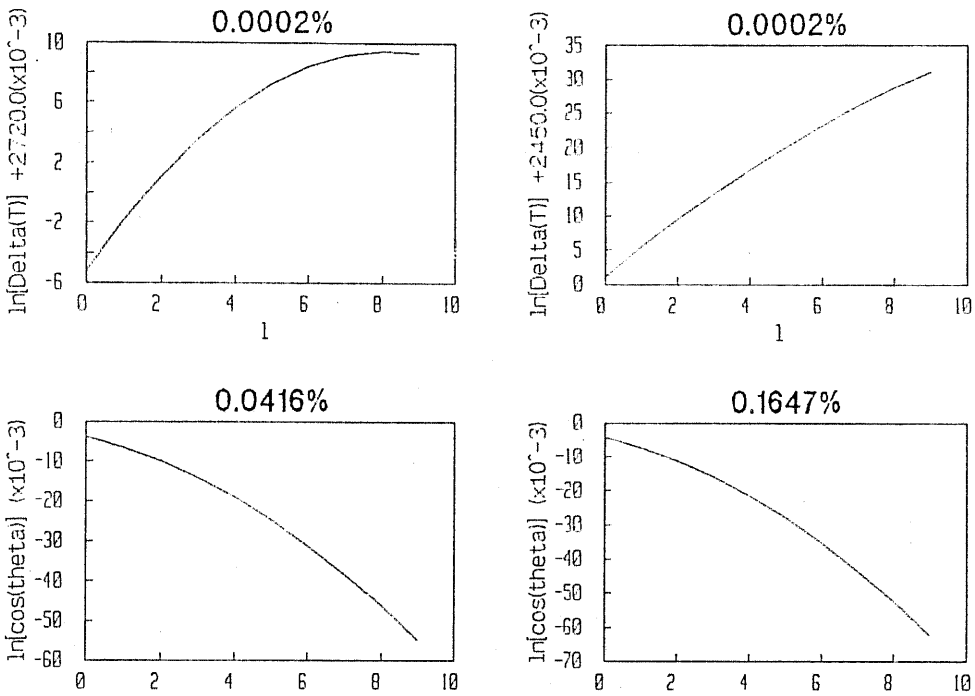

Fig. 3.18 $\ln \Delta T$ and $\ln \cos\theta$ versus l, for a 3-layer model.

We abandoned the search for "efficient" algorithms and considered a more general approach, in which the medium parameters are determined by solving a minimization problem.

First of all we notice that, since the determination of one layer needs three parameters c_i, d_i and γ_i (Fig. 3.19), three signals received at different locations l_a, l_b and l_c are necessary. Denoting the pulse positions by T_{a1}, T_{a2}, $\cdots$, T_{b1}, T_{b2}, $\cdots$, T_{c1}, T_{c2}, $\cdots$, the problem is to calculate from these data c_0, d_0, γ_0, c_1, d_1, γ_1, $\cdots$. Of course the locations l_a, l_b and l_c are also assumed to be known.

The calculation of c_0, d_0 and γ_0 depends upon T_{a1}, T_{b1} and T_{c1} only, and can be carried out accurately. Referring to Fig. 3.20, it can be shown that

$$\begin{aligned}(c_0 T)^2 &= (d_0 \cos\gamma_0 + d_0 \cos\gamma_0 - l \sin\gamma_0)^2 + (l\cos\gamma_0)^2 \\ &= 4d^2\cos^2\gamma_0 + l^2 - 4ld\sin\gamma_0\cos\gamma_0 \\ &= 4d^2\cos^4\gamma_0 + (l - d\sin 2\gamma_0)^2 \end{aligned} \tag{3.36}$$

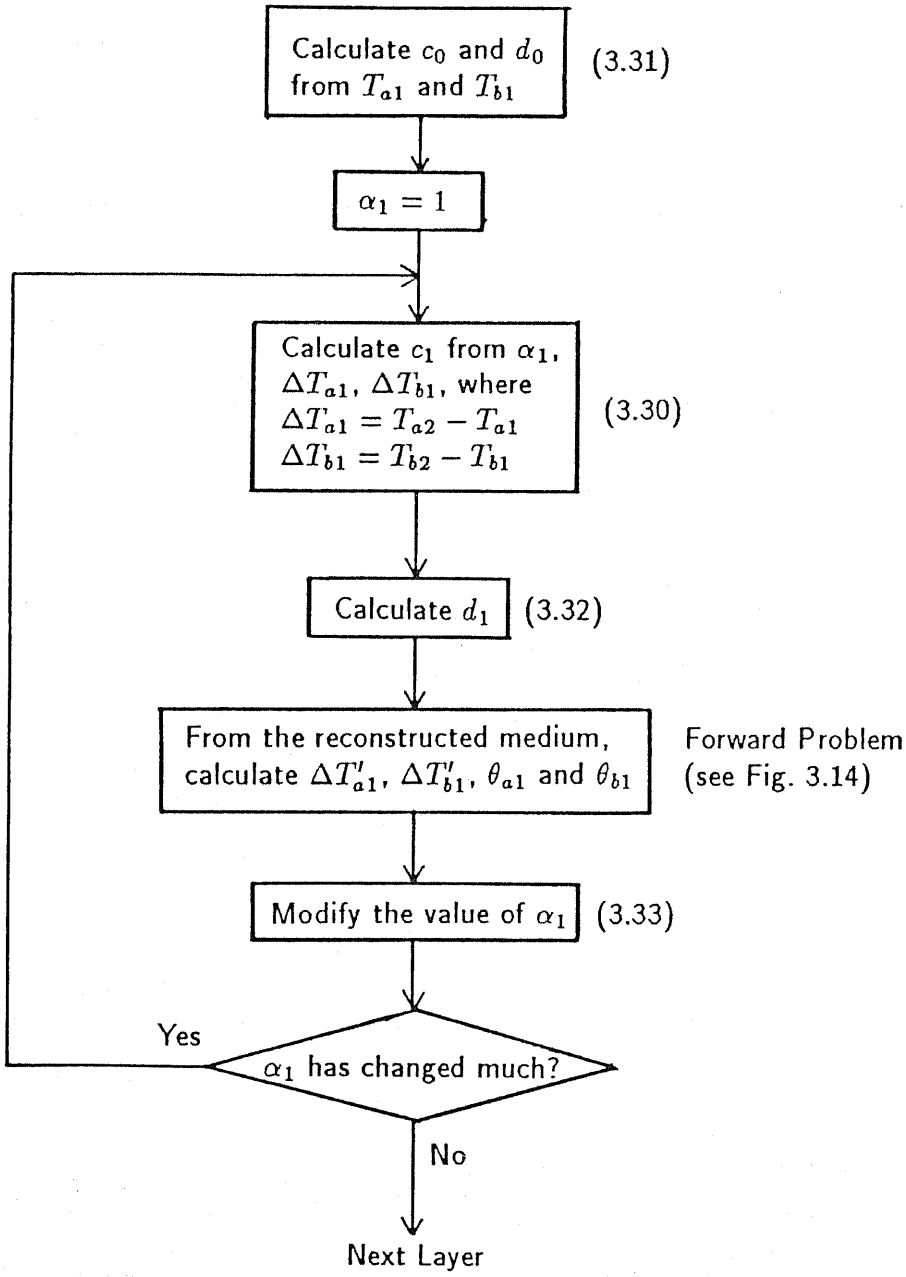

Fig. 3.17 Flowchart of inverting pulse position data for sound velocity and depth of a layered medium with horizontal interfaces, probed by spherical waves.

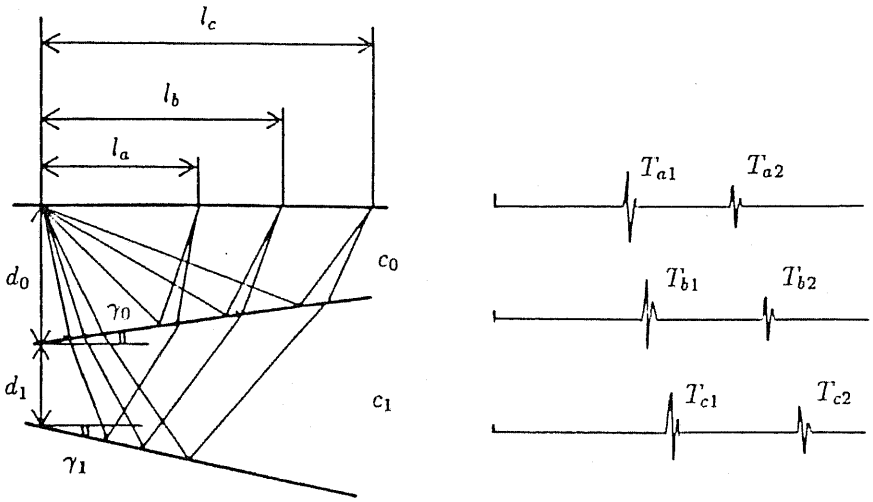

Fig. 3.19 A layered medium with non-parallel plane interfaces, measured under 3 different settings.

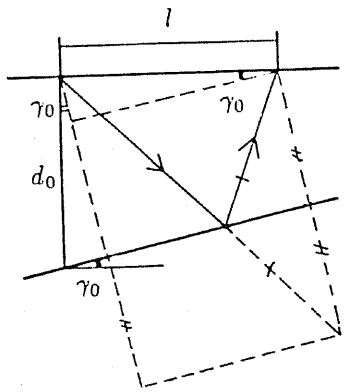

Fig. 3.20 Calculation of the first layer.

It is clear from (3.36) that T^2 is a parabolic function of l, so that if by parabolic fitting to (l_a, T_{a1}^2), (l_b, T_{b1}^2), (l_c, T_{c1}^2), we obtain

$$T^2 = b_0 l^2 + b_1 l + b_2 = b_0 \left(l + \frac{b_1}{2b_0} \right)^2 + b_2 - \frac{b_1^2}{4b_0}$$
$$\equiv p_0 (l + p_1)^2 + p_2 \qquad (3.37)$$

then, comparing (3.37) with (3.36), we arrive at

$$c_0 = \frac{1}{\sqrt{p_0}}, \quad \gamma_0 = -\tan^{-1}\left(\frac{p_1}{c_0\sqrt{p_2}}\right), \quad d_0 = -\frac{p_1}{\sin 2\gamma_0} \tag{3.38}$$

However such simple derivation is no longer available for the subsequent layers, and generally we may assume the medium to be totally known down to the $(k-1)$th layer, and determine the kth layer from $T_{a,k+1}$, $T_{b,k+1}$ and $T_{c,k+1}$. This may be done by minimizing the following

$$\begin{aligned} J_1 = (T'_{a,k+1} - T_{a,k+1})^2 + \\ + (T'_{b,k+1} - T_{b,k+1})^2 + (T'_{c,k+1} - T_{c,k+1})^2 \end{aligned} \tag{3.39}$$

where the dashed quantities are calculated from the model, with assumed values of c_k, d_k and γ_k for the kth layer.

To save computation time we did this in a different way, treating c_k differently from d_k and γ_k. First we assume a value for c_k and determine d_k and γ_k by minimizing

$$J_2 = (T'_{a,k+1} - T_{a,k+1})^2 + (T'_{c,k+1} - T_{c,k+1})^2 \tag{3.40}$$

(J_2 can be made arbitrarily close to 0, just as J_1). Next we calculate $T'_{b,k+1}$, which is generally different from the observed $T_{b,k+1}$, because the value of c_k is incorrect. However, if we view $T'_{b,k+1}$ as a function of c_k under this condition (*i.e.*, d_k and γ_k have been adjusted by minimizing J_2), we find that the curve is again very close to a straight line (Fig. 3.21). Thus the secant method (Fig. 3.9) is suitably applied here to modify c_k so that $T'_{b,k+1}$ approaches $T_{b,k+1}$.

The minimization of (3.40) with respect to d_k and γ_k is not an easy job. In Fig. 3.22 the contour lines of J_2 is shown. It can be seen that the ordinary gradient method leads to a zig-zag searching path in the parameter space, and the convergence is very slow (this phenomenon is known as hemstitching [59]). To resolve this problem we employed the Marquardt-Levenberg algorithm [60],

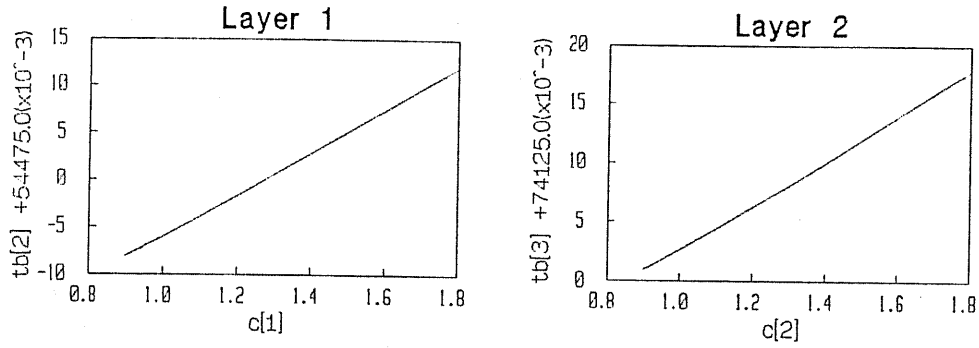

Fig. 3.21 An example of the linear relationship between $T'_{b,k+1}$ and c_k, when d_k and γ_k have been adjusted to minimize J_2.

which is a combination of the gradient method and the Gauss-Newton method [61,62]. It provides a search direction which is in between the vectors provided by these two methods. Since the gradient method looks at local properties only, it is unsuitable when the searching region is still far from the optimum. On the other hand the Gauss-Newton method approximates the square-of-error evaluation function by quadratic forms, and aims at the optimal point in one step. This makes it diverges easily when the searching is near the optimum. By adjusting a parameter in the Marquardt-Levenberg algorithm, one can combine the merits of these two methods, shifting from the Gauss-Newton method to the gradient method as the searching goes on. We will not go into the details of this algorithm, but only mention that it has been working well for our purpose.

The selection of the initial valuse for c_k, d_k and γ_k can be made rather arbitrarily. We have tried the following two methods, and both leaded to convergence in processing simulated as well as experimental data. In the first method, we calculate c_k, d_k and γ_k from T_{ak}, T_{bk} and T_{ck} using (3.37) and (3.38), as if it were the 0th layer. Then we recalculate d_k by

$$d_k = \frac{1}{4} c_k (T_{a,k+1} - T_{ak} + T_{c,k+1} - T_{ck}) \tag{3.41}$$

It is found that γ_k obtained in this way is close to the final answer, but c_k is a kind of average of the sound velocities of the $0 \sim (k-1)$th layer, and d_k is proportional to c_k.

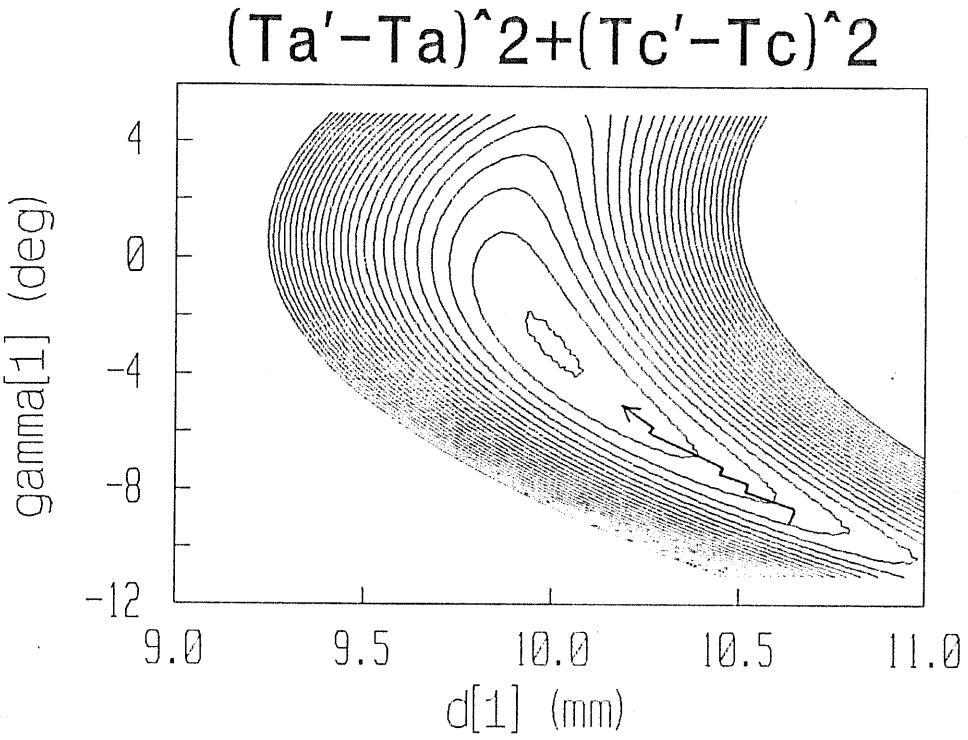

Fig. 3.22 Hemstitching of the gradient method in the searching space of d_k and γ_k.

Another method is even simpler. We just guess about the average sound velocity $\bar{c}$ (which is not difficult in most cases) and use

$$\begin{cases} c_k = \bar{c} \\ d_k = \dfrac{1}{4} c_k (T_{a,k+1} - T_{ak} + T_{c,k+1} - T_{ck}) \\ \gamma_k = 0 \end{cases} \tag{3.42}$$

as the initial values.

4

Estimation of Pulse Positions

4.1 Modelling the Reflection from a Layered Medium

We assume that the reflection occurs only at the interfaces among the layers, and the impulse response of the layered medium consists of a series of impulses. That is,

$$h(t) = r_1\delta(t - t_1) + r_2\delta(t - t_2) + \cdots + r_n\delta(t - t_n) \tag{4.1}$$

is the impulse response.

In practice $h(t)$ is not directly measurable, owing to the finite band-width of the measuring system. Denoting the impulse response of the measuring system by $g(t)$, the reflected signal is the convolution of $g(t)$ with $h(t)$, and there is always the unavoidable measurement noise $m(t)$, which we assume to be additive. Thus a simple model of the received signal $s(t)$ is obtained:

$$s(t) = \int_{-\infty}^{+\infty} g(\tau)h(t - \tau)d\tau + m(t) = g(t) * h(t) + m(t) \tag{4.2}$$

where $*$ denotes convolution. The graphical counterpart of (4.2) is illustrated in Fig. 4.1.

The characteristics of the measuring system $g(t)$ is mainly determined by the transducers, although the driving and amplifying circuits also play a role in it. Usually the spectrum of $g(t)$ has its energy centered around a certain frequency range (say 2 to 4MHz), acting as a bandpass filter upon $h(t)$. On

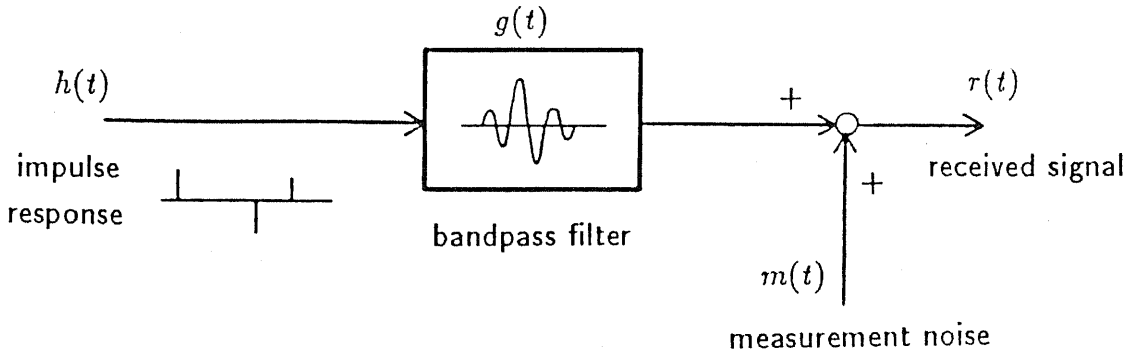

Fig. 4.1 Modelling the signals reflected from a layered medium.

the other hand the signal $h(t)$ is wide-banded. In fact the Fourier transform of $h(t)$ is

$$H(i\omega) = \int_{-\infty}^{+\infty} h(t)e^{-i\omega t}dt = \sum_{k=1}^{n} r_k e^{-i\omega t_k}$$
$$= \sum_{k=1}^{n} r_k \cos\omega t_k - i\sum_{k=1}^{n} r_k \sin\omega t_k \qquad (4.3)$$

It can be seen that $H(i\omega)$ is a periodic function of ω, with discrete "frequencies" t_1, t_2, $\cdots$, t_n. Our interest is in recovering $h(t)$ from $r(t)$ and $g(t)$. Because of the existence of the measurement noise $m(t)$, and the bandlimitedness of $g(t)$, the information about $H(i\omega)$ is only available in a certain frequency range. To calculated $h(t)$ in the time-domain means to extrapolate $H(i\omega)$ from that range to the whole frequency domain. Generally this would not be possible, but as discussed above, if $h(t)$ consists of sparse spikes, this becomes possible because of the strong periodicity in $H(i\omega)$.

4.2 Deconvolution via Spectral Fitting

Clearly to estimate $h(t)$ from $r(t)$ and $g(t)$ is a deconvolution operation. We have developed a spectral fitting procedure for this purpose.

Suppose that $H(i\omega)$ is known in a certain frequency range (ω_L, ω_H), from which the parameters (t_1, r_1), (t_2, r_2), $\cdots$, (t_n, r_n) are to be estimated. Denoting the estimated parameters by (τ_1, ρ_1), (τ_2, ρ_2), $\cdots$, (τ_n, ρ_n), first we determine (τ_1, ρ_1) by minimizing

$$J(\tau_1, \rho_1) = \sum_{l=1}^{N} \left| H(j\omega_l) - \rho_1 e^{-i\omega_l \tau_1} \right|^2 . \tag{4.4}$$

where we have considered discrete frequencies

$$\omega_l = \omega_L + \frac{l-1}{L-1}(\omega_H - \omega_L), \qquad l = 1, 2, \cdots, L \tag{4.5}$$

This minimization problem can be solved effectively using the FFT. As a matter of fact, for a fixed τ_1, to minimize $J(\tau_1, \rho_1)$ with respect to ρ_1 we calulate $\partial J / \partial \rho_1$ and put it to zero:

$$\begin{aligned} \frac{\partial J}{\partial \rho_1} &= \frac{\partial}{\partial \rho_1} \left[\sum_{l=1}^{L} \left(H(i\omega_l) - \rho_1 e^{-i\omega_l \tau_1} \right) \left(H^*(i\omega_l) - \rho_1 e^{i\omega_l \tau_1} \right) \right] \\ &= \sum_{l=1}^{L} \left(-H(i\omega_l) e^{i\omega_l \tau_1} - H^*(i\omega_l) e^{-i\omega_l \tau_1} \right) + 2L\rho_1 = 0 \end{aligned} \tag{4.6}$$

where $H^*(i\omega_l)$ is the complex conjugate of $H(i\omega_l)$. Thus

$$\begin{aligned} \rho_1 &= \frac{1}{2L} \sum_{l=1}^{L} \left[H(i\omega_l) e^{i\omega_l \tau_1} + H^*(i\omega_l) e^{-i\omega_l \tau_1} \right] \\ &= \frac{1}{L} \mathrm{Re} \left[\sum_{l=1}^{L} H(i\omega_l) e^{i\omega_l \tau_1} \right] \end{aligned} \tag{4.7}$$

The coresponding minimum of J is obtained by substituting (4.7) in (4.4)

$$J(\tau_1, \rho_1) = \sum_{l=1}^{L} |H(i\omega_l)|^2 - N\rho_1^2 \tag{4.8}$$

Now, to minimize $J(\tau_1, \rho_1)$ with respect to τ_1, we can calculate ρ_1 using (4.7) for every τ_1 and choose the one that results in the maximum of ρ_1^2. This is nothing more than calculating the IFFT of $H(i\omega_l)$ (zero-padding the data for frequencies outside of (ω_L, ω_H)) and choosing the one that has the largest

absolute real part. The position of that point gives τ_1, while the real part, after multiplication with N/L where N is the number of FFT points, gives ρ. The factor N/L is needed because in IFFT the calculated quantity is something like $\frac{1}{N}\sum_{k=0}^{N-1} H(k)e^{i2\pi nk/N}$.

Once τ_1 and ρ_1 are obtained, the term $\rho_1 e^{-i\omega_l\tau_1}$ is subtracted from $H(i\omega_l)$, and the same process is repeated, giving successively (τ_2,ρ_2), (τ_3,ρ_3), $\cdots$, *etc.* This process can be terminated by observing the decrease in J, or equivalently, the magnitude of ρ_i.

Clearly we are solving the minimization problem in a sequential manner. One may doubt if the result is the same as minimizing the following J with respect to all the parameters *simultaneously*:

$$J = \sum_{l=1}^{L} \left| H(i\omega_l) - \rho_1 e^{-i\omega_l\tau_1} - \rho_2 e^{-i\omega_l\tau_2} - \cdots - \rho_n e^{-i\omega_l\tau_n} \right|^2 \tag{4.9}$$

The answer is a conditional yes. To see this let us consider the simple case of $n = 2$. The above J becomes

$$\begin{aligned} J &= \sum_{l=1}^{L} \left[H(i\omega_l) - \rho_1 e^{-i\omega\tau_1} - \rho_2 e^{-i\omega_l\tau_2} \right] \left[H^*(i\omega_l) - \rho_1 e^{i\omega\tau_1} - \rho_2 e^{i\omega_l\tau_2} \right] \\ &= \sum |H|^2 - \rho_1 \sum \left(H e^{i\omega_l\tau_1} + H^* e^{-i\omega_l\tau_1} \right) - \rho_2 \sum \left(H e^{i\omega_l\tau_2} + H^* e^{-i\omega_l\tau_2} \right) \\ &+ \rho_1\rho_2 \sum \left(e^{i\omega_l(\tau_1-\tau_2)} + e^{-i\omega_l(\tau_1-\tau_2)} \right) + L\rho_1^2 + L\rho_2^2 \end{aligned} \tag{4.10}$$

If the term

$$\rho_1\rho_2 \sum_{l=1}^{L} \left(e^{i\omega_l(\tau_1-\tau_2)} + e^{-i\omega_l(\tau_1-\tau_2)} \right) = 2\rho_1\rho_2 \mathrm{Re}\left[\sum_{l=1}^{L} e^{i\omega_l(\tau_1-\tau_2)} \right] \tag{4.11}$$

is very small so that it can be neglected in (4.10), the solution of simultaneous minimization is almost the same as that of sequential minimization. By differentiating (4.10) with respect to ρ_1 and ρ_2 while neglecting the term in (4.11), we obtain

$$\rho_1 = \frac{1}{L}\mathrm{Re}\left[\sum H(i\omega_l) e^{i\omega_l\tau_1} \right], \quad \rho_2 = \frac{1}{L}\mathrm{Re}\left[\sum H(i\omega_l) e^{i\omega_l\tau_2} \right] \tag{4.12}$$

and on subtitution in (4.10)

$$J = \sum_{l=1}^{L} |H(i\omega_L)|^2 - L\rho_1^2 - L\rho_2^2 \tag{4.13}$$

Thus we choose τ_1 and τ_2 that correspond to the points of the IFFT of $H(i\omega_l)$, that have the largest and the second largest absolute real part. On the other hand, in sequential minimization, ρ_2 is calculated from

$$\begin{aligned}\rho_2 &= \frac{1}{L}\mathrm{Re}\left[\sum_{l=1}^{L}\left(H(i\omega_l) - \rho_1 e^{-i\omega_l\tau_1}\right)e^{i\omega_l\tau_2}\right] \\ &= \frac{1}{L}\mathrm{Re}\left[\sum_{l=1}^{L} H(i\omega_l)e^{i\omega_l\tau_2}\right] - \frac{1}{L}\rho_1\,\mathrm{Re}\left[\sum_{l=1}^{L} H(i\omega_l)e^{-i\omega_l(\tau_1-\tau_2)}\right]\end{aligned} \tag{4.14}$$

and by assumption the second term is much smaller than the first term, so that (4.14) is almost the same as (4.12).

The assumption that the term in (4.11) be small means that the base functions $e^{-i\omega_l\tau_1}$ and $e^{-i\omega_l\tau_2}$ be orthogonal on $[\omega_L, \omega_H]$. Since these are harmonic functions of ω, if the "frequencies difference" $\tau_1 - \tau_2$ is big enough so that there are many cycles in the range $[\omega_L, \omega_H]$, *i.e.*,

$$|\tau_1 - \tau_2|\ (\omega_H - \omega_L) \gg 1 \tag{4.15}$$

then our assumption becomes true. To get some idea about the condition (4.15), let us see a numerical example: ω_L =2.5MHz×2π, ω_H =4.5MHz×2π, thus (4.15) requires

$$|\tau_1 - \tau_2| \gg \frac{1}{2 \times 2\pi} \approx 0.1\mu s$$

which means that any layer should be much thicker (say 10 times thicker) than 1.5mm/μs×0.1μs/2 = 0.075mm, where 1.5mm/μs is the assumed sound velocity. This condition is usually met in practice.

In conclusion, we have suggested a procedure for estimating the parameters (t_1, τ_1), (t_2, τ_2), $\cdots$, (t_n, τ_n) from $H(i\omega)$ in (ω_L, ω_H). Note that the estimated (τ_1, ρ_1), (τ_2, ρ_2), $\cdots$, (τ_n, ρ_n) do not have one-to-one correspondence with the

t's and r's. In fact $t_1 < t_2 < \cdots < t_n$ while $\rho_1 > \rho_2 > \cdots > \rho_n$, so they are sorted in quite different orders.

An improvement to this procedure is possible. Instead of cutting out a frequency band and performing spectral fitting in that band, one can do weighted fitting, *i.e.*, to minimize

$$J(\tau_1, \rho_1) = \sum_{l=0}^{N} q(\omega_l) \left| H(i\omega_l) - \rho_1 e^{-i\omega_l \tau_1} \right|^2 \tag{4.14}$$

instead of (4.4). Here ω_l is redefined to cover the whole frequency range. For example, if $H(i\omega)$ is obtained by $2N$-point Fourier transform, then

$$\omega_l = \frac{l}{2N} \cdot 2\pi F_{sp}, \quad (l = 0, 1, \cdots, N-1) \tag{4.15}$$

where F_{sp} is the sampling rate. The function $q(\omega_l)$ in (4.14) is the weighting function, which can be chosen to emphasize certain frequency components. The rest of the derivation can be carried out following exactly the same line as done above, so will not be repeated here.

We also notice that it is possible to determine the τ's to a fraction of the sampling interval, by utilizing the fact that zero-padding in the frequency-domain corresponds to over-sampling in the time-domain [63,68]. If zeros are added to the high frequency side of the spectrum $H(i\omega)$ so that the length of the Fourier analysis becomes K times longer, the ratio of over sampling in the time-domain is also K. The case of $K = 2$ is illustrated in Fig. 4.2.

The final question to be answered is how to estiamte $H(i\omega)$ from the signals $s(t)$ and $g(t)$ (see Fig. 4.1). If we take into consideration the existence of measurement noise and perform least-squares estimation, we arrive at the well-known Wiener filter. But to apply the Wiener filter we need knowledge about the cross power spectrum of $h(t)$ and $s(t)$ [64], which is unavailable in our case. On the other hand we may ignore the measurement noise and use the simple solution $\hat{H}(i\omega) = \mathrm{FFT}[s(t)]/\mathrm{FFT}[g(t)]$. In practice we find that this provides satisfactory results when the noise level is not too high. However we agree that this problem, together with the determination of the weighting function $q(\omega)$ in (4.14) is still open for further investigations.

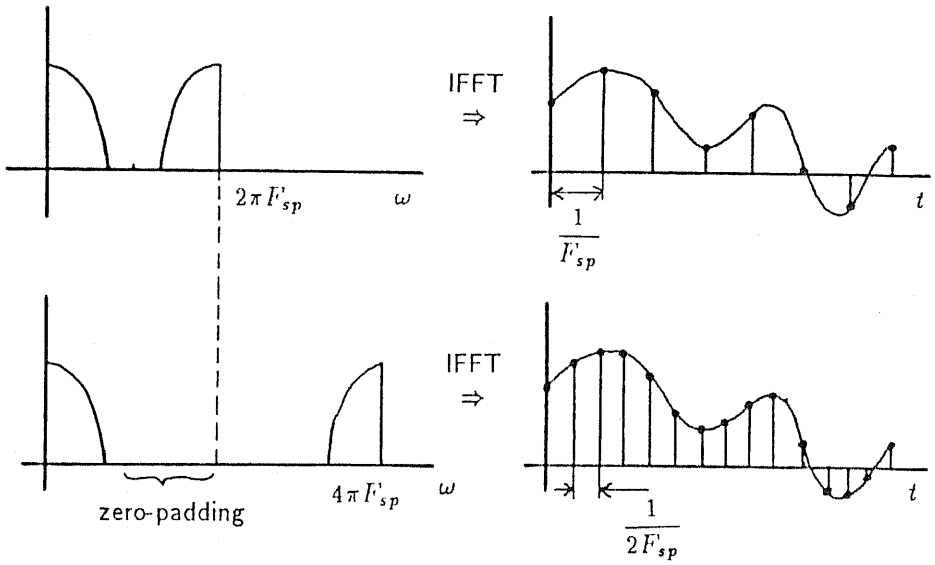

Fig. 4.2 Zero-padding in the frequency-domain corresponds to over-sampling in the time-domain.

4.3 Fluctuation of the Peak Position of Cross-Correlation Function

In this section we will discuss the fluctuation of the position of the estimated pulses, caused by the additive measurement noise. Since this is a time-domain quantity, a time-domain approach is preferable from the stand point of analysis. We notice that it is also possible to estimate the delay between two pulses using the peak position of the cross-correlation function [65,66]. By analysing the fluctuation of the peak position we can get an evaluation of the influence of measurement noise on the problem of delay estimation. By the way, this analysis can also be applied to the delay between two random signals, which is encountered when travel time differences are estimated from randomly scattered signals [67].

Without loss of generality we consider the cross-correlation function between two signals $s_1(t) = g(t) + m_1(t)$ and $s_2(t) = ag(t) + m_2(t)$,

$$R(\tau) = \int_{-\infty}^{+\infty} s_1(t)s_2(t+\tau)dt$$

$$= \int_{-\infty}^{+\infty} [g(t) + m_1(t)]\ [ag(t+\tau) + m_2(t+\tau)]dt$$
$$= a\int g(t)g(t+\tau)dt + \int (gm_2 + agm_1)dt + \int m_1 m_2 dt. \qquad (4.16)$$

The first term equals $a\Gamma(\tau)$ where

$$\Gamma(\tau) \equiv \int_{-\infty}^{+\infty} g(t)g(t+\tau)dt \qquad (4.17)$$

is the auto-correlation function $g(t)$, which has its peak at $\tau = 0$. Noticing that $\Gamma'(0) = 0$, we have in the neighborhood of $\tau = 0$ that

$$\Gamma(\tau) \approx \Gamma(0) + \frac{1}{2!}\Gamma''(0)\tau^2. \qquad (4.18)$$

Further more, from the connection between the correlation function and the power spectrum

$$\Gamma(\tau) = \frac{1}{2\pi}\int_{-\infty}^{+\infty} |G(i\omega)|^2 e^{i\omega\tau} d\omega \qquad (4.19)$$

one can derive

$$\Gamma(0) = \frac{1}{2\pi}\int_{-\infty}^{+\infty} |G(i\omega)|^2 d\omega$$
$$\Gamma''(0) = -\frac{1}{2\pi}\int_{-\infty}^{+\infty} \omega^2 |G(i\omega)|^2 d\omega \qquad (4.20)$$

Here $G(i\omega)$ represents the Fourier transform of $g(t)$.

The second and the third terms of (4.16) are the influences of measurement noise. If the signal-to-noise ratio (SNR) is high enough (which we assume), the third term can be neglected compared to the second term. Denoting

$$n(\tau) \equiv \int [g(t)m_2(t+\tau) + ag(t+\tau)m_1(t)]\, dt, \qquad (4.21)$$

and assuming that $m_1(t)$ and $m_2(t)$ are stationary random processes obeying the same distribution, independent of each other, we have

$$n(\tau) \sim g(\tau) * m_2(\tau) + ag(\tau) * m_1(\tau) = g(\tau) * [m_1(\tau) + am_2(\tau)]$$
$$\sim g(\tau) * \sqrt{1+a^2}\, m(\tau). \qquad (4.22)$$

where $m(\tau)$ is a common notation for $m_1(\tau)$ and $m_2(\tau)$ since they are statistically the same. Concequently we have obtained a model for $R(\tau)$ (Fig. 4.3)

$$R(\tau) \approx a\Gamma(\tau) + n(\tau) \approx a\Gamma(\tau) + \sqrt{1+a^2}\, g(\tau) * m(\tau). \qquad (4.23)$$

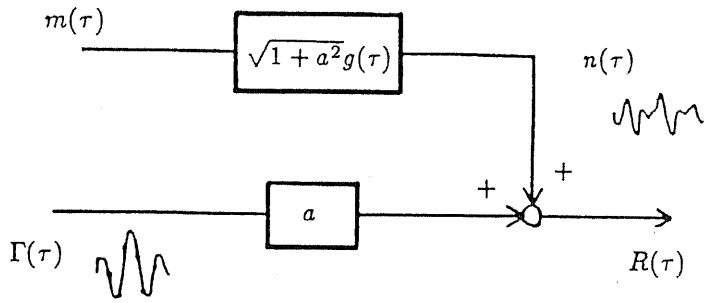

Fig. 4.3 Modelling the cross-correlation function between two pulses which are corrupted by additive noise.

We note that $\Gamma(\tau)$ and $n(\tau)$ have nearly the same frequency content (so, comparable speed of variation), determined by the spectrum of $g(t)$. When the SNR is high, the amplitude of $n(\tau)$ is much smaller than that of $\Gamma(\tau)$, which means that the peak of $R(\tau)$ will only fluctuate slightly about the peak of $\Gamma(\tau)$ which is at $\tau = 0$. To analyse this fluctuation caused by $n(\tau)$, one only has to investigate $dn(\tau)/d\tau$, because in the neighborhood of $\tau = 0$,

$$\begin{aligned} R(\tau) &\approx a\left\{\Gamma(0) + \frac{1}{2}\Gamma''(0)\tau^2\right\} + \{n(0) + n'(0)\tau\} \\ &= \frac{a\Gamma''(0)}{2}\left[\tau + \frac{n'(0)}{a\Gamma''(0)}\right]^2 + a\Gamma(0) + n(0) - \frac{[n'(0)]^2}{2a\Gamma''(0)}. \end{aligned} \tag{4.24}$$

The amount of peak fluctuation is

$$\xi = -\frac{n'(0)}{a\Gamma''(0)} \tag{4.25}$$

which has zero-expectation because

$$\mathrm{E}(\xi) = -\frac{1}{a\Gamma''(0)}\mathrm{E}[n'(0)] = 0 \tag{4.26}$$

So it is bias-less. To estimate its variance $\mathrm{E}[\xi^2]$, we need to evaluated $\mathrm{E}[(n'(0))^2]$. By assuming $m(t)$ to be white so that

$$\mathrm{E}[m(t_1)m(t_2)] = \sigma_m^2 \delta(t_1 - t_2) \tag{4.27}$$

we obtain from (4.22) that

$$\begin{aligned}\mathrm{E}[(n'(0))^2] &= \mathrm{E}\left[(1+a^2)\int_{-\infty}^{+\infty} g'(t_1)m(t_1)dt_1 \int_{-\infty}^{+\infty} g'(t_2)m(t_2)dt_2\right] \\ &= (1+a^2)\sigma_m^2 \int_{-\infty}^{+\infty} [g'(t)]^2 dt \\ &= -(1+a^2)\sigma_m^2 \Gamma''(0).\end{aligned} \tag{4.28}$$

Thus finally

$$\begin{aligned}\mathrm{E}(\xi^2) = \frac{\mathrm{E}[(n'(0))^2]}{a^2[\Gamma''(0)]^2} &= -\frac{1+a^2}{a^2}\frac{\sigma_m^2}{\Gamma''(0)} \\ &= \frac{1+a^2}{a^2}\frac{2\pi\sigma_m^2}{\int_{-\infty}^{+\infty}\omega^2|G(j\omega)|^2 d\omega}\end{aligned} \tag{4.29}$$

In summary, under the condition that $m_1(t)$ and $m_2(t)$ are white and have a small amplitude, the peak position of the cross-correlation function of $r_1(t)$ and $r_2(t)$ as defined in (4.16) fluctuates around the zero point, the amount of which can be estimated by (4.29). The applicability of this result to the spectral fitting method will be investigated using computer simulation, in chapter 5.

From this result it can be seen that, the fluctuation becomes smaller if the noise level is lower, and/or the auto-correlation function of $g(t)$ has a sharper peak at $\tau = 0$ so that the curvature $\Gamma''(0)$ around $\tau = 0$ is greater.

4.4 The Influence of Errorneous Pulse Positions on the Result of Sound Velocity Calculation

For the sake of simplicity we will only consider the case of plane wave incidence on a layered medium with parallel interfaces. From equations (3.5) and (3.26)

$$c_i = \sqrt{\frac{1-(\Delta T_{ai}/\Delta T_{bi})^2}{p_a^2 - p_b^2(\Delta T_{ai}/\Delta T_{bi})^2}} \tag{4.30}$$

where p_a and p_b are defined in (3.3). It is clear that fluctuation of the estimated pulse positions directly influences the calculated sound velocity. To get an idea of this influence, let us examine a numerical example.

Suppose that the sound velocity in the first layer is c_0=1.5mm/μs, and that the two incident angles are $\theta_{a0} = 0°$, $\theta_{b0} = 15°$. From (3.3)

$$p_a = \frac{\sin\theta_{a0}}{c_0} = 0, \quad p_b = \frac{\sin\theta_{b0}}{c_0} = 0.172546$$

Suppose that the real value of c_i is also 1.5mm/μs, and we wish that the calculated value of c_i to be within 1.485~1.515, so that its error does not exceed 1%. This requires $\Delta T_{ai}/\Delta T_{bi}$ to be within 0.96662~0.96523. $\Delta T_{ai}/\Delta T_{bi}$=0.96593 makes c_i just equal 1.5. Thus the requirement on the relative error of $\Delta T_{ai}/\Delta T_{bi}$ is about $\pm$0.07%, which in turn requires the relative error of ΔT_{ai}, ΔT_{bi} to be within $\pm$0.035%. If the layer is 5mm thick, ΔT_{ai}=5mm$\times$2/1.5$\approx$6.67μs. So the error of ΔT_{ai} should be within $\pm$0.00233μs, and each pulse position cannot fluctuate more than $\pm$0.00117μs.

From the above example it is seen that a small error in ΔT_{ai}, ΔT_{bi} of $\pm$0.035% results in a large error in c_i of $\pm$1% under the condition that the two incident angles are 0° and 15°. The amplification of relative error is about 30 times. This is a reflection of the fact that the inverse scattering problem is ill-conditioned [10,72]. A similar calculation reveals that if the two incident angles are 0° and 30°, the amplification is about 8 times.

The above process of error propagation can be seen more clearly if we put $u \equiv \Delta T_{ai}/\Delta T_{bi}$ in (4.30). By differntiation we obtain

$$\frac{dc}{c} = \frac{p_a^2 - p_b^2}{(1-u^2)(p_a^2 - u^2 p_b^2)} u du \tag{4.31}$$

If the two incident angles θ_{a0} and θ_{b0} are not very different, then u is very close to 1, so that (4.31) becomes roughly

$$\frac{dc}{c} \approx \frac{1}{1-u^2} u du = \frac{u^2}{1-u^2}\frac{du}{u} \tag{4.32}$$

Or, if $p_a = 0$,

$$\frac{dc}{c} = \frac{1}{1-u^2}\frac{du}{u} \tag{4.33}$$

All these equations say that the relative error of c is $\frac{u^2}{1-u^2}$ or $\frac{1}{1-u^2}$ times the relative error of u. This amplification of error can be very large if u is close to 1, and to avoid such a situation, one should try to make the difference between the incident angles as big as possible.

5

Computer Simulation

5.1 Deconvolution by Spectral Fitting

This is to show the usefulness of the spectral fitting approach, described in §4.2, in recovering a δ-pulse train from its band-pass filtered and noise-corrupted version.

The received signal is generated according to the model in Fig. 4.1. Signals are sampled at 20MHz, and the length of $s(t)$ is 256 sampling points. $h(t)$ consists of 4 impulses, two of which are made very close to each other—only 10 points apart, to test the ability of this algorithm to distinguish two closely spaced pulses. For $g(t)$ we have used the following pulse:

$$g(t) = e^{-(t-4\sigma_t)^2/2\sigma_t^2} \sin \omega_0(t - 4\sigma_t) \quad (0 \le t \le 8\sigma_t) \tag{5.1}$$

because its logarithmic power spectrum has a parabolic form, similar to those of practical ultrasonic pulses. Outside of the above range $g(t)$ is assumed to be zero. The parameters ω_0 and σ_t have been determined with reference to practical ultrasonic pulses:

$$\omega_0 = 2\pi \times 3.5(\text{rad} \cdot \text{MHz}), \quad \sigma_t = \frac{1}{2\pi\sigma_f} = \frac{1}{2\pi \cdot 0.6}\left(\frac{1}{\text{rad} \cdot \text{MHz}}\right) \tag{5.2}$$

The length of $g(t)$ $(8\sigma_t)$ is about 43 points under the sampling rate of 20MHz. To simulate the received signal the final problem is to determine the amplitude of the measurement noise, so that it simulates a prescribed signal-to-noise ratio

(SNR). This problem tends to be ignored, but is not as simple as it may appear.

Suppose that we are going to simulate a white process

$$\mathrm{E}[m(t)m(t+\tau)] = \sigma_m^2 \delta(\tau) \tag{5.3}$$

under the sampling rate F_{sp}. We cannot directly sample the process $m(t)$ because its energy is distributed in the whole frequency range, far beyond the Nyquist frequency range $[-F_{sp}/2,\ F_{sp}/2]$. $m(t)$ must be first filtered by a low-pass filter, whose frequency response is

$$U(i\omega) = \begin{cases} 1 & -\pi F_{sp} < \omega < \pi F_{sp} \\ 0 & \text{otherwise} \end{cases} \tag{5.4}$$

and the corresponding impulse response is denoted by $u(t)$. The low-pass filtered noise $m'(t)$ is the signal that can be sampled:

$$m'(t) = \int_{-\infty}^{+\infty} m(\tau)u(t-\tau)d\tau \tag{5.5}$$

The auto-correlation function of $m'(t)$ is

$$\begin{aligned} \mathrm{E}[m'(t)m'(t+\tau)] &= \mathrm{E}\left[\int u(\tau_1)m(t-\tau_1)d\tau_1 \cdot \int u(\tau_2)m(t+\tau-\tau_2)d\tau_2\right] \\ &= \int_{-\infty}^{+\infty}\int_{-\infty}^{+\infty} u(\tau_1)u(\tau_2)\sigma_m^2\delta(\tau+\tau_1-\tau_2)d\tau_1 d\tau_2 \\ &= \sigma_m^2 \int_{-\infty}^{+\infty} u(\tau_1)u(\tau+\tau_1)d\tau_1 \end{aligned} \tag{5.6}$$

However, from the fact that the auto-correlation function and the power spectrum are a Fourier transform pair, we have

$$\begin{aligned} \int_{-\infty}^{+\infty} u(\tau_1)u(\tau+\tau_1)d\tau_1 &= \frac{1}{2\pi}\int_{-\infty}^{+\infty} |U(i\omega)|^2 e^{i\omega\tau}d\omega \\ \frac{1}{2\pi}\int_{-\pi F_{sp}}^{\pi F_{sp}} e^{i\omega\tau}d\tau &= F_{sp}\cdot\frac{\sin(\pi F_{sp}\tau)}{\pi F_{sp}\tau} \end{aligned} \tag{5.7}$$

Thus

$$\mathrm{E}[m'(t)m'(t+\tau)] = \sigma_m^2 F_{sp}\cdot\frac{\sin(\pi F_{sp}\tau)}{\pi F_{sp}\tau} \tag{5.8}$$

which is plotted in Fig. 5.1. In particular

$$\mathrm{E}[(m'(t))^2] = \sigma_m^2 F_{sp} \tag{5.9}$$

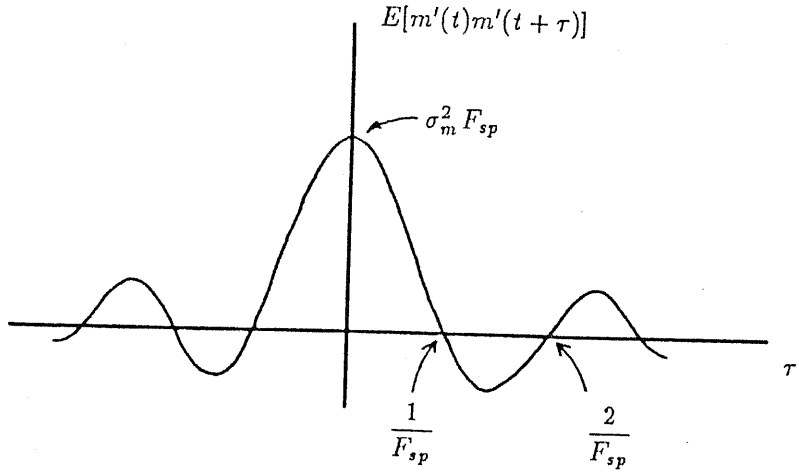

Fig. 5.1 The auto-correlation function of a band-pass filtered white noise.

The result (5.9) is interesting because it says that the variance of the sampled white noise is proportional to the sampling rate, so that it is different for different sampling rates.

Now we can answer the question of how to determine the variance of the numbers which simulate the measurement noise $m(t)$. Defining the SNR around a particular pulse $ag(t)$ by

$$\text{SNR} \equiv \int_{-\infty}^{+\infty} [ag(t)]^2 dt \Big/ \sigma_m^2 \tag{5.10}$$

then from (5.9) the variance of the random numbers is given by

$$\sigma_m^2 F_{sp} = \frac{\int_{-\infty}^{+\infty} [ag(t)]^2 dt}{\text{SNR}} \cdot F_{sp} \tag{5.11}$$

Now we will show the results of our simulation. Waveforms of the signals $g(t)$, $h(t)$ and $s(t)$ are shown in Fig. 5.2. The SNR is set at 20dB around the first pulse in $s(t)$, which is cut out as "$g(t)$" and used as the reference signal of deconvolution. Spectral fitting is performed to FFT[$s(t)$]/FFT["$g(t)$"], in

the range of 2.5~4.5MHz. The decrease of J versus the number of fitted pulses, as well as the finally recovered $\hat{h}(t)$, are also illustrated in Fig. 5.2.

From the results in Fig. 5.2 it can be seen that

1. the two closely spaced impulses have been successfully recovered, even though they cannot be resolved visually from the original $s(t)$;
2. the amplitude of $\hat{h}(t)$ can differ from the original $h(t)$ by a constant multiplication, because of the lack of knowledge of the real $g(t)$ (in fact $\hat{h}(t)$ always contains a unit impulse at the position from where the reference pulse "$g(t)$" has been cut out).

No over-sampling has been performed in this simulation. We will consider it in the next section.

5.2 The Fluctuation of Estimated Pulse Positions

In this section we will apply the analysis made in section 4.3 to a specific pulse signal expressed by (5.1). We assume that the $\pm 4\sigma_t$ range is big enough for $g(t)$ to be recognized as if it were defined from $-\infty$ to $+\infty$. After some calculations we obtain

$$\begin{aligned} |G(j\omega)|^2 &= \frac{\pi\sigma_t^2}{2}\left[e^{-\sigma_t^2(\omega+\omega_0)^2} + e^{-\sigma_t^2(\omega-\omega_0)^2} - 2e^{-\sigma_t^2(\omega^2+\omega_0^2)}\right] \\ \int_{-\infty}^{+\infty} g^2(t)dt &= \frac{1}{2\pi}\int_{-\infty}^{+\infty} |G(j\omega)|^2 d\omega = \frac{\sigma_t\sqrt{\pi}}{2}(1 - e^{-\sigma_t^2\omega_0^2}) \\ \Gamma''(0) &= -\frac{1}{2\pi}\int_{-\infty}^{+\infty} \omega^2 |G(j\omega)|^2 d\omega = -\frac{\sigma_t\sqrt{\pi}}{2}\left[\omega_0^2 + \frac{1}{\sigma_t^2}(1 - e^{-\sigma_t^2\omega_0^2})\right] \end{aligned} \tag{5.12}$$

The parameters ω_0 and σ_t are the same as those of (5.2). Since $\omega_0\sigma_t$=3.5/0.6≈6, the term $e^{-\omega_0^2\sigma_t^2}$ is far less than 1, so it can be neglected in (5.12). From (4.29) and (5.12) we obtain

$$\sigma_\xi = \sqrt{\mathrm{E}(\xi^2)} = \sqrt{-\frac{1+a^2}{a^2}\frac{\sigma_m^2}{\Gamma''(0)}} \approx \sqrt{\frac{-\sigma_m^2(1+a^2)/a^2}{-\frac{\sigma_t\sqrt{\pi}}{2}\left[\omega_0^2 + \frac{1}{2\sigma_t^2}\right]}} \tag{5.13}$$

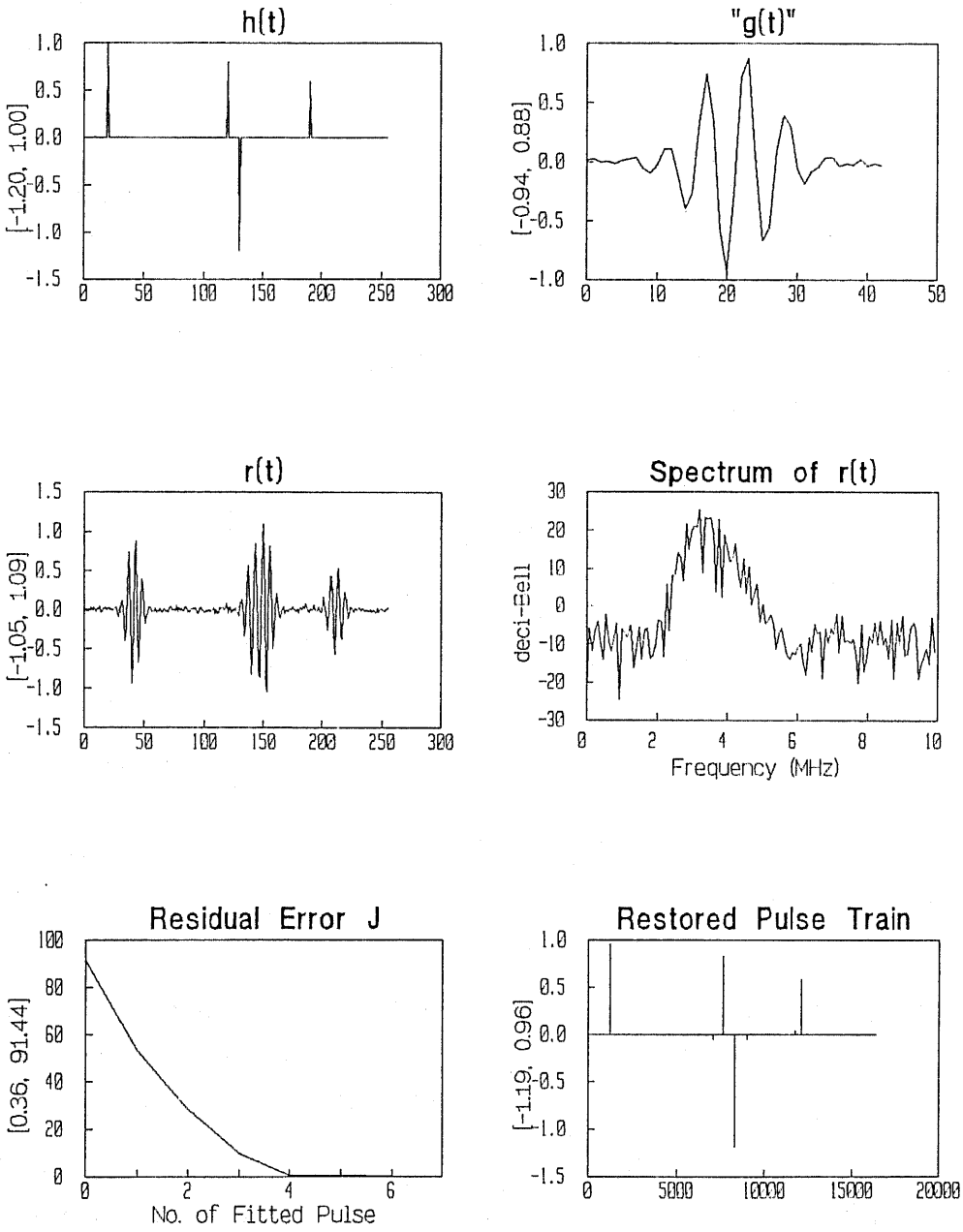

Fig. 5.2 Computer simulation of spectral fitting.

σ_ξ is the standard deviation of the fluctuation of the peak position of $R(\tau)$, which is the cross-correlation function of $g(t)+m_1(t)$ and $ag(t)+m_2(t)$. Assuming $a=1$ and the SNR defined in (5.10) is

$$\mathrm{SNR} \approx \frac{1}{\sigma_m^2} \cdot \frac{\sigma_t\sqrt{\pi}}{2} = \frac{\sigma_t\sqrt{\pi}}{2\sigma_m^2} \tag{5.14}$$

Combining this with (5.13) we obtain

$$\sigma_\xi = \sqrt{\frac{2}{\mathrm{SNR}\cdot(\omega_0^2 + 1/2\sigma_t^2)}}. \tag{5.15}$$

Setting SNR to 10000(40dB), 1000(30dB) and 100(20dB), the corresponding σ_ξ can be calculated to be respectively 0.000683, 0.00202 and 0.00683 μs.

The above values are obtained from analysis, which we wish to verify by computer simulations. First two signals are generated according to the following:

$$\begin{cases} s_1(t) = g(t) + m_1(t) \\ s_2(t) = g(t-\tau) + m_2(t) \end{cases} \tag{5.16}$$

τ is varied from 0 to 0.05μs (one sampling period) at a step of 0.01μs. $s_1(t)$ and $s_2(t)$ are sampled at 20MHz, and using the sampled data the discrete values of the cross-correlation function are calculated. To get the peak position we applied the natural spline interpolation [69] to the discrete values. In this way the peak position can be determined to a fraction of the sampling interval (Fig. 5.3).

The simulation of a specific SNR is realized by adding computer-generated white Gaussian numbers to $g(t)$ and $g(t-\tau)$, whose variance σ_{m1}^2 is given by (5.11)

$$\sigma_{m1}^2 = \frac{\int g^2(t)dt}{\mathrm{SNR}} \approx \frac{\sigma_t F_{sp}\sqrt{\pi}}{2\cdot\mathrm{SNR}} \tag{5.17}$$

Suppose that the generated numbers are m_i (i=0, 1, $\cdots$, $N-1$), and by multiplying a number r to m_i, we wish to make

$$\frac{1}{N}\sum_{i=0}^{N-1}(rm_i)^2 = \sigma_{m1}^2 \tag{5.18}$$

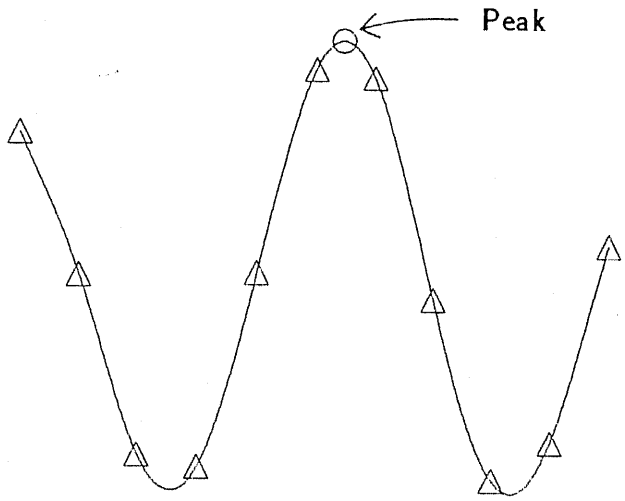

Fig. 5.3 Spline function interpolation is used to detect the peak position.

then r is determined from

$$r = \frac{N\sigma_{m1}^2}{\sum m_i^2} = \frac{N}{\sum m_i^2}\frac{\sigma_t\sqrt{\pi}F_{sp}}{2\cdot \mathrm{SNR}} \tag{5.19}$$

For a specific SNR (40, 30 and 20dB) and a specific delay τ, 30 pairs of s_1 and s_2 are generated, their cross-correlation function calculated over ± 5 sampling intervals, and the peak position detected. The average and the standard deviation of these peak positions are tabulated in Table 5.1, together with the theoretical values. It can be seen from this table that the peak position is indeed an unbiased estimation of the delay, and that its fluctuation agrees well with that predicted by our analysis. When the noise level gets higher, the fluctuation becomes slightly larger than the theoretical value, which may have been caused by the decreased accuracy of the Taylor expansion (4.18) used in the analysis. If the noise level is too high, the correlation method may break down by detecting a peak position which is about 1 period away from the true position (Fig. 5.4).

Next we will investigate the performance of the spectral fitting approach. Since the theoretical value of the standard deviation of the random fluctuation is 0.000683 at SNR=40dB, a sampling interval smaller than this value

Table 1. Results of delay estimation using the cross-correlation function and spline interpolation.

		τ						Avg. of sd.
		0.00	0.01	0.02	0.03	0.04	0.05	
40 dB	avg	0.0016	0.00931	0.01957	0.03037	0.04091	0.05006	
	sd	0.00067	0.00071	0.00074	0.00080	0.00063	0.00050	0.000675
30 dB	avg	0.00051	0.00918	0.01945	0.03031	0.04138	0.05020	
	sd	0.00215	0.00224	0.00231	0.00260	0.00209	0.00170	0.00218
20 dB	avg	0.00158	0.00871	0.01962	0.02925	0.04123	0.05069	
	sd	0.00822	0.00796	0.00851	0.00954	0.00947	0.00783	0.00859

Table 2. Results of delay estimation using the spectral fitting method described in §4.2.

		τ						Avg. of sd.
		0.00	0.01	0.02	0.03	0.04	0.05	
40 dB	avg	-0.00004	0.00998	0.01979	0.03004	0.04031	0.05018	
	sd	0.00086	0.00085	0.00068	0.00082	0.00075	0.00072	0.000778
30 dB	avg	0.00025	0.00984	0.01951	0.02996	0.04033	0.05027	
	sd	0.00227	0.00256	0.00178	0.00218	0.00156	0.00168	0.002003

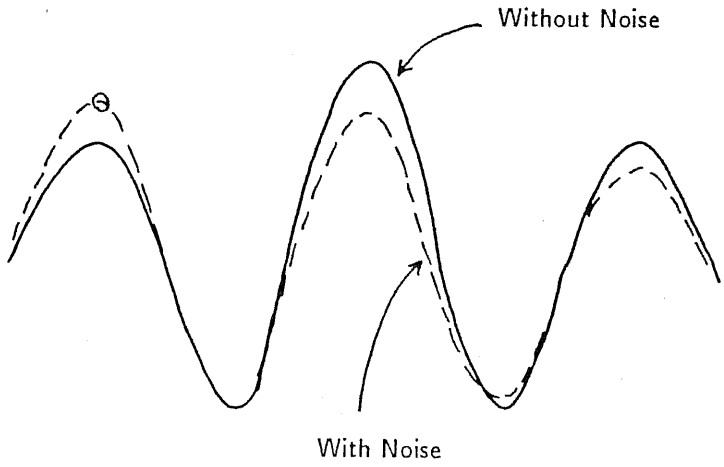

Fig. 5.4 When the noise level is too high, the peak position of the correlation function may jump over to a neighboring crest.

is necessary. The original sampling interval is 0.05μs (20MHz), so an over sampling rate of K=128 or 256 is necessary. If K=256, the sampling interval after over sampling becomes 0.05/256$\approx$0.0002μs, which is small enough so that the quantization effect of sampling will not interfere much with the observation of the fluctuation. In this case the length of FFT calculation becomes $64K$=16384 points, where 64 is the original length of $s_1(t)$ and $s_2(t)$. Typical waveforms and the spectra of $s_1(t)$ and $s_2(t)$ are illustrated in Fig. 5.5. The results of simulation are summarized in Table 5.2, from which it can be seen that the estimated delays are biasless, and their variances are somewhat larger (about 10 to 30%) than the values predicted by theory. It is noticed that the spectral fitting approach breaks down when SNR=20dB. The reason can be found by examining Fig. 5.5, from where it can be seen that the spectrum of the signal is almost buried in noise at SNR=20dB. Furthermore, the needed amount of calculation is much greater than that of calculating the discrete correlation values and using the spline interpolation to find the peak position.

In summary, we have shown through simulation that our analysis of the fluctuation of the estimated pulse position is correct, whether it is estimated

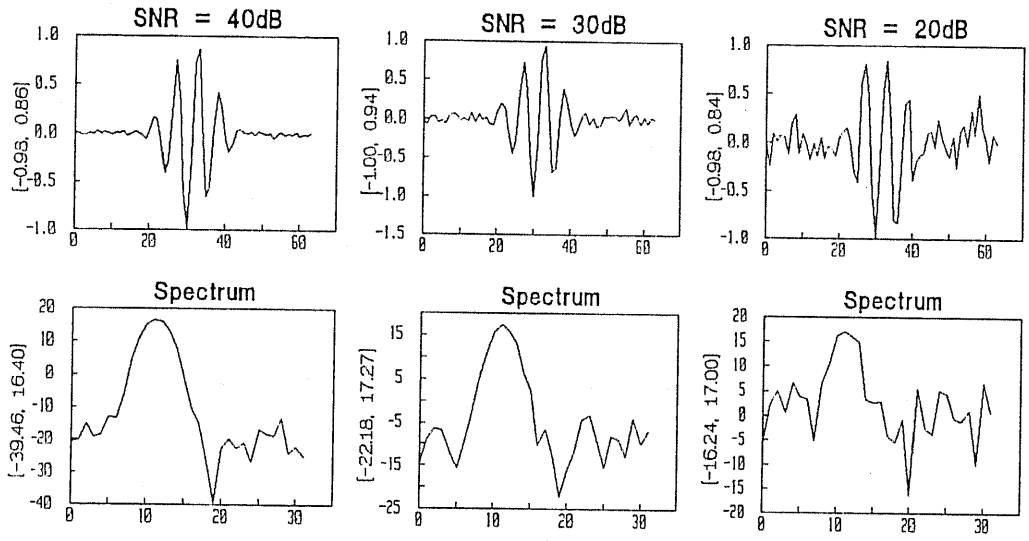

Fig. 5.5 Spectra of the pulses with different noise levels.

by spectral fitting or by the correlation method. The smaller the noise, the better the degree of agreement. Typical signals encountered in practical measurements have appearances like those of SNR=40dB, so we expect both methods to work well in practice. However, on considering the amount of calculation, the best combination would be to use the spectral fitting technique to scan the whole signal, which provides rough positions of the pulses, and then to use the correlation technique, together with spline interpolation, to get accurate estimation of the positions.

5.3 A Layered Medium with Horizontal Interfaces, Probed by Plane Waves

The forward problem, to calculate the reflected wave from the incident wave and medium parameters, can be solved using the Goupillaud's method

described in section 2.3. The parameters of the medium are assumed as the following, with reference to practical tissue parameters [1]:

$$\begin{cases} c_0 = 1.52\text{mm}/\mu\text{s(water)} & \rho_0 = 1.00\text{g/ml} & d_0 = 5\text{mm} \\ c_1 = 1.35\text{mm}/\mu\text{s(fat)} & \rho_1 = 0.92\text{g/ml} & d_1 = 10\text{mm} \\ c_2 = 1.69\text{mm}/\mu\text{s(muscle)} & \rho_2 = 1.07\text{g/ml} & d_2 = 10\text{mm} \\ c_3 = 1.52\text{mm}/\mu\text{s(blood)} & \rho_3 = 1.06\text{g/ml} & d_3 = 10\text{mm} \\ c_4 = 1.56\text{mm}/\mu\text{s(liver)} & \rho_4 = 1.06\text{g/ml} & \end{cases} \tag{5.20}$$

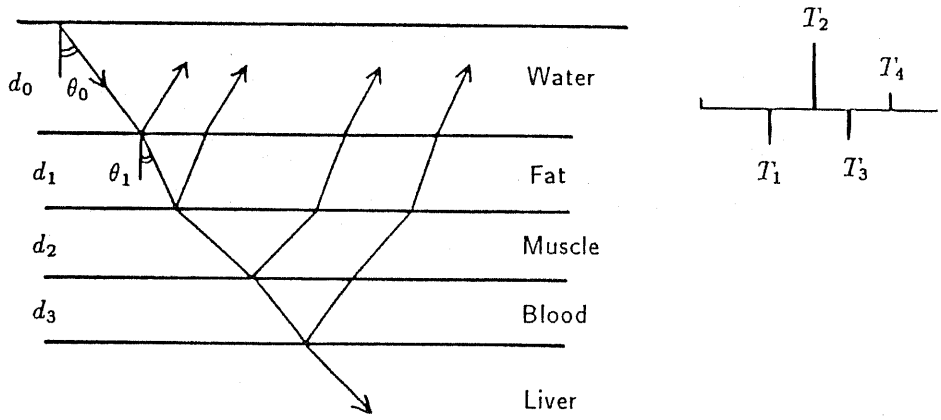

Fig. 5.6 The assumed non-uniform medium.

The medium is illustrated in Fig. 5.6. It can be seen that there are 4 primary reflections, whereas the number of multiple reflection is essentially infinite. To apply the Goupillaud's method we must decide the number of division along the depth direction. From the discussion in §4.4, we know approximately that the error in pulse position should not exceed 0.001μs. Since the total propagation time between the first and the last pulse is about

$$2 \times \left(\frac{10}{1.47} + \frac{10}{1.59} + \frac{10}{1.56} \right) \approx 39.0\mu\text{s}$$

the number of division should be about 39.0/0.001=39000. To apply the Goupillaud's method with so large a number of division needs a lot of calculation. On the other hand the meaning of using the Goupillaud's method lies in the investigation of multiple reflection. For this purpose a much smaller number of division is sufficient. So we do this simulation in two steps.

First the reflected waves are calculated using the Goupillaud's method with a small number (1000) of division. The observation is made at 20MHz, lasting 102.4μs (2048 points). Since this time is more than twice of the round-trip travel time, it is believed that multiple reflections, if any, are included in the observation. The results are illustrated in Fig. 5.7, from which it can be seen that multiple reflections, though exist, are almost negligible compared to the primary reflections.

Thus we can calculate the reflection response considering only the primary reflections. The positions of these reflections are determined from geometrical path, which is exact for plane waves:

$$T_k = 2 \cdot \sum_{i=1}^{k} \frac{d_i}{c_i / \cos\theta_i} \tag{5.21}$$

whereas the amplitudes are calculated from the equivalent impedances (see Appendix A). The results are shown in Fig. 5.8, which are basically the same as those in Fig. 5.7, except that no multiple reflection is present, and that the positions of the impulses are almost accurate, unlike those of Fig. 5.7 which are limited by the number of division in applying the Goupillaud's method.

The impulse trains of Fig. 5.8 are convolved with $g(t)$ of (5.1) and the results are sampled at 20MHz. Then random numbers are added to make the SNR around the first pulse of $s_a(t)$ to be 40dB (Fig. 5.8). The two signals $s_a(t)$ and $s_b(t)$, together with $\theta_{a0} = 0°$, $\theta_{b0} = 15°$, $c_0 = 1.52\text{mm}/\mu\text{s}$, are the input data for solving the inverse problem.

The solution of the inverse problem begins with spectral fitting, as done in §5.1. As a result the approximate positions of the pulses are obtained.

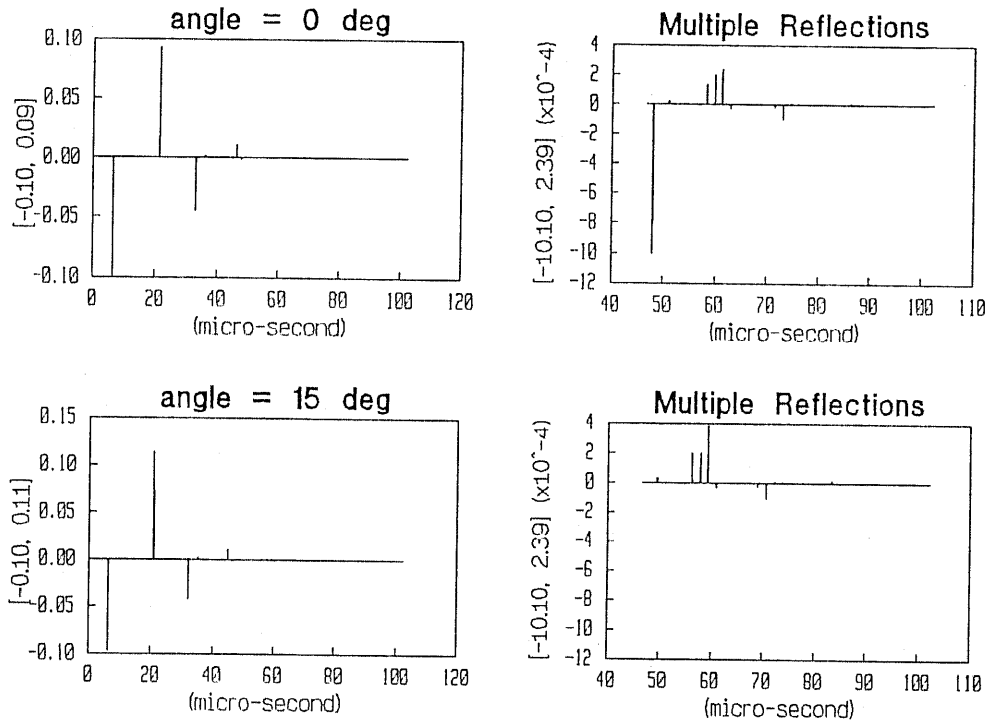

Fig. 5.7 Impulse responses of the medium of Fig. 5.6 calculated by the Goupillaud's method with 1000 as the number of division.

Then the correlation and spline interpolation method is applied to find more accurate estimation of the pulse positions. The results are summarized in Table 5.3. Finally, to calculate c_k and d_k, we notice that

$$\begin{cases} T_{ak} - T_{a,k-1} = \dfrac{2d_k \cos\theta_{ak}}{c_k} \\ T_{bk} - T_{b,k-1} = \dfrac{2d_k \cos\theta_{bk}}{c_k} \end{cases} \tag{5.22}$$

Combining (5.22) with the Snell's law, as done in (3.4), we obtain

$$c_k = \sqrt{\frac{1-u_k^2}{p_a^2 - p_b^2 u_k^2}} \quad d_k = \frac{c_k(T_{ak} - T_{a,k-1})}{2\sqrt{1-p_a^2 c_k^2}} \tag{5.23}$$

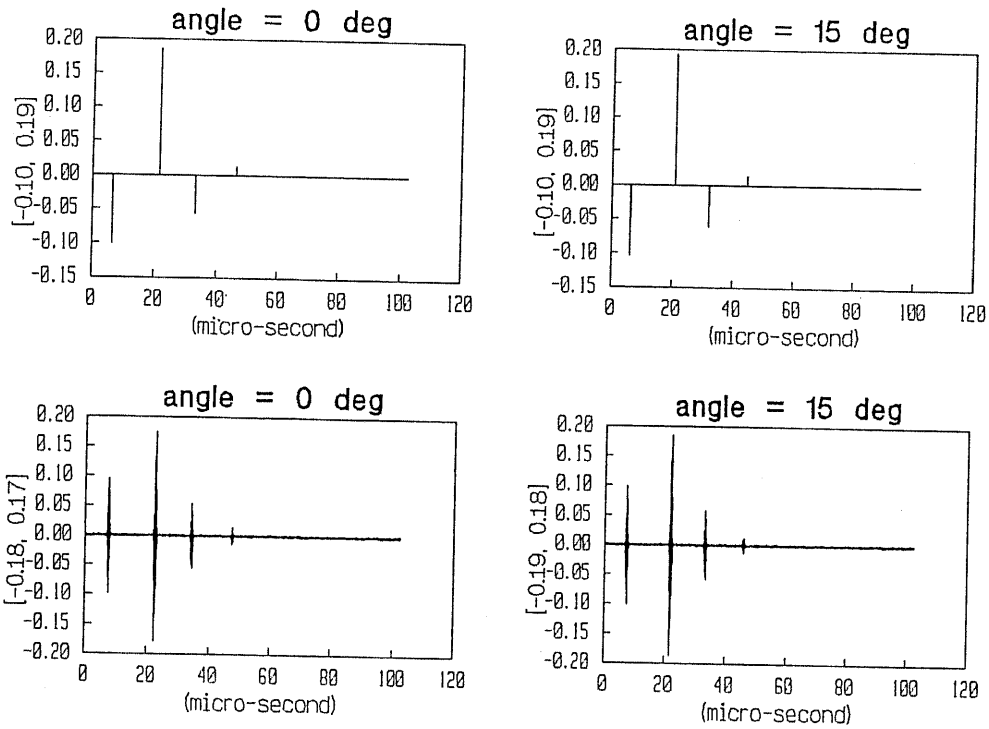

Fig. 5.8 Impulse responses of the medium of Fig. 5.6, containing only the primary reflections.

Table 5.3 Results of simulating a horizontally layered medium, probed by plane waves.

k	T_{ak}	Error	T_{bk}	Error	c_k	d_k
1	6.45	-0.128	6.22	-0.135	1.52	4.90
2	21.23	-0.159	20.61	-0.166	1.36	10.03
3	33.10	-0.128	31.97	-0.134	1.69	10.00
4	46.24	-0.146	44.66	-0.153	1.53	10.02

where

$$p_a = \frac{\sin\theta_{a0}}{c_0}, \quad p_b = \frac{\sin\theta_{b0}}{c_0}, \quad u_k = \frac{T_{ak} - T_{a,k-1}}{T_{ak} - T_{a,k-1}}$$

If the amplitude information contained in the pulses is utilized, the acoustic impedance, and the density of each layer can also be obtained. The relationship is (see (A.7))

$$r_k = \frac{\rho_k c_k / \cos\theta_{ak} - \rho_{k-1} c_{k-1} / \cos\theta_{a,k-1}}{\rho_k c_k / \cos\theta_{ak} + \rho_{k-1} c_{k-1} / \cos\theta_{a,k-1}} \tag{5.24}$$

where r_k is the kth reflection coefficient obtained from $s_a(t)$. Since this kind of relationship can always be used to find ρ_k from r_k (if known), we will not consider it further in our discussion. The c_k and d_k calculated using (5.23) are also included in Table 5.3. The results compare favorably with the assumed values of (5.20), the only source of error being the error of pulse positions.

5.4 A Layered Medium with Horizontal Interfaces, Probed by Spherical Waves

The only purpose is to check the validity of the inversion algorithm proposed in §3.4 (Fig. 3.17), and since we already know that multiple reflections are unimportant, we used directly the positions of the primary reflections, calculated according to §3.3, as the input data. The assumed medium is the same as that of Fig. 5.6, and the two transmitter-receiver distances are $l_a = 0$mm, $l_b = 5$mm. To simulate the influence of measurement noise, random numbers are added to the calculated travel times, whose variance is $(0.000683\mu s)^2$ for an assumed SNR of 40dB (see (5.15)). The results are summarized in Table 5.4. It can be seen that the influence of measurement noise is larger compared to Table 5.3. This is expected because the transmitter-receiver distance of 5mm corresponds to an incident angle of only $\tan^{-1}(5/35/2) \approx 4°$ with respect to the last layer.

Table 5.4 Results of simulating a horizontally layered medium, probed by spherical waves.

k	T_{ak}	Error	T_{bk}	Error	c_k	d_k
1	6.58	-0.0001	7.36	0.0004	1.52	5.00
2	21.40	0.0015	21.69	-0.0008	1.36	10.06
3	33.23	0.0004	33.39	0.0007	1.68	9.93
4	46.39	-0.0007	46.50	0.0003	1.50	9.87

5.5 A Layered Medium with Non-Parallel Interfaces, Probed by Spherical Waves

Here the situation is in parallel with that of the last section. Parameters of the medium are assumed as the following:

$$\begin{cases} c_0 = 1.52\text{mm}/\mu\text{s(water)} & \rho_0 = 1.00\text{g/ml} & d_0 = 5\text{mm} & \gamma_0 = 5^\circ \\ c_1 = 1.35\text{mm}/\mu\text{s(fat)} & \rho_1 = 0.92\text{g/ml} & d_1 = 10\text{mm} & \gamma_1 = 0^\circ \\ c_2 = 1.69\text{mm}/\mu\text{s(muscle)} & \rho_2 = 1.07\text{g/ml} & d_2 = 10\text{mm} & \gamma_2 = -5^\circ \\ c_3 = 1.52\text{mm}/\mu\text{s(blood)} & \rho_3 = 1.06\text{g/ml} & d_3 = 10\text{mm} & \gamma_3 = 3^\circ \\ c_4 = 1.56\text{mm}/\mu\text{s(liver)} & \rho_4 = 1.06\text{g/ml} & & \end{cases}$$

The only difference with those of (5.20) is that the planes are inclined. To solve the inverse problem signals measured at 3 different locations are necessary, and we selected $l_a = 0\text{mm}$, $l_b = 5\text{mm}$, $l_c = 10\text{mm}$. The traced rays are shown in Fig. 5.9.

Finally, the results of inversion using the approach described in §3.5 are summarized in Table 5.5. As before, random fluctuations corresponding to SNR=40dB have been added to the pulse positions, T_{ak}, T_{bk} and T_{ck}.

5.6 The Influence of Various Kinds of Errors

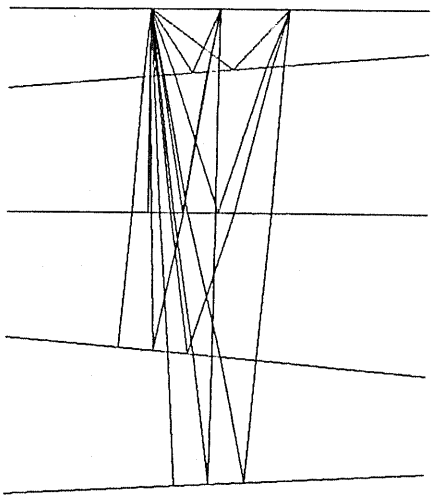

k	T_{ak}	T_{bk}	T_{ck}
1	6.5539	7.0722	8.8725
2	21.3934	21.7246	22.6248
3	33.1207	33.5779	34.3503
4	46.3103	46.2628	46.4504

Fig. 5.9 Results of ray tracing in a medium with non-parallel interfaces.

Table 5.5 Results of simulating a layered medium with non-parallel interfaces, probed by spherical waves.

k	T_{ak}	T_{bk}	T_{ck}	c_k	d_k	γ_k
1	6.55	7.07	8.87	1.52	5.00	5.03
2	21.39	21.72	22.63	1.35	9.99	0.02
3	33.12	33.58	34.35	1.68	9.93	-4.92
4	46.31	46.26	46.45	1.51	9.93	3.02

In this section we will investigate the influence of the following kinds of errors:

(1) All the pulse positions are shifted by the same amount, which might happen because the beginning of a pulse is hard to identify.

(2) Random fluctuations of varying amplitudes of pulse positions. corresponding to different signal-to-noise ratios.

(3) Mistaking non-parallel interfaces by horizontal interfaces.

(4) Inaccurate knowledge of the positions of the transducers.

The inversion algorithm employed in this study is the one described in §3.4, which is for point-like transmitter & receiver, and horizontally layered media. The assumed parameters of the medium is the same as those of (5.20), and the two transmitter-receiver distances are $l_a = 0\text{mm}$, $l_b = 5\text{mm}$, the same as those of §5.4.

The results are summarized in Fig. 5.10, from which it can be seen that

(1) The influence of shifting all the pulses by the same amount is only apparent in the values of the first layer.

(2) Random fluctuation of the pulse positions, the non-zero inclination of each interface, and inaccurate knowledge of the position of the transducers, affect the results significantly.

The problem of random fluctuation of the pulse positions can be solved to a certain extent by taking the average of many trials. One can average to get more accurate pulse positions, or perform the inversion with noisy data and then average the results. Probably both approaches lead to similar results (see §6.4), but the latter requires more calculation. The inclination of the interfaces can only be dealt with by considering a layered model of non-parallel interfaces, whereas inaccurate knowledge about transducer positions should be made more accurate before calculation.

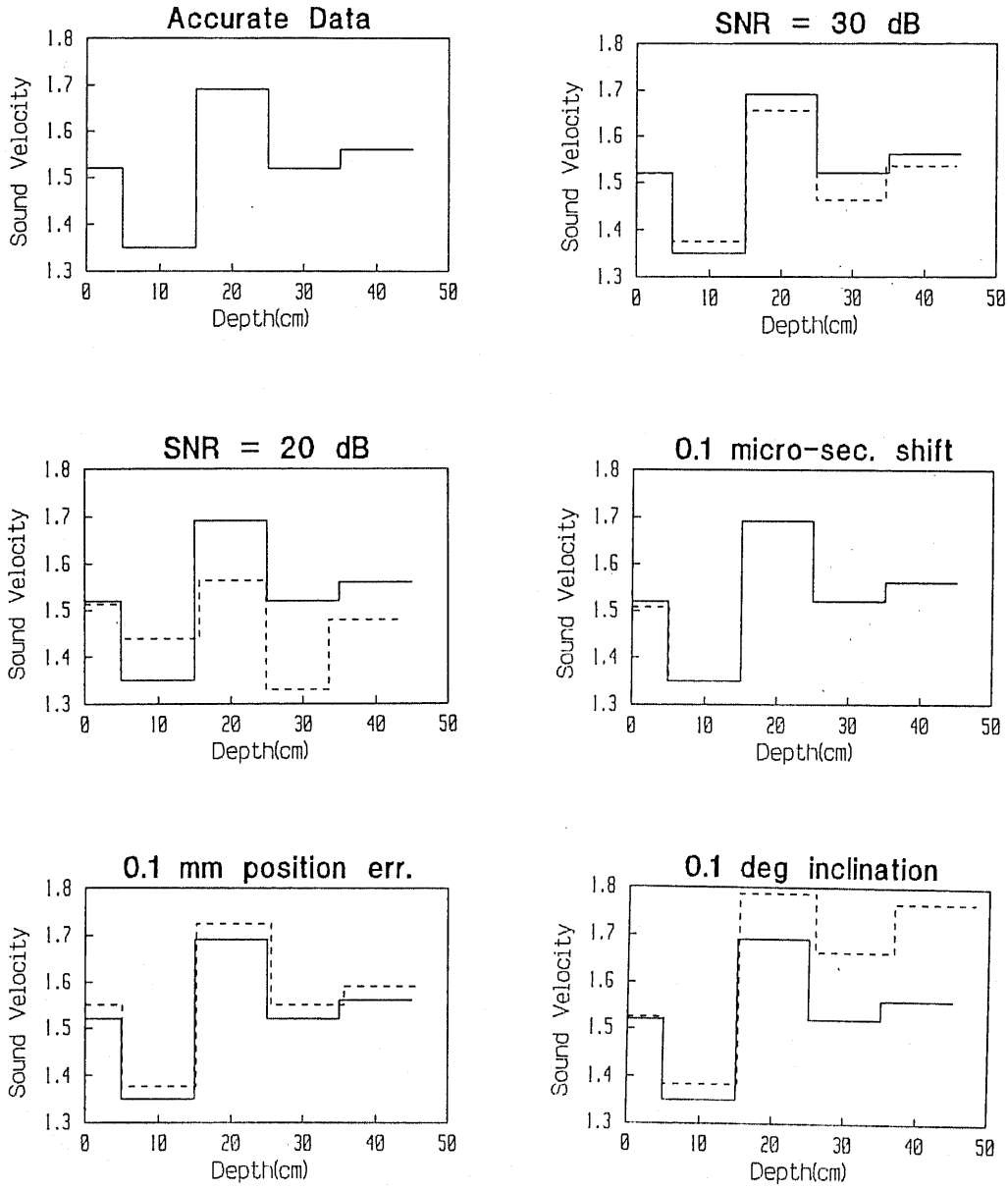

Fig. 5.10 The influence of various kinds of errors

The drastic variation in the results caused by small variation of the conditions indicates the ill-conditioned character of the inverse problem. However, it should be pointed out that, if our interest is not in the reconstructed medium parameters, but in applying them to compensate for the additional amount of variation in travel time brought about by the layered medium, then we may find that the results are not that bad. This can be shown by calculating the travel time from the transmitter down to the last interface, and back to the receiver, as a function of l (see Fig. 5.9), for the original as well as the reconstructed medium. One example of this calculation is shown in Fig. 5.11, in which it can be seen that, even though the calculated values differ much from the original values, the travel times are almost the same for the two models. This means that, although the reconstructed model is inaccurate in itself, it can still serve the purpose of calculating the additional amount of travel time variation caused by the nonuniformity.

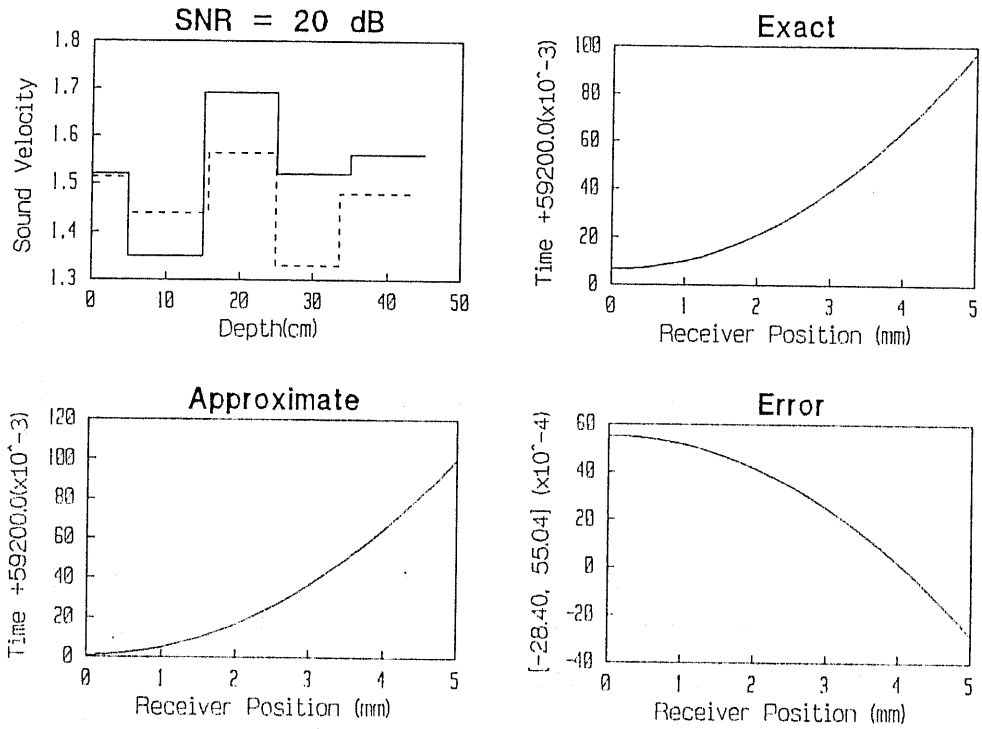

Fig. 5.11 The travel times from the transmitter to the last interface, and back to the receiver, calculated for the original model and the (inaccurately) reconstructed model. It can be seen that their difference is of the same order as the error of the data for inversion.

6

Experimental Measurements

6.1 The Deterioration of the Image Qualities Caused by a Distortion Plate

The experimental setup is shown in Fig. 6.1. Two wire targets are put at about 40 and 60mm below a linear transducer, and all these are immersed in water (22°C). A distortion plate made of silicon resin, with 6mm wide, 0.36mm deep ditches cut on one side, is inserted between the transducer and the targets. The sound velocity of the plate is about 0.96mm/μs, whereas in water it is 1.488mm/μs, so that the difference in one-way travel time introduced by this plate is about 0.133μs.

The transducer has 128 elements, each spaced 0.64mm apart. Each element can work independently as a transmitter or a receiver. We used only the central 64 elements, and collected the signal for all combinations of transmitting and receiving element numbers, so that in all we get 64×64=4096 signals. This dataset can be processed by a computer to test any focusing or compensating algorithms. Signals are sampled at 40MHz with 10-bit precision. The first 500 points have been skipped and the following 4096 points are recorded. For the sake of comparison, signals have been collected with the distortion plate present, as well as absent.

The synthesis of a B-scope picture from one dataset is simple in the case of a uniform medium. Only geometrical factors need to be compensated for. Consider the synthesis of a scan line. The most complicated processing

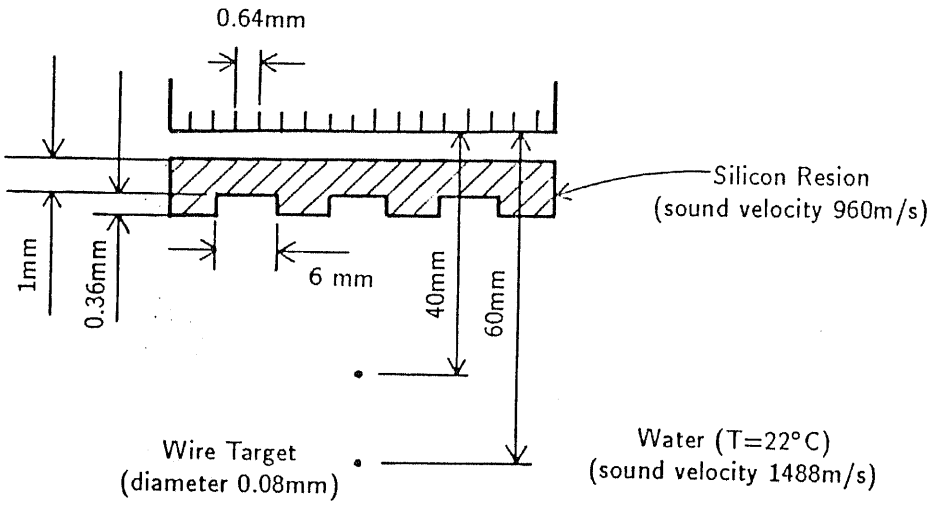

Fig. 6.1 A distortion plate is inserted between the transducer and the wire targets.

is fixed focusing in transmitting and dynamic focusing in receiving. Suppose that $2N+1$ elements are involved in this scan line, and the $(2N+1)\times(2N+1)$ signals are available:

$$s_{ij}(t) \quad (i,j = 0,1,\cdots,2N)$$

where i is the transmitting, j is the receiving element number.

Referring to Fig. 6.2, fixed focusing in transmitting can be realized by delaying $s_{ij}(t)$ by τ_i, where

$$\tau_i = \frac{1}{c_0}\left\{\sqrt{d^2+(N\Delta)^2} - \sqrt{d^2+[(i-N)\Delta]^2}\right\}. \tag{6.1}$$

τ_i is zero for elements at both ends of the aperture ($i = 0,\ 2N$), is maximum for the central element ($i = N$).

Next we consider dynamic focusing in receiving. We only have to move the focal point from near region to far region. At time instant t, the focal point is at $d(t) = c_0 t/2$, so that the delay introduced into the signals received by the jth element should be

$$\zeta_j(t) = \frac{1}{c_0}\left\{\sqrt{\left(\frac{c_0 t}{2}\right)^2+(N\Delta)^2} - \sqrt{\left(\frac{c_0 t}{2}\right)^2+[(i-N)\Delta]^2}\right\}. \tag{6.2}$$

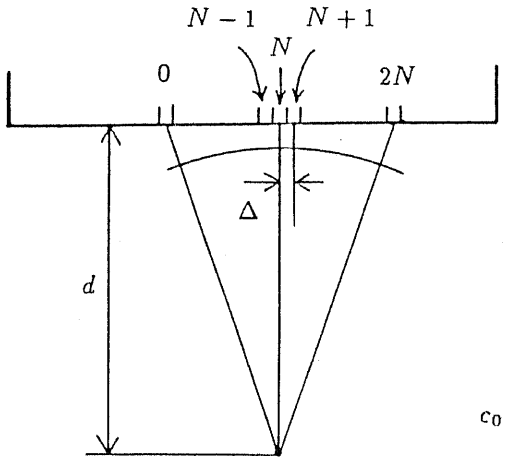

Fig. 6.2 Focusing the array at a point.

However this formula has some defects in it. Putting $j = N$ we get

$$\zeta_N(t) = \frac{1}{c_0}\left\{\sqrt{\left(\frac{c_0 t}{2}\right)^2 + (N\Delta)^2} - \left(\frac{c_0 t}{2}\right)^2\right\}. \tag{6.3}$$

which depends on t. Under the assumption that the medium is uniform, the signal received by the central element can be uniformly mapped to the physical depth. If a time dependent delay is added to it, this merit of uniform mapping is lost. To avoid this problem of time distortion, we considered shifting forward the signals received by the elements which are not at the center. The amount of shifting is

$$\zeta_j(t) = \frac{1}{c_0}\left\{\sqrt{\left(\frac{c_0 t}{2}\right)^2 + [(j-N)\Delta]^2} - \left(\frac{c_0 t}{2}\right)^2\right\}. \tag{6.4}$$

which also compensates for the travel time difference.

Summing up all the signals which have been appropriately shifted to incorporate the focusing requirements of transmitting and receiving, finally we get

$$s(t) = \sum_{i=0}^{2N} \sum_{j=0}^{2N} s_{ij}(t - \tau_i + \zeta_j) \tag{6.5}$$

where τ_i, ζ_j are given by (6.1), (6.4), respectively.

One can further improve this processing by introducing a weighting function along the aperture to compress the side lobes. As is well known [56], the far field directivity is approximately the Fourier transform of the intensity distribution, so the problem is analogous to the selection of an appropriate window function for spectral analysis, compromising between the contradictory requirements of high resolution and low sidelobe level.

Because of limited computer resources we only performed a very simple processing on the dataset: dynamic focusing in transmitting and non-focusing in receiving. By the principle of reciprocity this is equivalent to non-focusing in transmitting and dynamic focusing in receiving. The reason that such a peculiar focusing has been adopted is because that the dataset consists of 64 files, each file contains all the signals received by an element when the transmitting element is varied over the whole aperture from 1 to 64 (Fig. 6.3), so that it is relatively easy to access the signals for one receiving element and arbitrary transmitting element.

Finally there is the problem of interpolation: $s_{ij}(t)$ are sampled data so that their values are only available on the sampling instants, whereas the needed amount of shift cannot be expected to be integral multiples of the sampling interval. One may use linear interpolation, spline interpolation, or the Fourier interpolation. The final method is based on the sampling theorem, so is theoretically exact. However the calculation requirement is very great, even using the efficient FFT algorithm. Here we used the cubic spline interpolation [69]. Using an aperture size of $2N+1$=31, the results are shown in Fig. 6.4 (without distortion plate) and Fig. 6.5 (with distortion plate). It

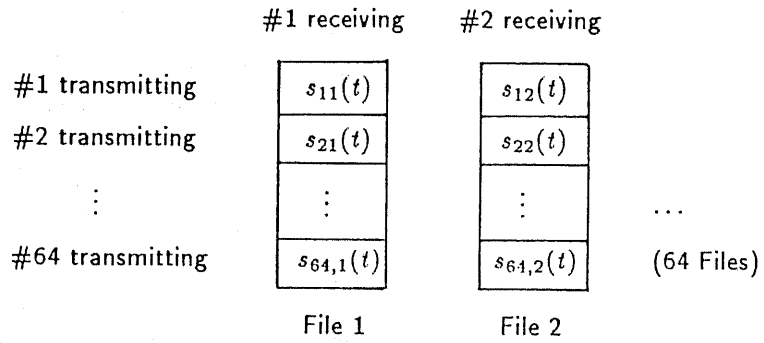

Fig. 6.3 Structure of the dataset.

can be seen that the image qualities are greatly affected by the distortion plate. The computation time for the generation of one such B-scope picture is about 9 minutes using an Hewlett-Packard 9000 series 360CH engineering workstation.

6.2 Compensating for the Distortion Effect Using Travel Time Residuals

The introduction of a distortion plate between the transducer and the traget (Fig. 6.1) disturbs the acoustic wave field, the most important disturbance being the variation of the travel time. In this section we will show the results of compensating for this variation using the reflection from a point target.

When a point target is insonified it generates a secondary field which is spherical and propagates outward (Fig. 6.6). So, if the positions of the pulses are ploted as a function of element number, under ideal conditions we obtain an arc (Fig. 6.7) which is part of a circle.

However, when there is a non-uniform medium lying between the transducer and the wire target, there will be another component of fluctuation superimposed on the circle (Fig. 6.7). By fitting a circle to this curve and subtract it from the curve, we can obtain the additional amount of delay

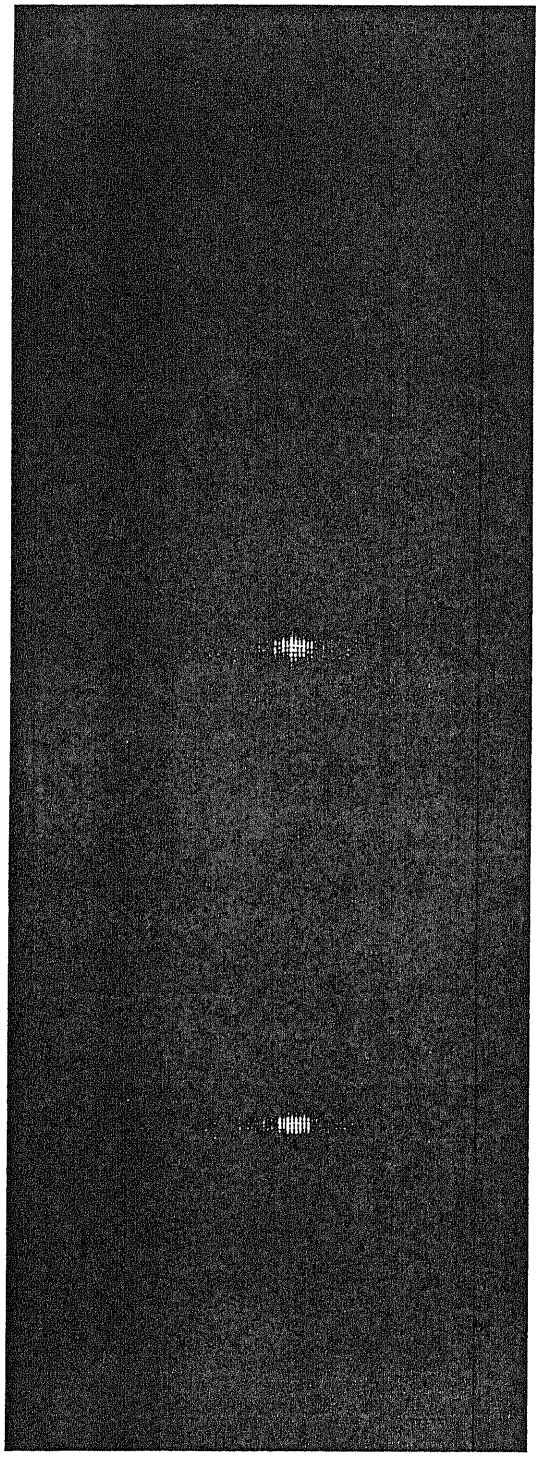

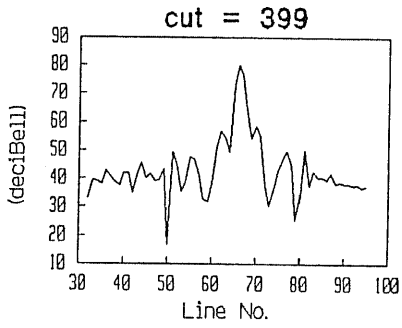

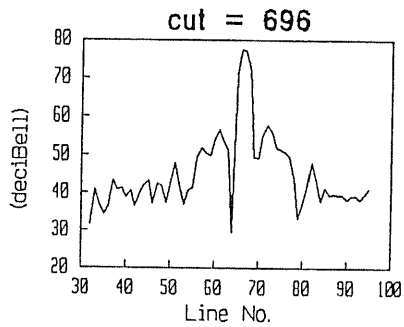

Fig. 6.4 Without a distortion plate.

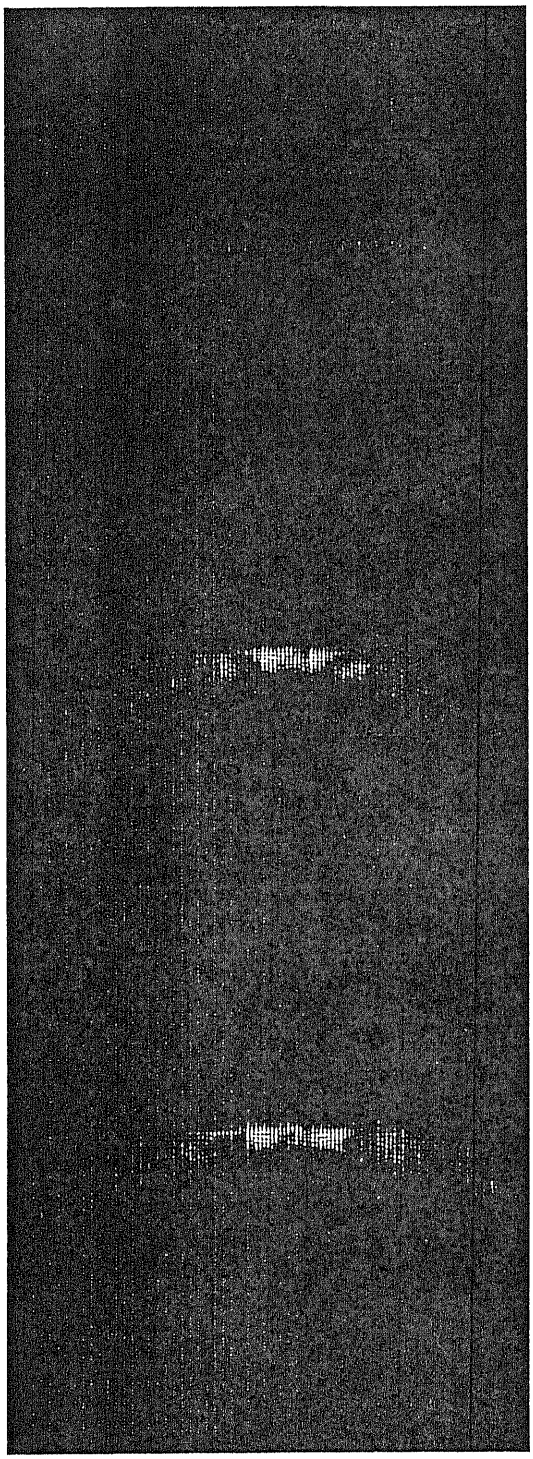

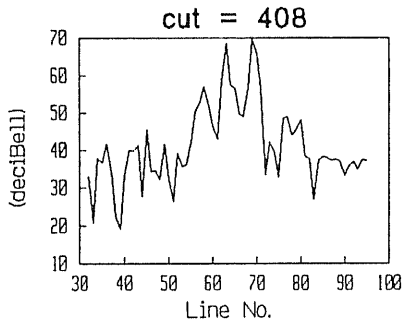

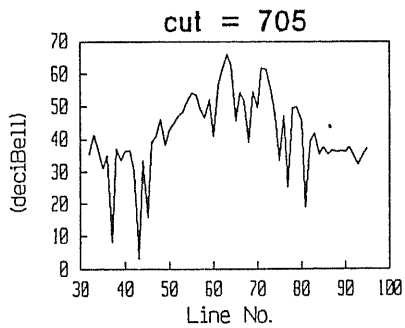

Fig. 6.5 With a distortion plate.

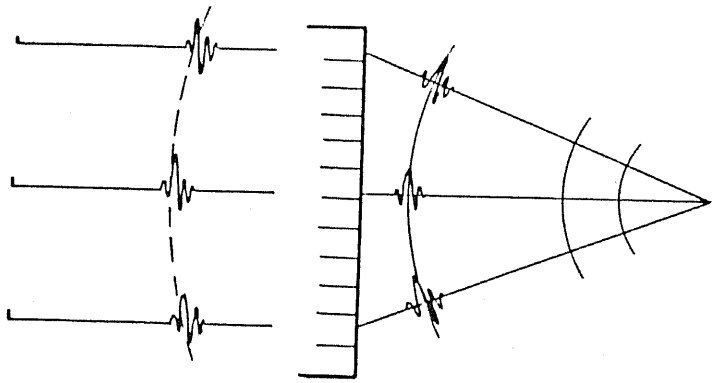

Fig. 6.6 An insonified point reflector generates a spherical wave field which propagates outward.

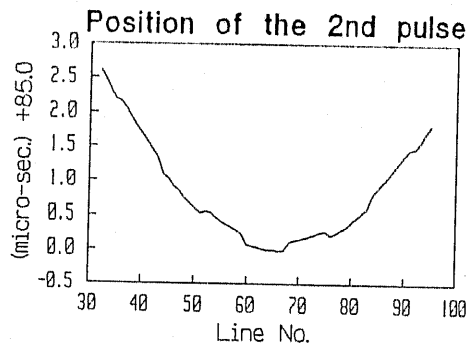

Fig. 6.7 Pulse position versus element number.

caused by the non-uniform medium, which we call the travel time residual. Specifically the ideal curve of t_i versus i is given by

$$(c_0 t_i)^2 = (i\Delta + a)^2 + d^2 \tag{6.6}$$

Since fitting a circle to the $t_i \sim i$ is not so easy, we may instead fit a parabolic curve to the $t_i^2 \sim i$ curve. The 3 parameters are c_0, a and d (Δ is the element pitch, which is assumed to be known). The insonification can be made by any element and the results are the same. Using the principle of reciprocity

again, we may also obtain the $t_i \sim i$ curve from the "varying transmitter, fixed receiver" data, so that we need only one file and do not have to open up all the files (Fig. 6.3). Finally the obtained travel time residual is displayed in Fig. 6.8. It can be seen that the results agree well with the expected values.

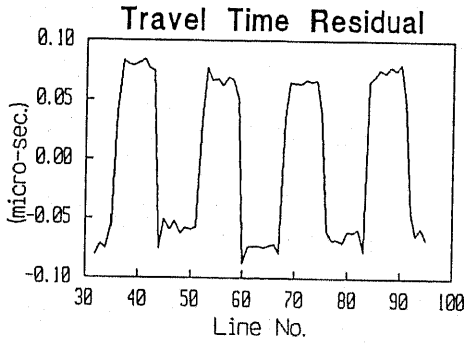

	Obtained	Expected
ditch width	~10 elements	$\frac{6 \text{ mm}}{0.64 \text{ mm}} \approx 9.4$
ditch depth	$\sim 0.14\ \mu s$	$0.133\ \mu s$

Fig. 6.8 Travel time residual estimated from the dataset with the distortion plate present.

Once the travel time residual is obtained, it can be used for compensation. The modified formula is

$$s(t) = \sum_{i=0}^{2N} \sum_{j=0}^{2N} s_{ij}(t - \tau_i + \zeta_j + u_i + u_j) \tag{6.7}$$

where u_i is the ith residual. The B-scope picture generated with this formula is shown in Fig. 6.9, which should be compared with the pictures of Fig. 6.4 and Fig. 6.5. the improvement of the image qualities after compensation is obvious.

In achieving this improvement we have used the reflection from a point reflector. However in clinical diagnosis we are not so lucky as to always have a point reflector in the region of interest. So we must seek to other means to find the travel time residual. One of the approaches is to perform inverse scattering to find the spatial distribution of sound velocity in the non-uniform medium. And the simplest model of the non-uniformity is a layered medium.

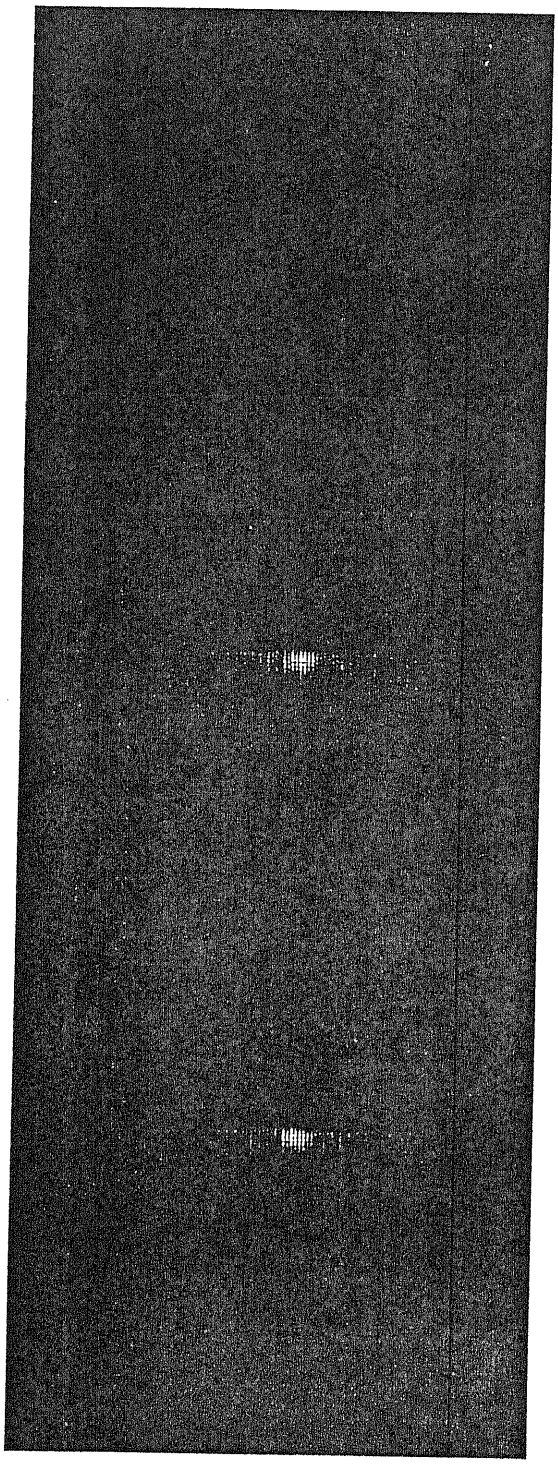

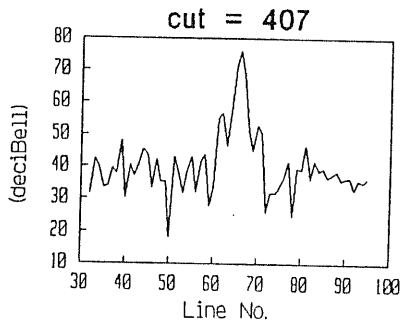

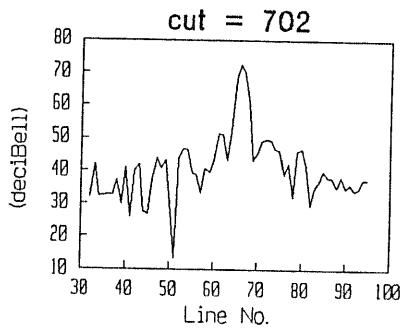

Fig. 6.9 With a distortion plate, after compensation

6.3 A Layered Medium with Horizontal Interfaces

The calculation of a one-dimensional sound velocity profile has been treated in §2.4, §3.1 for plane wave incidence, in §3.3 for spherical wave incidence (using the ray approximation). In the following experiment we used individual elements of a linear array transducer (the same as the one used in the previous section) to transmit and receive acoustic waves. Since the elements are very small (~0.64mm) in size, the waves are approximately spherical, and the procedure (Fig. 3.15) described in §3.4 should be applied.

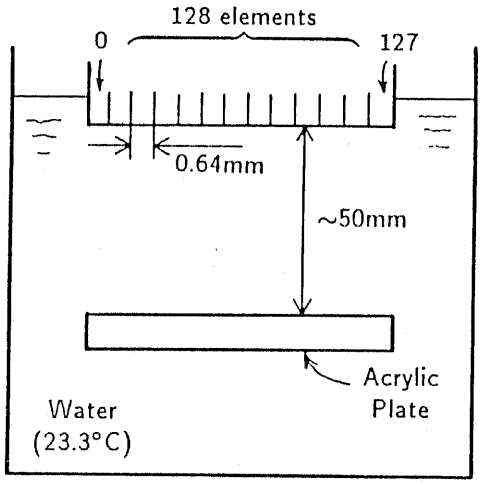

Fig. 6.10 Experimental setup for inverse scattering measurement.

The setup of the measurement is shown in Fig. 6.10. An acrylic plate (a kind of plexiglass) is put at about 50mm below the tranducer and both are immersed in water (23.3°C). The elements are numbered 0, 1, ···, 127 from left to right. Firing the 20th element, the reflection is received by all the 128 elements. These signals are sampled at 40MHz with 10-bit precision. The first 2000 points have been skipped, and the following 4096 points are recorded. Part of the data are shown in Fig. 6.11.

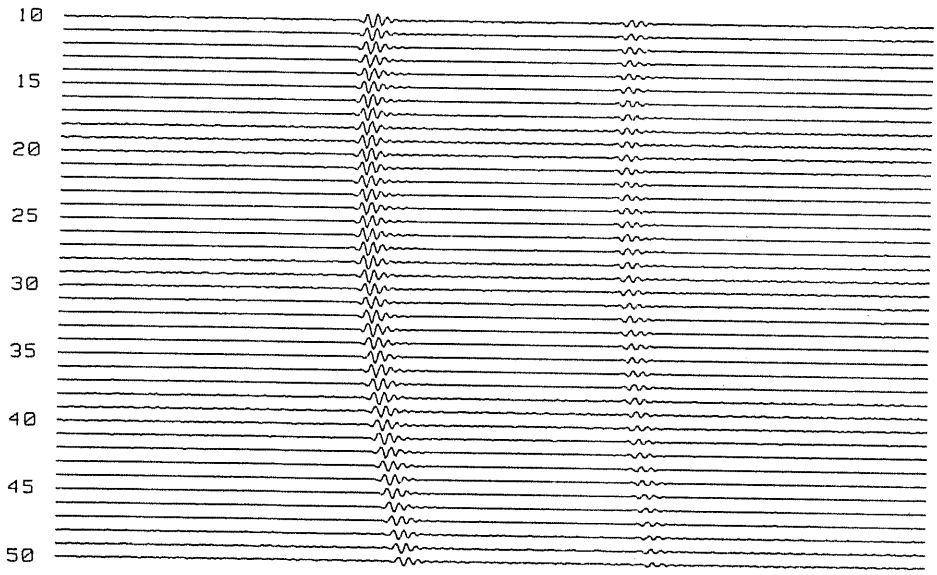

Fig. 6.11 Signals measured with the setup in Fig. 6.10.

The processing of these data follows exactly the same line as that of simulation (§5.4), with only one exception: although we have tried to put the transducer and the plate parallel to each other, there is still a small angle between the two. From the results in §5.6 we know that even a small inclination can result in great errors in the calculated sound velocity. To compensate for this inclination we collected another dataset, which also contains 128 signals, which are obtained by firing the 128 elements one by one, and receiving the reflection by the same element that is used in transmission. the position of the first pulse of these signals is ploted as a function of element number in Fig. 6.12.

By fitting a straight line to this plot, the slope is found to be 0.0042μs/ 0.64mm. Assuming the sound velocity of water to be 1.492mm/μs, the angle between the plate and the transducer can be found

$$\gamma = \tan^{-1}(1.492 \times 0.0042/0.64/2) \approx 0.28^\circ \qquad (6.8)$$

Using this angle, the correction of the pulse positions and transmitter-receiver distances before being input to the inversion algorithm is performed in the

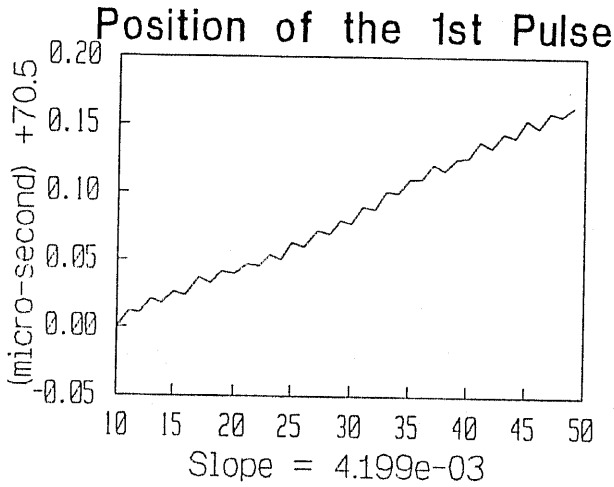

Fig. 6.12 Data used to estimate the inclination.

following way (Fig. 6.13)

$$\begin{cases} l' = l\cos\gamma \\ T_k' = T_k - l\sin\theta/c_0 \quad (k = 1, 2) \end{cases} \tag{6.9}$$

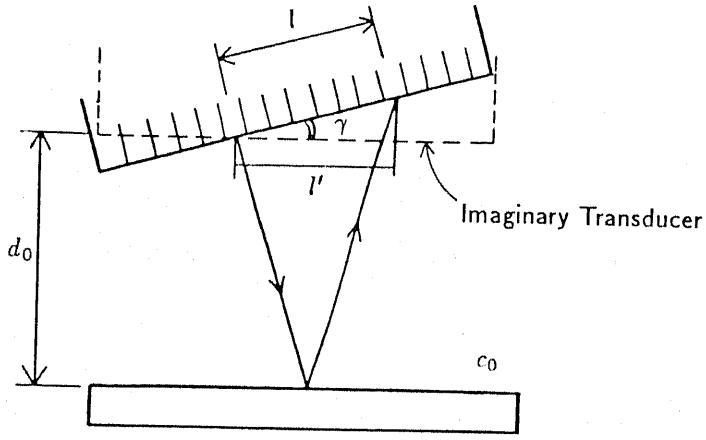

Fig. 6.13 Compensating for the inclination.

It is possible to calculate the sound velocity c_0, c_1 and the thickness d_0 and d_1 (Fig. 6.13) using any two received signals corresponding to two

different transmitter-receiver distances l_a and l_b, but the difference between l_a and l_b should not be too small. Or the results will be very sensitive to errors in pulse positions (see §4.4). On the other hand it is not suitable to use too large an l because the signal-to-noise ratio falls down as l gets larger.

The pulse positions are estimated using the cross-correlation function, and are ploted in Fig. 6.14. It is observed that there is a periodic variation among the neighboring positions, which might have been caused by some electronics of the array transducer. To avoid the error caused by this factor, we used only the signals received by even-numbered elements (of course odd-numbered data will also be all right).

The results are summarized in Table 6.1. Using the signals received by the elements (20, 30), (20, 32), $\cdots$, (20, 50), 11 answers are obtained, and their average $\pm$ standard deviations are as the following:

$$c_0 = 1.474 \pm 0.004, \quad d_0 = 51.96 \pm 0.13$$
$$c_1 = 2.767 \pm 0.026, \quad d_1 = 10.38 \pm 0.10$$

The real value of thickness d_1 is measured to be 10.0mm, while the sound velocity in the acrylic plate, calculated from the time interval between the two pulses in the signal received by the 20th element, is found to be 2.729mm/μs. There are some biases in our preliminary results, which might have been caused by the existence of a thin acoustical lens on the surface of the array transducer.

6.4 A Layered Medium with Non-Parallel Interfaces

There is nothing new in the setup, except that the non-uniformity is replaced by two acrylic plates, making an angle to each other (Fig. 6.15). It can be viewed as a 5-layer model, made up of water, acrylic plate, water, acrylic plate and water again.

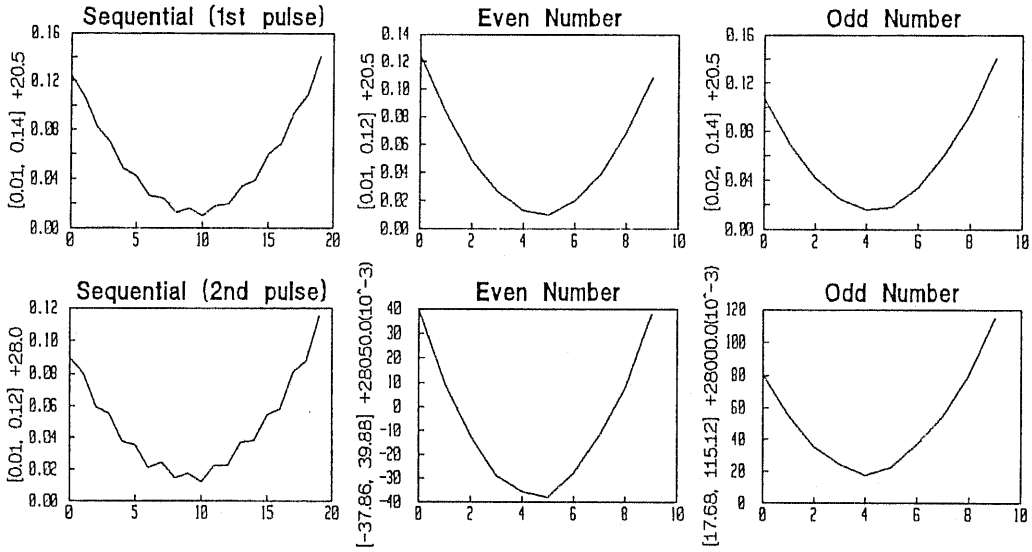

Fig. 6.14 Pulse positions estimated from the data shown in Fig. 6.11.

Table 6.1 Results calculated from the data of Fig. 6.14.

	c_0	d_0	c_1	d_1
(20, 30)	1.48	52.21	2.81	10.56
(20, 32)	1.47	51.99	2.81	10.52
(20, 34)	1.47	51.71	2.76	10.34
(20, 36)	1.47	51.78	2.72	10.22
(20, 38)	1.47	51.89	2.79	10.47
(20, 40)	1.47	51.98	2.76	10.34
(20, 42)	1.47	52.89	2.77	10.37
(20, 44)	1.48	52.02	2.75	10.33
(20, 46)	1.48	52.01	2.74	10.28
(20, 48)	1.48	52.03	2.76	10.36
(20, 50)	1.48	52.05	2.77	10.38

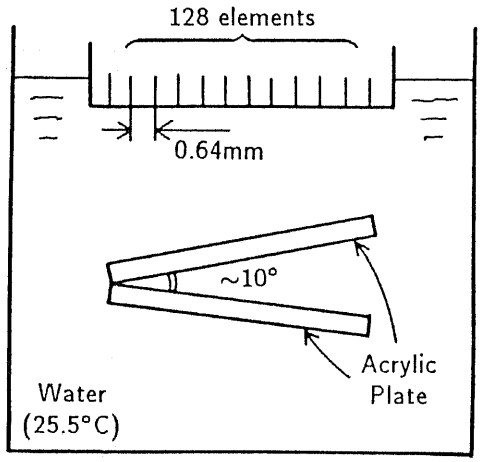

Fig. 6.15 Experimental setup.

The primary reflection consists of 4 pulses, as shown in Fig. 6.16. The signals are obtained using the 63rd element as a transmitter and all the elements as receivers. The pulse positions are plotted in Fig. 6.17.

For the same reason as mentioned in the previous section, we used only the signals received by even-numbered elements. These signals are divided into groups, with 3 signals in each group, and the parameters c_i, d_i, γ_i (i=0, 1, 2, 3) are calculated from the pulse positions in the same way as done in simulation (§5.6). The results are summarized in Table 6.2.

We may also process the data by first fitting parabolic curves to the plots in Fig. 6.17, and assuming 3 arbitrary distances l_a, l_b, l_c, for which the pulse positions are obtained from the fitted curves. In this way the influence of the random fluctuation of the pulse positions caused by measurement noise can be suppressed. Numerical calculations indicate that the accuracy is higher if we fit parabolic curves to $T_i^2 \sim i$ instead of to $T_i \sim i$ directly. One result with $l_a = -6$mm, $l_b = 0$mm, $l_c = 4$mm is tabulated in Table 6.3.

Finally we notice that the horizontal-interface medium treated in the previous section is a special case of non-parallel media. So we reclaculated for the c_i, d_i, γ_i (i=0,1) using the data of Fig. 6.11. We adopted the parabolic

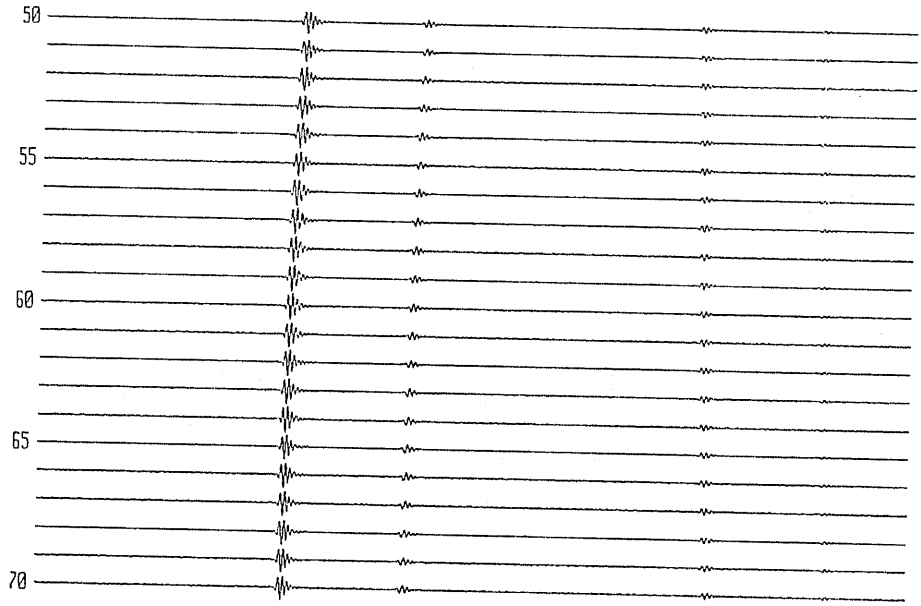

Fig. 6.16 Signals measured with the setup of Fig. 6.15.

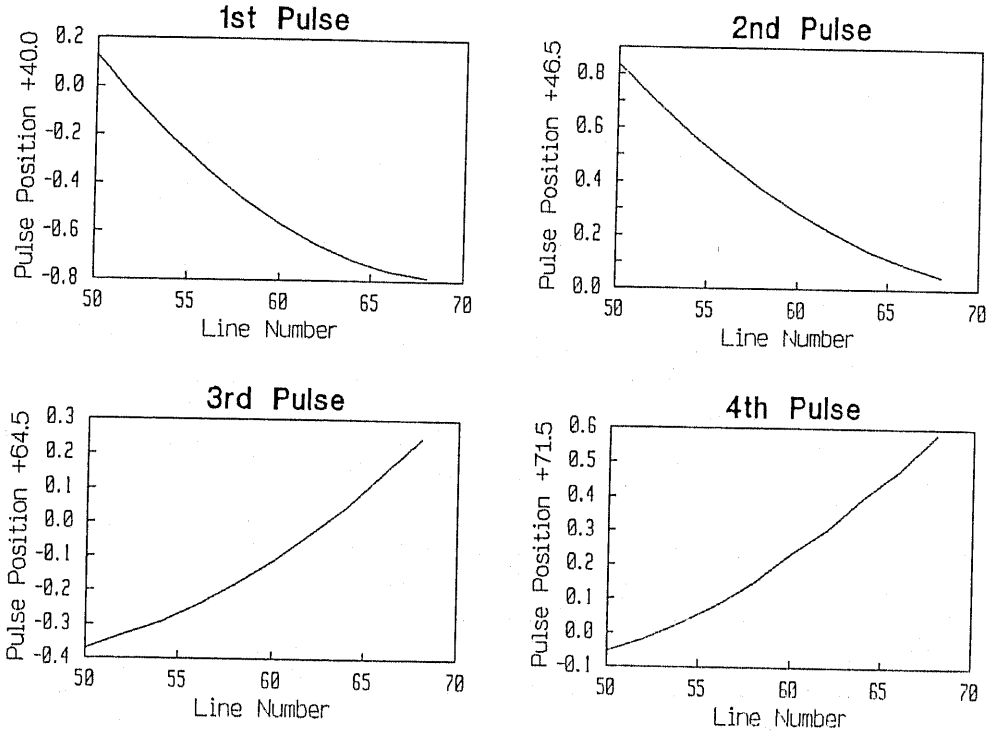

Fig. 6.17 Positions of the pulses plotted against the element number.

Table 6.2 Results calculated from the data of Fig. 6.17

Receiving Elements		47 57 67	48 58 68	49 59 69	50 60 70	51 61 71	52 62 72	53 63 73	54 64 74	55 65 75	56 66 76	Average	Std. Devi.
c_k	1	1.49	1.50	1.50	1.50	1.49	1.49	1.49	1.49	1.49	1.49	1.49	0.00
	2	2.72	2.71	2.72	2.71	2.68	2.72	2.72	2.73	2.69	2.71	2.71	0.02
	3	1.48	1.52	1.46	1.58	1.52	1.42	1.58	1.44	1.48	1.57	1.50	0.05
	4	2.42	2.22	2.57	2.72	2.88	2.90	2.60	3.32	2.68	2.34	2.67	0.30
d_k	1	29.14	29.38	29.33	29.39	29.21	29.23	29.13	29.22	29.23	29.27	29.25	0.09
	2	10.03	9.99	10.02	10.00	9.88	10.05	10.05	10.09	9.93	10.02	10.01	0.06
	3	13.50	13.89	13.26	14.39	13.81	12.92	14.36	13.14	13.46	14.33	13.71	0.51
	4	8.93	8.21	9.48	10.04	10.63	10.67	9.59	12.27	9.87	8.64	9.83	1.11
γ_k	1	4.28	4.37	4.34	4.37	4.29	4.32	4.30	4.36	4.32	4.35	4.33	0.03
	2	4.35	4.38	4.34	4.37	4.31	4.36	4.35	4.37	4.33	4.37	4.35	0.02
	3	-5.69	-5.93	-5.51	-6.31	-5.89	-5.21	-6.30	-5.40	-5.63	-6.28	-5.81	0.37
	4	-5.68	-6.06	-5.44	-6.14	-5.81	-5.15	-6.22	-5.45	-5.58	-6.30	-5.78	0.37

Table 6.3 Results after fitting parabolic curves to the data in Fig. 6.17.

k	c_k	d_k	γ_k
1	1.49	29.2	4.31
2	2.71	10.0	4.34
3	1.53	14.0	-6.03
4	2.65	9.8	-5.96

fitting approach as described above, with $l_a = 0\text{mm}$, $l_b = 4\text{mm}$, $l_c = 8\text{mm}$. The results are tabulated in Table 6.4, which agrees well with those in Table 6.1 and (6.10).

Table 6.4 Results after fitting parabolic curves to the data in Fig. 6.11.

k	c_k	d_k	γ_k
1	1.48	52.2	-0.32
2	2.75	10.3	-0.26

7

Conclusions and Prospects

7.1 Concluding Remarks

In this dissertation we have considered the imaging of a non-uniform medium by ultrasound. If the non-uniformity can be divided into two groups: one is like a totally random field, while the other is structurally non-uniform, then our interest has been in the latter. Although our research is still preliminary and has not been applied to actual tissue samples, we have confirmed the validity of our analyses by computer simulation, as well as by experimental measurement of some simple geometries.

The main results of our research can be summarized as the following:

1. Demonstrated that it is possible to calculate the sound velocity profile of a one-dimensional medium using only a relationship between the travel times corresponding to two different incident angles;
2. Developed algorithms for calculating the sound velocities and thicknesses of layered media with either horizontal or non-parallel plane interfaces;
3. Proposed a spectral fitting approach to recover an δ-impulse series from its filtered and noise-corrupted version. Evaluated the error of the positions of these δ-impulses caused by measurement noise.

Some more detailed descriptions about our results are available:

After reviewing some of the most important results on the inverse scattering problem, we confined ourselves to one-dimensional problems and later,

to layered media with either horizontal or non-parallel interfaces.

Our treatment of the one-dimensional problem is unprecedented so far as we know. On comparing two signals measured at different incident anglse, it is noticed that waves coming from the same depth resemble each other, even though they arrive at the surface at different time instants. This fact indicates that it is possible to make the two waveforms nealy the same (according to certain criteria) by stretching or contracting the time-axis of one of them. In this way a functional relationship is established between the two travel times. A simple derivation is then given which shows that the one-dimensional sound velocity profile can be recovered as a function of depth from this travel time relationship, under the assumption that the probing wave is a plane wave.

Next we turned our attenuation to layered media. Apparently a layered medium with horizontal plane interfaces is a special case of the general one-dimensional media. The new problem here is that the probing wave is not planar, but spherical. Using the ray approximation we investigated the dependency of increments of travel time on the propagation angle, and found the relationship $dt \sim \cos^{\alpha}\theta$ to be a very good approximation. Based upon this observation we modified the analysis which is derived under the plane wave assumption, and developed an algorithm for the processing of data obtained with spherical waves.

Layered media with non-parallel interfaces are treated quite differently. Although some relationships have been established between increments of travle time and propagation angles, the final solution is based upon a minimization formulation, *i.e.*, the medium parameters are varied so that the travel times calculated from the reconstructed model agree with those of observation. The adjustment of the sound velocity c_k of the kth layer is made through the secant method, whereas the thickness d_k and the inclination angle γ_k are obtained by solving a minimization problem, using the Marquardt-Levenberg algorithm, which is a combination of the Gauss-Newton method and the gradient method.

The problem of estimating pulse positions from signals which contain measurement noise has been considered. The reflection from a layered medium is modeled by the convolution of an incident pulse with the impulse response of the medium, which consists of a series of δ-impulses. The problem is to estimate the accurate positions of these δ-impulses from the received signal. We propose to solve this problem by a spectral fitting approach, in which we fit terms like $\rho_i e^{-i\omega\tau_i}$ to the estimated spectrum of the impulse response. This fitting problem can be solved efficiently using the FFT. Furthermore we analysed the fluctuation of the estimated pulse positions caused by additive noise, using the peak position of the cross-correlation function. This not only leads to the analytical result of (4.29), but also provides an alternative way for estimating the delay between two pulses. In fact this latter approach is less time consuming when the rough positions of the two pulses are known, and the purpose is to make an accurate estimation of the delay between them.

There are several points which should be mentioned:

The inverse scattering problem is known to be ill-conditioned [71,72], in the sense that small errors in the input data are amplified during the process of inversion, and emerge as larger errors of the results. As an example, we have considered probing a one-dimensional medium with plane waves of incident angles 0° and 15°, and arrived at the conclusion that, the relative error in estimating the interval between two pulses is amplified by about 30 times when it appears as the relative error of the calculated sound velocity. This amplification equals 8 times when the two angles are 0° and 30°. Simulation studies of more realistic settings (§5.6) show similar results. To avoid this ill-conditionedness, the only way is to employ signals whose incident angles have as large a difference as possible. However, as noted in §5.6, even if the recovered sound velocities and thicknesses are not accurate by themselves, the travel times calculated from them are usually accurate enough to be applied to improve the focusing.

When it comes to real biological tissues, there are several problems which need consideration:

1. Multiple reflections. We paid no special attention to multiple reflections in our processing, because results of simulation study show that multiple reflections may be negligible compared to the primary reflections, for the soft tissues found in human body.

2. The generation of transverse waves, which might happen if there is a bony interface, has not been considered here, because we are mainly interested in the bodywall in the abdomen.

3. Attenuation inside each layer. If the attenuation is independent of frequency, then it has no great influences to the estimation of pulse positions; on the other hand, if it is dependent on frequency, then we can estimate it from the spectrum of the two pulses reflected from the two interfaces which sandwiches that layer. So in any case, the attenuation in a layered medium seems to be an unimportant problem.

4. The interfaces not only may have arbitrary shapes, but also may be not specular at all. This presents a real difficulty. If it can be approximated by a one-dimensional model, then we may consider a one-dimensional problem with continuous profiles, as done in §3.1. But the more general case is out of our scope.

7.2 Some Prospects for the Imaging of Non-Uniform Media

The research reported here is a mere start of a long journey of imaging a non-uniform, refractive medium with accuracy. It is not even clear if the present approach—starting from a simple layered medium and adding complexities to the model step by step—is promising, or is it better to attack the problem in one step, for example, by assuming a two dimensional spatial distribution of sound velocity and density. Inspite of this question, let us consider several directions in which the present research may be continued:

1. The estimation of pulse positions:
   More elaborated studies are necessary to obtain a method-independent

lower bound to the error of position estimation in the presence of measurement noise. Such a lower bound will provide a solid fundation to the estimation of the error of reconstructed profiles.

2. We have only considered inclination of the interfaces within one plane. In a three-dimensional world the inclination represented by a normal vector has two independent components. Planes pitch not only from left to right, but also in the forward-backward direction. To inverse data from such media we may need to collect signals with transducers arranged in a cross (Fig. 7.1) instead of only along a line.

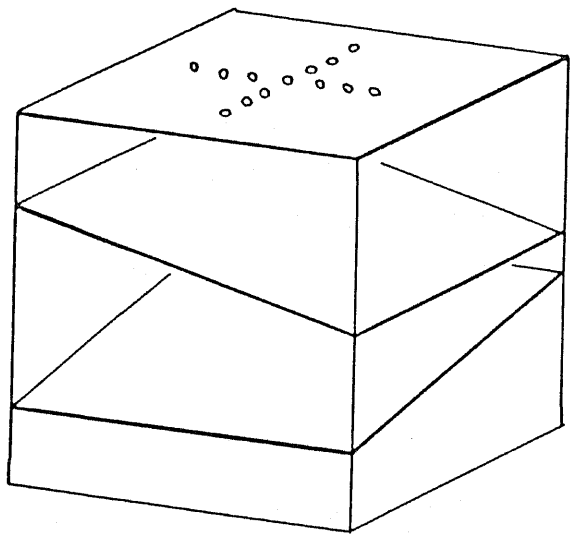

Fig. 7.1 Transducers arranged in a cross are needed to get data for the inversion of layered media, whose interfaces are planes of arbitrary inclination.

3. Interfaces of arbitrary shapes.
   This is a big step toward reality. However it is also much more difficult to measure and process the data of such media. First we need a way to specify the interfaces. One may use some base functions, but it is perhaps simpler to specify N points on one interface, and use spline or

other interpolation to obtain the whole surface. One must be careful in doing this because a small error in the inclination of the surface may cause the ray to be reflected to a totally different location. To inverse for such a medium we need $N+1$ signals (N for the surface and 1 for the sound velocity of that layer) measured at $N+1$ different locations. Minimization is perhaps the only method of solution.

4. New forms of data acquisition.

   The data used in this research are collected with a fixed transducer and a moving receiver. Taking the position of the transmitter as the abscissa and the position of the receiver as the ordinate (Fig. 7.2), this collection corresponds to a vertical line. Other forms of data collection are imaginable. For example, the transducer and the receiver may be moved at the same time in opposite directions so that their middle point is unmoved, or they may be moved in the same direction so that their distance is unchanged (a special case is that their distance is always zero). More investigations are necessary to judge which form is most suitable for our purpose.

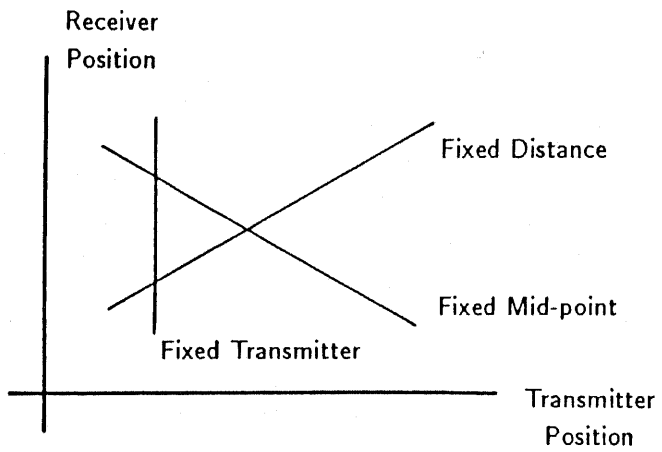

Fig. 7.2 Transmitter positions and receiver positions, and different data collcetion schemes.

We finish by commenting that, so long as we are imaging a non-uniform refractive medium, we should not close our eyes to this reality. Focusing in such a medium cannot be perfect unless we know the distribution of sound velocity. What we have been doing is like shouting aloud at mountains and listening to the echoes with many ears. The question is, can we hear the shape of the mountain, and the variation of sound speed (probably caused by temperature differences)? This is a difficult task, but is worth trying.

~ *The End* ~

Acknowledgements

I was vaguely aware of the influence of a non-uniform bodywall on the qualities of ultrasonic measurements and imaging when I finished my master course 3 years ago, but it was Professor Robert C. Waag of the University of Rochester, who introduced me to the researches on the inverse scattering problem. In performing the research work reported here, as well as during the past 5 years which I spent at the University of Tokyo, I have always received timely and instructive advices and comments from my supervisor, Professor Masao Saito. I am also thankful to Dr. Akira Watanabe and Dr. Kenji Ikeda who have been helpful since the very beginning of my research life at the Saito's Laboratory.

I have benefitted from discussions with many of my colleagues, including Dr. Tusyoshi Shiina who is now with the University of Agriculture and Technology of Tokyo, Mr. Shimura, Mr. Murakami, Mr. Shiba, Mr. Yamada and Mr. Iida of the Fujitsu Laboratory. Inside the Saito's Laboratory I have enjoyed friendship with many Japanese students. I want to mention especially the help I have obtained from Mr. Seiichi Suzuki, and the many stimulus discussions I have had with Mr. Toshiyuki Tanaka.

The experimental measurements reported here are all carried out with the help of the Fujitsu group, especially with the help of Mr. Noda, as we do not have a device in which the transducer positions are accurately known. Their cooperation is highly appreciated.

Still I will not forget the kindness and concern shown to me by Mr. Morii's family. For many times their friendship helped me to escape from homesickness and to concentrate on my study.

Finally I wish to thank my parents for letting their only son to study abroad for so many years, and showing their understanding and encouragement all the time to his deeds.

Appendix A

Non-Perpendicular Plane Waves in One-Dimensional Media

Consider the incidence of a plane wave on a interface between two media (Fig. A.1). The wave motion can be represented by the velocity potential ψ, whose gradient is the opposite of partical velocity, *i.e.*,

$$\vec{v} = -\nabla\psi \tag{A.1}$$

From wave equations (2.1) and (2.2) the connection between p and ψ can be obtained:

$$p = \rho\frac{\partial\psi}{\partial t} \tag{A.2}$$

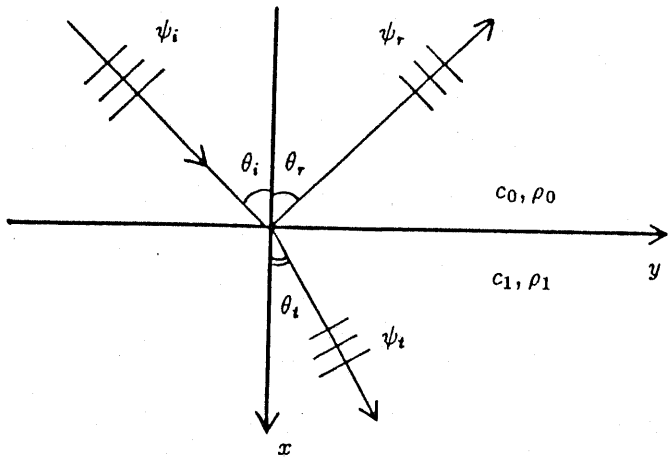

Fig. A.1 A plane wave incident on an interface between two media.

There are 3 components of wave motion in Fig. A.1: the incident field, the reflected field, and the transmitted field, represented ψ_i, ψ_r and ψ_t respectively. Their dependencies on x, y and t can be summarized in one variable because they are intrinsically one-dimensional:

$$\begin{cases} \psi_i(x,y,t) = \psi_i\left(t - \dfrac{1}{c_0}(x\cos\theta_i + y\sin\theta_i)\right) \\ \psi_r(x,y,t) = \psi_r\left(t - \dfrac{1}{c_0}(-x\cos\theta_r + y\sin\theta_r)\right) \\ \psi_t(x,y,t) = \psi_t\left(t - \dfrac{1}{c_1}(x\cos\theta_t + y\sin\theta_t)\right) \end{cases} \tag{A.3}$$

The boundary condition on the interface requires that the pressure and the normal partical velocity be continuous. The former leads to

$$\rho_0\psi_i' + \rho_0\psi_r' = \rho_1\psi_t'|_{x=0}$$

or

$$\rho_0\left(\psi_i'\left(t - \frac{\sin\theta_i}{c_0}y\right) + \psi_r'\left(t - \frac{\sin\theta_r}{c_0}y\right)\right) = \rho_1\psi_t'\left(t - \frac{\sin\theta_t}{c_0}y\right) \tag{A.4}$$

which cannot hold unless ψ_i, ψ_r and ψ_t have the same time dependence, and

$$\frac{\sin\theta_i}{c_0} = \frac{\sin\theta_r}{c_0} = \frac{\sin\theta_t}{c_1} \tag{A.5}$$

This equation gives the law of reflection and the law of refraction (the Snell's law). The requirement of continuous normal velocity across the interface reduces to

$$\frac{\cos\theta_i}{c_0}(\psi_i' - \psi_r') = \frac{\cos\theta_t}{c_1}\psi_t' \tag{A.6}$$

From (A.4) and (A.6) we can solve for ψ_r and ψ_t:

$$\begin{cases} \psi_r' = \dfrac{\rho_1 c_1\cos\theta_i - \rho_0 c_0\cos\theta_t}{\rho_1 c_1\cos\theta_i + \rho_0 c_0\cos\theta_t}\psi_i' \\ \psi_t' = \dfrac{2\rho_0 c_1\cos\theta_i}{\rho_1 c_1\cos\theta_i + \rho_0 c_0\cos\theta_t}\psi_i' \end{cases} \tag{A.7}$$

From this result we see that, if new sound velocities are defined by

$$c_0' = \frac{c_0}{\cos\theta_i}, \quad c_1' = \frac{c_1}{\cos\theta_t} \tag{A.8}$$

then the amplitudes of the reflected and the transmitted waves can be calculated as though the waves are perpendicular waves.

This same fact can also be derived from the wave equation. Since the partical velocity has only the x and y components v_x and v_y, (2.1) and (2.2) can be rewritten as

$$\begin{cases} \dfrac{\partial p}{\partial x} = -\rho \dfrac{\partial v_x}{\partial t} \\ \dfrac{\partial p}{\partial y} = -\rho \dfrac{\partial v_y}{\partial t} \\ \dfrac{\partial p}{\partial t} = -\dfrac{1}{\kappa}\left(\dfrac{\partial p}{\partial x} + \dfrac{\partial p}{\partial y}\right) \end{cases} \tag{A.9}$$

Consider harmonic wave motions such that $\partial/\partial t$ can be replaced by multiplication with $i\omega$. Furthermore, from (A.3) and (A.5) it is clear that any derivation with respect to y can be calculated in the following way:

$$\frac{\partial}{\partial y} = \frac{-\sin\theta}{c}\frac{\partial}{\partial t} = -\frac{i\omega \sin\theta}{c} \tag{A.10}$$

Thus (A.9) can be transformed into

$$\begin{cases} \dfrac{\partial p}{\partial x} = -i\omega\rho v_x \\ -i\omega \dfrac{\sin\theta}{c} p = -\omega\rho v_y \\ i\omega p = -\dfrac{1}{\kappa}\dfrac{\partial v_x}{\partial v_y} + \dfrac{1}{\kappa} i\omega \dfrac{\sin\theta}{c} v_y \end{cases}$$

Eliminating v_y from the second and the third equation, we get

$$\begin{cases} \dfrac{\partial p}{\partial x} = -i\omega\rho v_x \\ \dfrac{\partial v_x}{\partial x} = -i\omega\kappa \cos^2\theta p \end{cases} \tag{A.11}$$

If we define an equivalent compressibility $\kappa' = \kappa\cos^2\theta$, then equation (A.11) becomes exactly the same as the equation for perpendicular waves. In this way the non-perpendicular waves can be treated without any additional difficulty.

The calculation of equivalent compressibility is straightforward given $\rho(x)$, $\kappa(x)$ and θ_0.

First the sound velocity $c(x)$ is calculated: $c(x) = 1/\sqrt{\rho(x)\kappa(x)}$. Then the propagation angle $\theta(x)$ is obtained by using the Snell's law repeatedly:

$$\frac{\sin\theta(x)}{c(x)} = \frac{\sin\theta(x-\Delta x)}{c(x-\Delta x)} = \cdots = \frac{\sin\theta_0}{c_0} \equiv p_0 \qquad (A.12)$$

Thus $\theta(x) = \sin^{-1}(p_0 c(x))$, and finally

$$\kappa'(x) = \kappa(x)\cos^2\theta(x) = \kappa(x)[1 - p_0^2 c^2(x)] \qquad (A.13)$$

The equivalent sound velocity $c'(x)$ at x can be obtained from $\rho(x)$ and $\kappa'(x)$:

$$c'(x) = \frac{1}{\sqrt{\rho(x)\kappa'(x)}} = \frac{1}{\sqrt{\rho\kappa}\cos\theta(x)} = \frac{c(x)}{\sqrt{1 - p_0^2 c^2(x)}} \qquad (A.14)$$

Some intuitive explainations are in need to understand the meaning of this equivalent velocity. Referring to Fig. A.2, consider the incidence of a wavefront ψ_1 on a flat plate. It impinges on the plate at point A, and a reflection ψ_2 and a refraction ψ_3 are generated. ψ_3 propagates on, and after reflection at B and refraction at C, emerges as ψ_4. Now ψ_1 is reflected not only at A, but also at C (because it is infinitely large). The reflection at C will be denoted as ψ_5, which is on the same plane as ψ_2. The time interval T between ψ_4 and ψ_5 is calculated from the time difference $t_{\mathrm{ABC}} - t_{\mathrm{DC}}$. With the help of Fig. A.2, we can write down

$$T = \frac{2d}{c_1\cos\theta_1} - \frac{2d\tan\theta_1\sin\theta_0}{c_0} \qquad (A.15)$$

Using $\sin\theta_0/c_0 = \sin\theta_1/c_1$ the above expression can be reduced to

$$T = \frac{2d\cos\theta_1}{c_1} \qquad (A.16)$$

So we see that the time interval is proportional to $\cos\theta_1$, and the equivalent sound velocity is $2d/T = c_1/\cos\theta_1$.

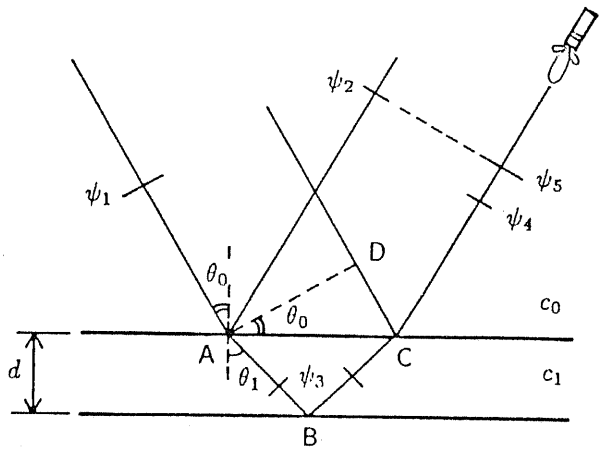

Fig. A.2 Non-perpendicular plane wave in a one-dimentional medium.

Appendix B

Reflection of a Spherical Wave by a Plane Interface

The materials in this appendix can be found in some text books [18,41]. We included them here not only for the convenience of the reader, but also because that these are the basis of travel time calculations for spherical waves.

Let us consider an incident spherical wave with center at $\vec{r}_0$:

$$p_i(\vec{r}|\vec{r}_0,t) = \frac{1}{R} f\left(t - \frac{R}{c_0}\right) \qquad (B.1)$$

where $R = |\vec{r} - \vec{r}_0|$. Denoting the Fourier transform of $f(t)$ by $F(i\omega)$, we have

$$p_i(\vec{r}|\vec{r}_0,t) = \frac{1}{2\pi R}\int_{-\infty}^{+\infty} F(i\omega) e^{-i\omega R/c_0} \cdot e^{i\omega t} d\omega \qquad (B.2)$$

If the reflection to a harmonic component

$$p_{i\omega}(\vec{r}|\vec{r}_0) = \frac{1}{R} e^{-i\omega R/c_0} \qquad (B.3)$$

is known, then the reflection to signals which have arbitrary time-dependencies can also be determined by virtue of linearity. Using the three-dimensional Fourier transform, $p_{i\omega}$ of (B.3) can be written as

$$p_{i\omega}(\vec{r}|\vec{r}_0) = \frac{1}{2\pi^2}\int_{-\infty}^{+\infty}\int_{-\infty}^{+\infty}\int_{-\infty}^{+\infty} \frac{e^{i\vec{K}\cdot(\vec{r}-\vec{r}_0)}}{K^2 - k^2} dK_x dK_y dK_z \qquad (B.4)$$

where $k = \omega/c_0$, $\vec{K} = (K_x, K_y, K_z)$, $K^2 = K_x^2 + K_y^2 + K_z^2$. This equation decomposes the spherical wave into a sum of plane waves, represented by $e^{i\vec{K}\cdot(\vec{r}-\vec{r}_0)}$.

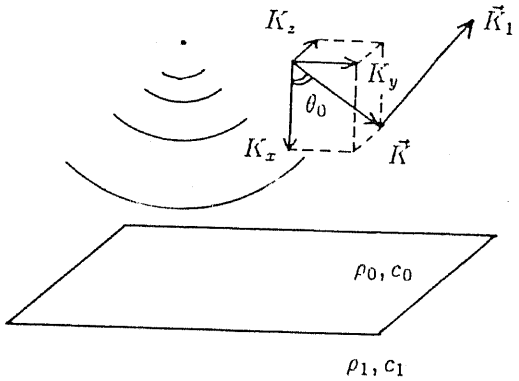

Fig. B.1 A spherical wave incident on a plane interface.

Referring to the coordinate system in Fig. B.1, the plane wave along the direction $\vec{K}$ incidents on the interface at an angle $\theta_0 = \cos^{-1}(K_x/K)$. From the results of Appendix A, we know that the reflection coefficient for this plane wave depends on θ_0, and the reflected plane wave can be represented by

$$r\left(\frac{K_x}{K}\right) e^{i[\vec{K}_1\cdot\vec{r}-\vec{K}\cdot\vec{r}_0]}$$

where

$$\vec{K}_1 = (-K_x, K_y, K_z)$$

$$r\left(\frac{K_x}{K}\right) = \frac{\rho_1 c_1/\cos\theta_1 - \rho_0 c_0/\cos\theta_0}{\rho_1 c_1/\cos\theta_1 + \rho_0 c_0/\cos\theta_0}$$

$$\theta_0 = \cos^{-1}(K_x/K), \quad \theta_1 = \sin^{-1}(c_1 \sin\theta_0/c_0)$$

The reflection to the spherical wave can be obtained by summing up all the reflections to the plane waves:

$$p_{r\omega}(\vec{r}|\vec{r}_0) = \frac{1}{2\pi^2}\int\int\int \frac{r(K_z/K)e^{i[\vec{K}_1\cdot\vec{r}-\vec{K}\cdot\vec{r}_0]}}{K^2-k^2} dK_x dK_y dK_z \qquad (B.5)$$

This integration cannot be carried out analytically, but a very good approximation, valid in the limit of high frequencies, is available. This approximation is based upon the stationary phase approximation [41,57], which is encountered in evaluating integrations of the following form:

$$I = \int_{-\infty}^{+\infty} \phi(x) e^{if(x)} dx \qquad (B.6)$$

If $\phi(x)$ is a slowly changing function with respect to one oscillation of $e^{if(x)}$, the various contributions to the integral will cancel out by anulling plus and minus values. However, if there is a value of x for which $f(x)$ is stationary, then in the neighborhood of this point, there will be a nonoscillating contribution to the integration (Fig. B.2). Denoting this point by α and using Taylor's series, we obtain

$$f(x) = f(\alpha) + \frac{f''(\alpha)}{2!}(x-\alpha)^2 + \cdots \qquad (B.7)$$

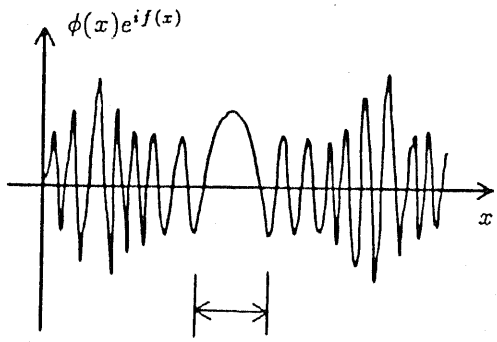

Fig. B.2 The main contribution to the integration comes from near the stationary phase point.

Since the integration has an appreciate value in the neighborhood of α only, and $\phi(x)$ is a slowly changing function, we may approximate it by

$$I \approx \int_{-\infty}^{+\infty} \phi(\alpha) e^{i\left[f(\alpha)+\frac{f''(\alpha)}{2!}(x-\alpha)^2\right]} dx \qquad (B.8)$$

which can be easily evaluated.

Turning back to the integration of (B.5), first we change variables to the cylindrical coordinate:

$$K_y = \mu\cos\beta, \quad K_z = \mu\sin\beta$$
$$y = w\cos\phi, \quad z = w\sin\phi.$$

We also assume that the center of the spherical wave to be on the x axis: $\vec{r}_0=(-d,0,0)$. With these changes (B.5) becomes

$$p_{r\omega}(\vec{r}|\vec{r}_0) = \frac{1}{2\pi^2}\int_0^{+\infty}\mu d\mu\int_0^{2\pi}d\beta\int_{-\infty}^{+\infty}dK_x\cdot r\left(\frac{K_x}{\sqrt{K_x^2+\mu^2}}\right)\frac{e^{i[-K_x(x-d)+\mu w\cos(\beta-\phi)]}}{K_x^2+\mu^2-k^2} \tag{B.9}$$

The integration with respect to K_x can be obtained using residuals

$$\int_{-\infty}^{+\infty}\frac{e^{-iK_x(x-d)}}{K_x^2-\sigma^2}\cdot r\left(\frac{K_x}{\sqrt{K_x^2+\mu^2}}\right)dK_x = -2\pi i e^{i\sigma(x-d)}\ r(-\sigma/k)\cdot\frac{1}{2\sigma} \tag{B.10}$$

where we have defined $\sigma=\sqrt{k^2-\mu^2}$, and used only the residual at $K_x=-\sigma$, because the reflected waves are propagating in the $-x$ direction.

Substituting this result in (B.9),

$$p_{r\omega}(\vec{r}|\vec{r}_0) = \frac{1}{2\pi i}\int_0^{+\infty}\mu d\mu\int_0^{2\pi}d\beta\ r(-\sigma/k)\frac{e^{i\sigma(x-d)+i\mu w\cos(\beta-\phi)}}{\sigma} \tag{B.11}$$

and using the relation $\int_0^{2\pi}e^{iu\cos v}=2\pi J_0(u)$, where J_0 is the 0th-order Bessel function, we get

$$p_{r\omega}(\vec{r}|\vec{r}_0) = \int_0^{+\infty}\frac{\mu}{i\sqrt{k^2-\mu^2}}\cdot r\left(-\frac{\sqrt{k^2-\mu^2}}{k}\right)J_0(\mu w)e^{i\sqrt{k^2-\mu^2}(x-d)}d\mu \tag{B.12}$$

If the frequency component which we are considering is high enough (k is large enough), then the phase of

$$J_0(\mu w)e^{i\sqrt{k^2-\mu^2}(x-d)} \tag{B.13}$$

is rapidly varying either around $\mu=0$ or $\mu=k$, while the rest of the integrand is slowly varying. So we may apply the stationary phase approximation. Using the asymptotic form of $J_0(u)$:

$$J_0(u)\big|_{u\to\infty}\to\sqrt{\frac{1}{2\pi u}}\left(e^{i(u-\pi/4)}+e^{-i(u-\pi/4)}\right)$$

the phases of (B.13) are approximately

$$\begin{cases} f_1(\mu) = \sqrt{k^2 - \mu^2}(x-d) + \left(\mu w - \frac{\pi}{4}\right) \\ f_2(\mu) = \sqrt{k^2 - \mu^2}(x-d) - \left(\mu w - \frac{\pi}{4}\right) \end{cases} \tag{B.14}$$

$f_1(\mu)$ has no stationary value for positive w and negative x (so the associated integration is almost zero), but $f_2(\mu)$ has. By putting $df_2/d\mu$ to zero we get the stationary point:

$$\mu_0 = \frac{w}{\sqrt{(x-d)^2 + w^2}} k \equiv \frac{w}{R_1} k \tag{B.15}$$

and the corresponding stationary phase approximation to (B.12) can be found to be

$$p_{rw}(\vec{r}|\vec{r}_0) \approx r\left(\frac{d-x}{R_1}\right)\frac{e^{-ikR_1}}{R_1} \tag{B.16}$$

Referring to the coordinate system in Fig. B.3, we see that the reflected wave is also approximately a spherical wave, whose center is the mirror image of the center of the incident wave, and the reflection coefficient is the same as that for a plane wave which propagates along the geometrical path.

The condition under which the approximation (B.8) is valid can be derived by considering an additional term of $\phi(x)$

$$\phi(x) \approx \phi(\alpha) + \phi'(\alpha)(x-\alpha)$$

in (B.7) and see how much the modification is. A result has been derived in this way [2]:

$$kR_1[(c_0/c_1)^2 - \sin^2\theta_0]^{3/2} \gg 1 \tag{B.17}$$

For applications in medical ultrasonic imaging, as a numerical example, the following values can be assumed:

$$f_0 = 1 \sim 6\text{MHz}, \quad c_0 = c_1 = 1.5\text{mm}/\mu\text{s}, \quad \theta_0 = 15^\circ$$
$$kR_1[(c_0/c_1)^2 - \sin^2\theta_0]^{3/2} = 3.77 \sim 22.65R_1$$

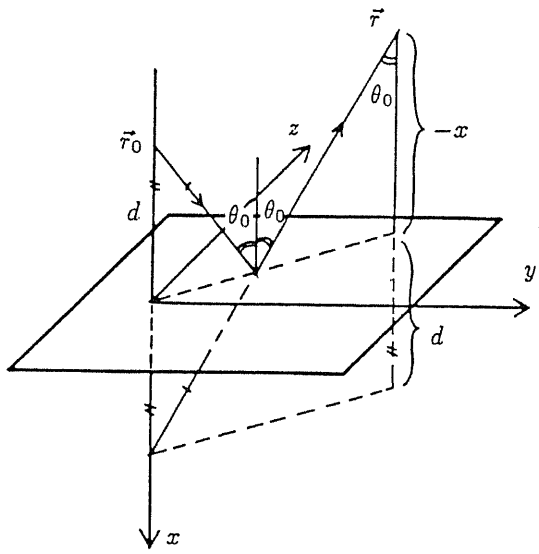

Fig. B.3 The stationary phase approximation leads to the conclusion that, the reflection to a spherical incident wave is also a spherical wave, the reflection coefficient being equal to that of a plane wave which follows the geometrical path from the source point to the observation point.

So, if the propagation path R_1 is more than a few mm, then the stationary phase approximation can be applied.

The reflection of an arbitrary pulse $f(t)$ can be obtained by summing up the reflection of individual harmonic component. Combining (B.2) and (B.16), the result is

$$\begin{aligned} p_r(\vec{r}|\vec{r}_0,t) &= \frac{1}{2\pi R_1} r\left(\frac{d-x}{R_1}\right) \int_{-\infty}^{+\infty} F(i\omega) e^{-i\omega R_1/c_0} \cdot e^{i\omega t} d\omega \\ &= \frac{1}{R_1} r\left(\frac{d-x}{R_1}\right) f(t - R_1/c_0) \end{aligned} \qquad (B.18)$$

References

[1] P. N. T. Wells, *Biomedical Ultrasonics*, Academic Press, 1977.

[2] R. C. Waag, "A Review of tissue characterization from Ultrasonic Scattering", *IEEE Trans. Biomed. Eng.*, vol. BME-31, 1984.

[3] R. C. Chivers, "Tissue characterization", *Ultrasound Med. Biol.*, vol. 7, 1981.

[4] J. F. Greenleaf and R. C. Bahn, "Clinical imaging with transmissive ultrasonic computerized tomography", *IEEE Trans. Biomed. Engi.*, vol. BME-28, no. 2, 1981.

[5] S. W. Flax, N. J. Pelc, G. H. Glover, F. D. Gutmann and M. McLachlan, "Spectral characterization and attenuation measurements in ultrasound", *Ultrasonic Imaging 5*, 1983.

[6] J. Ophir, T. H. Shawker, N. F. Maklad, J. G. Miller, S. W. Flax, P. A. Narayana and J. P. Jones, "Attenuation estimation in reflection: progress and prospects", *Ultrasonic Imaging 6*, 1984.

[7] D. Nicholas, "Evaluation of backscattering coefficients for excised human tissues: results, interpretation and associated measurements", *Ultrasound in Med. & Biol.*, vol. 8, no. 1, 1982.

[8] J. F. Greenleaf, S. A. Johnson, S. L. Lee, G. T. Herman and E. H. Wood, "Algebraic reconstruction of spatial distributions of acoustic absorption within tissue from their two-dimensional acoustic projections", In *Acoustical Holography* (ed. P. S. Green), Plenum Press, 1974.

[9] A. C. Kak, "Computerized tomography with x-ray, emission and ultrasonic sources", *Proc. IEEE*, vol. 67, no. 9, 1979.

[10] K. Sobeczyk, *Stochastic Wave Propagation*, Elsevier, 1985.

[11] P. C. Sabatier (editor), *Inverse Problems: An Interdisciplinary Study*, Academic Press, 1987.

[12] I. M. Gel'fand and B. M. Levitan, "On the determination of a differential equation from its spectral function", *Am. Math. Soc. Trans.*, Ser. 2, 1, 1955.

[13] R. G. Newton, "Inverse scattering. I. one dimension", *J. Math. Phys.*, 21(3), 1980.

[14] R. G. Newton, "Inverse scattering. II. three dimensions", *J. Math. Phys.*, 21, 1980.

[15] G. N. Balanis, "Inverse scattering: determination of inhomogeneities in sound speed", *J. Math. Phys.*, 23, 1982.

[16] G. N. Balanis, "The plasma inverse problem", *J. Math. Phys.*, vol. 13, no. 7, 1972.

[17] D. L. Jaggard and K. E. Olson, "Numerical reconstruction for dispersionless refractive profiles", *J. Opt. Soc. Am. A*, vol. 2, no. 11, 1985.

[18] P. M. Morse and K. U. Ingard, *Theoretical Acoustics*, McGraw-Hill, 1968.

[19] S. J. Norton, "Generation of separate density and compressity images in tissue", *Ultrasonic Imaging 5*, 1983.

[20] A. J. Devaney, "Variable density acoustic tomography", *J. Acoust. Soc. Am.*, 78(1), 1985.

[21] G. Beylkin and M. L. Oristaglio, "Distorted-wave Born and distorted-wave Rytov approximations", *Optics Communications*, vol. 53, 4, 1985.

[22] R. J. Wombell and M. A. Fiddy, "Acoustical imaging beyond Born and Rytov", *Acoustical Imaging*, vol. 16, ed. L. W. Kessler, Plenum Press, 1988.

[23] W. C. Chew and Y. M. Wang, "Reconstruction of two-dimensional permittivity distribution using the distorted Born interative method", *IEEE Trans. Med. Imaging*, vol. MI-9, no. 2, 1990.

[24] W. A. Schneider, "The common depth point stack", *Proc. IEEE*, vol. 72, no. 10, 1984.

[25] E. A. Robinson, "Migration of seismic data by the WKBJ method", *Proc. IEEE*, vol. 74, no. 3, 1986.

[26] A. E. Yagle, "Multidimensional inverse scattering: an orthogonalization formulation", *J. Math. Phys.*, 28(7), 1987.

[27] A. E. Yagle, "Connections between three-dimensional inverse scattering and linear least-squares estimation of random fields", *Acta Applicandae Mathematicae 13*, 1988.

[28] S. J. Norton and M. Linzer, "Ultrasonic reflectivity imaging in three dimensions: exact inverse scattering solutions for plane, cylindrical and spherical apertures", *IEEE Trans. Biomed. Eng.*, vol. BME-28, no. 2, 1981.

[29] D. K. Nassiri and C. R. Hill, "The use of angular acoustic scattering measurements to estimate structural parameters of human and animal tissues", *J. Acoust. Soc. Am. 79(6)*, 1986.

[30] J. A. Campbell and R. C. Waag, "Normalization of ultrasonic scattering measurements to obtain average differential scattering cross sections for tissues", *J. Acoust. Soc. Am. 74(2)*, 1983.

[31] J. C. Gore and S. Leeman, "Ultrasonic backscattering from human-tissue: a realistic model", *Phys. Med. Biol.*, vol. 22, no. 2, 1977.

[32] R. C. Chivers, "Review: the scattering of ultrasound by human tissues—some theoretical models", *Ultrasound in Med. & Biol.*, vol. 33, Pergamon Press, 1977.

[33] J. A. Campbell and R. C. Waag, "Measurement of calf liver ultrasonic differential and total scattering cross sections", *J. Acoust. Soc. Am. 75(2)*, 1984.

[34] D. K. Nassiri and C. R. Hill, "The differential and total bulk acoustic scattering cross sections of some human and animal tissues", *J. Acoust. Soc. Am. 79(6)*, 1986.

[35] Y. M. Wang and W. C. Chew, "An iterative solution of two-dimensional electromagnetic inverse scattering problem", *Int. J. Imaging Syst. Technolo.*, vol. 1, no. 1, 1989.

[36] L. A. Chernov, *Wave Propagation in a Random Medium*, McGraw-Hill, 1969.

[37] V. I. Tatarski, *Wave Propagation in a Turbulent Medium*, McGraw-Hill, 1961.

[38] R. K. Mueller, M. Kaveh and G. Wade, "Reconstructive Tomography and Applications to Ultrasonics", *Proc. IEEE*, vol. 67, no. 4, 1979.

[39] N. N. Bojarski, "The k-space formulation of the scattering problem in the time domain", *J. Acoust. Soc. Am. 72(2)*, 1982.

[40] N. N. Bojarski, "The k-space formulation of the scattering problem in the time domain: an improved single propagator formulation", *J. Acoust. Soc. Am. 77(3)*, 1985.

[41] C. B. Officer, *Introduction to the Theory of Sound Transmission*, McGraw-Hill, 1958.

[42] P. C. Pederson, O. Tretiak and P. He, "Impedance-matching properties of an inhomogeneous matching layer with continuously changing acoustic impedance", *J. Acoust. Soc. Am. 72(2)*, 1982.

[43] P. L. Goupillaud, "An approach to inverse filtering of near-surface layer effects from seismic records", *Geophysics*, vol. XXVI, no. 6, 1961.

[44] J. F. Claerbout, "Synthesis of a layered medium from its acoustic transmission response", *Geophysics*, vol. 33, no. 2, 1968.

[45] J. A. Ware and K. Aki, "Continuous and discrete inverse-scattering problems in a stratified elastic medium. I. plane waves at normal incidence", *J. Acoust. Soc. Am. 45(4)*, 1969.

[46] A. V. Oppenheim and R. W. Schafer, *Digital Signal Processing*, Prentice-Hall, Englewood Cliffs, 1975.

[47] J. F. Claerbout, *Fundamentals of Geophysical Data Processing*, McGraw-Hill, 1976.

[48] L. M. Brekhovskikh, *Waves in Layered Media, 2nd. ed.*, Academic Press, 1980.

[49] S. H. Gray, "A second order procedure for one-dimensional velocity inversion", *SIAM J. Appl. Math.*, vol. 39, no. 3, 1980.

[50] P. C. Pederson, O. J. Tretiak and P. He, "Numerical Techniques for the Inverse Acoustical Scattering Problem in Layered Media", *Acoustical Imaging 12 ed. by E. A. Ash and C. R. Hill*, Plenum Press, 1982.

[51] S. M. Candel, F. Defillipi and A. Launay, "Determination of the inhomogeneous structure of a medium from its plane wave reflection response, part I: a numerical analysis of the direct problem", *J. of Sound and Vibration*, 68(4), 1980.

[52] S. M. Candel, F. Defillipi and A. Launay, "Determination of the inhomogeneous structure of a medium from its plane wave reflection response, part II: a numerical approximation", *J. of Sound and Vibration*, 68(4), 1980.

[53] D. L. Jaggard and Y. Kim, "Accurate one-dimensional inverse scattering using a nonlinear renormalization technique", *J. Opt. Soc. Am. A*, vol. 2, no. 11, 1985.

[54] D. J. Thomson, "Inversion of ocean subbottom reflection data", *Progress in Underwater Acoustics*, ed. by H. M. Merklinger, Plenum Press, 1987.

[55] H. Sakoe and S. Chiba, "Dynamic programming algorithm optimization for spoken word recognition", *IEEE Trans. Acoust., Speech and Signal Process.*, vol. ASSP-26, 1978.

[56] K. Aki and P. Richards, *Quantitative Seismology: Theory and Methods*, vol. 2, W. H. Freeman Co., 1980.

[57] A. Ishimaru, *Wave Propagation and Scattering in Random Media*, vol. 2, Academic Press, 1978.

[58] R. P. Feynman, *QED, The Strange Story of Light and Matter*, Princeton University Press, 1985.

[59] M. Avriel, *Nonlinear Programming: Analysis and Methods*, Prentice-Hall, 1976.

[60] D. W. Marquardt, "An algorithm for least squares estimation of non-linear parameters", *Journal of the Society of Industrial and Applied Mathematics 11*, 1963.

[61] L. R. Lines and S. Treitel, "Tutorial: a review of least-squares inversion and its application to geophysical problems", *Geophysical Prospecting 32*, 1984.

[62] F. B. Smith, Jr., and D. F. Shanno, "An improved Marquardt procedure for nonlinear regressions", *Technometrics*, vol. 13, no. 1, 1971.

[63] L. R. Rabiner and G. Gold, *Theory and Application of Digital Signal Processing*, Prentice-Hall, 1975.

[64] H. L. V. Trees, *Detection, Estimation, and Modulation Theory*, Part I, John Wiley & Sons, 1968.

[65] C. W. Helstrom, *Statical Theory of Signal Detection*, Pergamon Press, 1960.

[66] G. C. Carter, "Coherence and time delay estimation", *Proc. IEEE*, vol. 75, no. 2, 1987.

[67] S. W. Flax and M. O'Donnel, "Phase-aberration correction using signals from point reflectors and diffuse scatterers: basic principles", *IEEE Trans. Ultrason. Ferroelec. Freq. Contr.*, vol. 35, no. 6, 1988.

[68] P. N. Keating, "More accurate interpolation using discrete Fourier transforms", *IEEE Trans. Acoust., Speech, and Signal Process.*, vol. ASSP-26, no. 4, 1978.

[69] Conte and de Boor, *Elementary Numerical Analysis*, 2nd Ed., McGraw-Hill, 1972.

[70] R. N. Bracewell, *The Fourier Transform and Its Applications*, 2nd ed., McGraw-Hill, 1978.

[71] A. G. Tijhuis, *Electromagnetic Inverse Profiling*, VNU Science Press, 1987.

[72] C. V. Schooneveld, "Inverse problems: a tutorial survey", in *Underwater Acoustic Data Processing*, ed. Y. T. Chen, Kluwer Academic Press, 1989.

Publications

Publications directly concerned with the present research:

[1] Dong-Lai Liu, "Sound Velocity Inversion in Layered Media with Band-Limited and Noise-Corrupted Data", Accepted by *IEEE Trans. on Biomed. Engi.*, December 1990.

[2] 劉　東来, 池田研二, 齋藤正男, "Ｂ－スキャンに於ける音速補正について", 第２９回日本ＭＥ学会大会, 1990.

[3] 劉　東来, "層状媒質における逆散乱問題について", 第５回日本ＭＥ学会秋季大会, 1990.

[4] Dong-Lai Liu, "Inverse Scattering in Layered Media with Band-Limited and Noise-Corrupted Data", *Proceedings of Far Eastern Conference on Medical and Biological Engeineering 1990 (FECMBE 1990).*

[5] 劉　東来, 齋藤正男, "層状媒質に於ける逆散乱問題", 日本超音波医学会第５７回研究発表会, 1990.

Publications on tissue characterization (attenuation estimation):

[1] Dong-Lai Liu and Masao Saito, "A New Method for Estimating the Acoustic Attenuation Coefficient of Tissue from Reflected Ultrasonic Signals", *IEEE Trans. Medical Imaging*, Vol. MI-8, No. 1, 107–110, March 1989.

[2] Dong-Lai Liu, Kenji Ikeda and Masao Saito, "On the Method-Independent Lower Bound (MILB) to the Variance of Attenuation Estimation in Random Reflection", *IEEE Trans. Medical Imaging*, Vol. MI-9, No. 1, March 1990.

[3] 劉　東来, 齋藤正男, "ＡＲデコンボルーション法による超音波減衰定数の推定", 第２７回日本ＭＥ学会大会, 1988.

[4] Dong-Lai Liu and Masao Saito, "A New Method for Estimating the Acoustic Attenuation Coefficient of Tissue from Reflected Ultrasonic Signals", *Proceedings of the Annual International Conference of the IEEE Engineering in Medicine and Biology Society*, 1988.

[5] 劉　東来, 齋藤正男, "ＡＲデコンボルーションとスペクトル平滑化による生体組織の超音波減衰定数の推定", 日本シミュレーション学会第７回シミュレーション・テクノロジー・コンファレンス, 1988.

[6] 劉　東来, 池田研二, 齋藤正男, "減衰定数推定におけるスペクトル・スロープの最尤推定", 第２８回日本ＭＥ学会大会, 1989.

[7] 劉　東来, 池田研二, 齋藤正男, "ＦＦＴスペクトル・スロープの最尤推定", 第４回日本ＭＥ学会秋期大会, 1989.